THESIS - TM185400

MODELING AND SIMULATION OF SERIES ACTIVE VARIABLE GEOMETRY SUSPENSION ON A QUARTER-CAR MODEL

SAMNANG CHHEANG
02111850087001

ADVISORS
Unggul Wasiwitono, ST., M.Eng.Sc., Dr.Eng.

Master Program
Mechanical Engineering Department
Faculty of Industrial Technology and System Engineering
Institut Teknologi Sepuluh Nopember
2020

THESIS - TM185400

MODELING AND SIMULATION OF SERIES ACTIVE VARIABLE GEOMETRY SUSPENSION ON A QUARTER-CAR MODEL

SAMNANG CHHEANG
02111850087001

ADVISORS
Unggul Wasiwitono, ST., M.Eng.Sc., Dr.Eng.

Master Program
Mechanical Engineering Department
Faculty of Industrial Technology and System Engineering
Institut Teknologi Sepuluh Nopember
2020

MODELING AND SIMULATION OF SERIES ACTIVE VARIABLE GEOMETRY SUSPENSION ON A QUARTER-CAR MODEL

TUGAS AKHIR
Diajukan Untuk Memenuhi Salah Satu Syarat
Memperoleh Gelar Magister Teknik
Program Studi S-2 Departemen Teknik Mesin

Fakultas Teknologi Industri dan Rekayasa Sistem
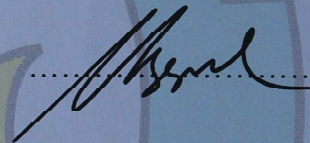Institut Teknologi Sepuluh Nopember

Oleh :
Samnang Chheang
NRP. 02111850087001

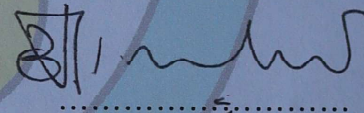Tanggal Ujian: 03 Agustus 2020
Periode Wisuda: September 2020

Disetujui oleh Pembimbing Tugas Akhir :

1. **Dr. Eng Unggul Wasiwitono,ST., M.Eng.Sc**
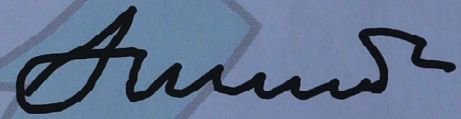   NIP. 197805102001121001
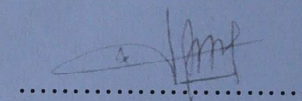
   Penguji:

1. **Bambang Pramujati, S.T. M.Sc., Ph.D**
   NIP. 196912031994031001

2. **Prof. Ir. I Nyoman Sutantra, M.Sc., Ph.D**
   NIP. 195106051978031002

3. **Dr. Latifah Nurahmi, S.T., M.Sc**
   NIP. 1986201712037

Kepala Departemen Teknik Mesin
Fakultas Teknologi Industri dan Rekayasa Sistem

Dr. Ir. Atok Setiyawan, M.Eng.Sc.
NIP. 196604021289031002

This page is blank

Modeling and Simulation of Series Active Variable Geometry Suspension on a Quarter-car Model

Student Name   : Samnang Chheang
Student ID   : 02111850087001
Advisors   : Unggul Wasiwitono, ST., M.Eng. Sc., Dr.Eng.

ABSTRACT

In this thesis report, an alternative suspension system of a vehicle called Series Active Variable Geometry Suspension (SAVGS) is studied. The SAVGS has been introduced another concept as well as proposed to enhance suspension performance. It has maintained some advantages of passive systems and contributed to avoid the impacts of other active solutions, of which it has lower compactness and higher power consumption. An extra single-link is retrofitted to the passive suspension. This link is jointed between the chassis and the upper-end of suspension instead of directly joining the chassis. It is actively controlled on the rotation respected to the longitudinal axle by a powered mechanism of the electromechanical actuator to regulate the force of suspension strut so that there is no added unsprung mass and little increase sprung mass. The full analysis of kinematic linkage of double wishbone arrangement and linkage of SAVGS can be served as a benchmark for designing the suspension system. Additionally, the performance of system dynamics has been compared between two varied linkage geometries for SAVGS and those of passive suspensions, as well as between two cases of single-link rotation ranges.

A linear equivalent model of the quarter car based on energy conservation principles is adopted to synthesize the Linear Quadratic Regulator (LQR) control scheme. The synthesized controller incorporated with actuator bandwidth limitation and controlling DC motor. The controller is implemented to a linear equivalent model of double wishbone quarter car, and after that implemented to the virtual prototype model of double-wishbone quarter car. The double-wishbone quarter-car model has been virtually experimental made in "*Simscape Multibody*" under road disturbance excited by the rotating eccentric cam.

In passive case, the root-mean-square (rms) of vertical sprung mass acceleration has been compared respect to non-linear models, the absolute errors are approximately 0.39% and 0.26% for linkage configuration 1 and configuration 2, respectively. The linkage geometry variation has affected on the aforementioned rms in which it becomes worse or better compared to the reference geometry depending on the road disturbance types. In highway road profile representation, the aforementioned rms in configuration 2 is smaller 5.24% than configuration 1's. Conversely, road smooth bump representation, that value in configuration 2 is greater 1.21% and 1.34% than configuration 1's for the linear and non-linear models, respectively. Furthermore, active case with SAVGS, the ride comfort improvement respected to corresponding passive case has illustrated that this

quality in linkage configuration 2 is somehow slightly better than configuration 1's. Physically, the center wheel-hub height in configuration 2 enabling to be adjusted higher than configuration 1's under the same commanded single-link positions which means the controller can handle higher road disturbance magnitude. However, the single-link rotation among two cases result less differences in ride comfort improvement for non-linear models. The aforementioned quality improvement under bump road is 6.30% and 7.01% for linkage configuration 1 and configuration 2. Interestingly, the road holding quality also has been improved along with the linear equivalent and non-linear models.

Keywords: Quarter car model, active variable geometry (AVG), linear quadratic regulator (LQR) control, suspension performances, double wishbone arrangement

Pemodelan dan Simulasi Penangguhan Geometri Variabel Aktif Seri Pada Model Seperempat Kendaraan

Nama   : Samnang Chheang
NRP   : 02111850087001
Dosen Pembimbing : Unggul Wasiwitono, ST., M.Eng. Sc., Dr.Eng.

ABSTRAK

Dalam laporan tesis ini, sistem suspensi alternatif kendaraan yang disebut Series Active Variable Geometry Suspension (SAVGS) dipelajari. SAVGS telah memperkenalkan konsep lain serta diusulkan untuk meningkatkan kinerja suspensi. Ini telah mempertahankan beberapa keunggulan sistem pasif dan berkontribusi untuk menghindari dampak dari solusi aktif lainnya, yang memiliki kekompakan yang lebih rendah dan konsumsi daya yang lebih tinggi. Tautan tunggal ekstra dipasang ke suspensi pasif. Tautan ini disambungkan antara sasis dan ujung atas suspensi alih-alih langsung bergabung dengan sasis. Ini secara aktif dikontrol pada rotasi yang berhubungan dengan sumbu longitudinal dengan mekanisme bertenaga dari aktuator elektromekanis untuk mengatur gaya penyangga suspensi sehingga tidak ada massa unsprung tambahan dan sedikit peningkatan massa sprung. Analisis lengkap keterkaitan kinematik dari susunan wishbone ganda dan keterkaitan SAVGS dapat digunakan sebagai tolok ukur untuk merancang sistem suspensi. Selain itu, kinerja dinamika sistem telah dibandingkan antara dua geometri tautan yang bervariasi untuk SAVGS dan geometri suspensi pasif, serta antara dua kasus rentang rotasi tautan tunggal.

Model linear ekuivalen mobil seperempat berdasarkan prinsip konservasi energi diadopsi untuk mensintesis skema kontrol Linear Quadratic Regulator (LQR). Pengontrol yang disintesis digabungkan dengan batasan bandwidth aktuator dan pengontrol motor DC. Kontroler diimplementasikan ke model linear ekuivalen mobil seperempat wishbone ganda, dan setelah itu diimplementasikan ke model prototipe virtual mobil kuartal tulang keinginan ganda. Model mobil seperempat wishbone ganda telah dibuat secara eksperimental di "Simscape Multibody" di bawah gangguan jalan yang ditimbulkan oleh cam eksentrik yang berputar.

Dalam kasus pasif, akar-rata-rata-kuadrat (rms) dari percepatan massa sprung vertikal telah dibandingkan dengan model non-linier, kesalahan absolut masing-masing sekitar 0,39% dan 0,26% untuk konfigurasi tautan 1 dan konfigurasi 2. Variasi geometri linkage mempengaruhi perusahaan-perusahaan tersebut menjadi lebih buruk atau lebih baik dibandingkan dengan geometri referensi tergantung pada jenis gangguan jalan. Pada representasi profil jalan raya, rms pada konfigurasi 2 lebih kecil 5,24% dari pada konfigurasi 1. Sebaliknya, representasi road smooth bump, nilai tersebut pada konfigurasi 2 lebih besar 1,21% dan 1,34% dibandingkan konfigurasi 1 untuk model linier dan non-linier. Selain itu, casing aktif dengan SAVGS, peningkatan kenyamanan berkendara yang terkait dengan casing pasif yang sesuai telah menggambarkan bahwa kualitas dalam konfigurasi

linkage 2 ini sedikit lebih baik daripada konfigurasi 1. Secara fisik, ketinggian hub roda tengah dalam konfigurasi 2 memungkinkan untuk disetel lebih tinggi dari konfigurasi 1 di bawah posisi tautan tunggal yang diperintahkan yang sama yang berarti pengontrol dapat menangani besaran gangguan jalan yang lebih tinggi. Namun, rotasi tautan tunggal di antara dua casing menghasilkan sedikit perbedaan dalam peningkatan kenyamanan berkendara untuk model non-linier. Peningkatan kualitas pada jalan bump adalah 6,30% dan 7,01% untuk konfigurasi linkage 1 dan konfigurasi 2. Menariknya, kualitas penahan jalan juga telah ditingkatkan seiring dengan model linear ekuivalen dan non-linear.

Kata Kunci: Model seperempat kendaraan, aktif geometri variable (AGV), linear quadratic regulator (LQR) control, kinerja suspensi, Pengaturan double wishbone

TABLE OF CONTENTS

viii

This page is blank

ACKNOWLEDGMENTS

This page is blank

PREFACE

This thesis report introduces readers to a part of the theories and practice of control systems dynamic. Due to passive suspension has limited its performances in terms of ride comfort and road holding, semi-active and active suspension are invented. However, active suspensions are facing with high power consumption, which imposes a new concept called SAVGS as an active low bandwidth control is introduced in order to challenge with power consumption and fail-safe operation.

SAVGS with two different arm linkage configurations is studied as well as analyzed their performances between passive suspension and active suspension in this work. The purpose of writing this work is to encourage readers and researchers to develop the SAVGS concept toward the implementation of real vehicles. Starting from a quarter-car model in this work as the first step of SAVGS development, it can be a benchmark study for students and researchers to develop a prototype.

The problems that came up during simulation are the performance obtained from "Simscape multibody." The ride comfort almost less improves when the controller weighted only on suspension deflection and tire deflection. However, the improvements reached are acceptable when the weighting controller only on tire deflection and vertical sprung mass acceleration.

The suggestion for reading this thesis is starting from the following steps; understand the concept of SAVGS, read how to build a linear equivalent model, figure out how to find the minimal state of single-link, read the relation between the linear actuator and rotary actuator, and read controller designed.

This page is blank

LIST OF FIGURES

LIST OF TABLES

This page is blank

CHAPTER 1

INTRODUCTION

1.1 Background

Vehicle suspension is the system of spring-damper that connects (by joints) a car body to its wheel and allows relative motion between the two [1] which is shown in Figure 1.1. The suspension system for cars plays an important role with various functions to provide good passenger comfort (root mean square of vertical body acceleration), vehicle road holding (dynamic of tire deflection) and to maintain overall vehicle stability. The designed suspensions are categorized into three main types [2] and shown in Figure 1.1.

1) Passive Suspension: The main component is a conventional spring-damper unit, it passively adapts to road profile and dissipates energy is caused by road disturbance.

2) Semi-Active Suspension: The structure is similar to passive suspension but the damping coefficient is actively variated by magnetorheological dampers, or electro-rheological, or solenoid valve-controlled dampers.

3) Active Suspension: An actuator functioned in parallel (hight bandwidth) or series (low bandwidth) with a passive spring or spring-damper unit to apply an independent force and provide a performance improvement.
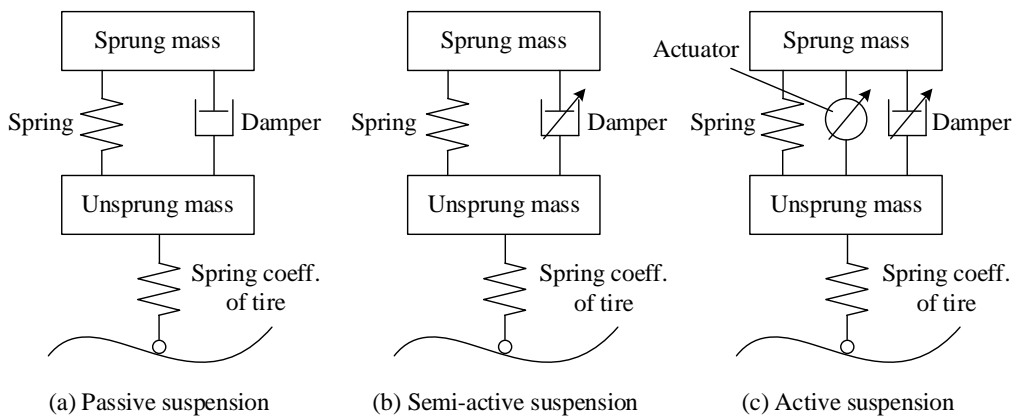
Figure 1.1 Three different suspension types [3]

Currently, suspension systems are presented with passive suspension for general vehicles. Passive suspension, which composes spring and damping coefficients at fixed rates, can only offer a compromise between passenger comfort and vehicle road holding [4] while the its allowable stroke still is bounded [5]. Consequently, it still exists the conflict condition which is the limitation of its performances. Passive suspensions in sport cars usually are stiff, harsh with poor passenger comfort while in luxury sedans offer softer suspensions but poor road handling capabilities. Poor road handling capability and decreased passenger comfort are due to excess car body vibrations resulting in artificial vehicle speed limitations, reduced vehicle-frame life and biological effects on passengers. However, passive suspensions still have been prioritized in the automobile market because of their simplicity, reduced cost, reliability, safe in operation, and less power consumption [6].

The active suspension, on the other hand, is extensively evaluated that it provides the best performance as compared to the aforementioned suspension types [7], its performances are enabling to be more developed and be recognized the overall potential by advance sensor integrations and intelligent controls. In recent decade, active suspensions encouraged to equip in the luxury vehicle are endlessly studied on their performance improvement; the essential approach is started from the quarter-car model [1], [2], [5], [7]–[13]; typically utilizing linear and non-linear models. However, in the real application the suspension lower end-strut is seldom connected to center mass of unsprung mass which leads the suspension system to be non-linear. There are different strategies of performance studied somewhat are suspension linkage and controller types. Several work study on the influences of linkage geometry of suspension, in [14] has been reported that the variation of double wishbone lower arm has significantly influences on the suspension performance. In addition, a few controllers have been proposed with the promising result; LQR [8]–[10], [12], [15]–[17]; LQG [5], [11]; and robust control H-infinity [1], [2], [7], [13], [14]. Although active suspension has advanced capabilities, the high bandwidth one considerably influences upon automotive market due to its several drawbacks, such as power consumption, lower compactness, and complexity.

To ease these conflicted solutions, the massive studies and implementing of active low bandwidth suspension and semi-active suspensions have proposed in the literatures [2], [5], [12], [5], [18] and commercially implemented in luxury vehicles; it has been reported that the performances are compatible with the high bandwidth active suspensions in term of ride comfort and road holding without violating the given constraints; as well as was available in lower cost. However, the endless studying on suspension performance improvement is imposed the researchers inventing a new concept of active low bandwidth suspension called Series Active Variable Geometry Suspension (SAVGS), which challenges with low power consumption and fail-safe operation.

The following chapters of this research are organized as follows. CHAPTER 2 presents the literatures of previous works and the basic theories used as references for the research. CHAPTER 3 presents state of the art to reach the controller design. CHAPTER 4 reports performance results under exciting road disturbance. CHAPTER 5 is the conclusion of the work.

1.2 Research Problem

Vehicle suspensions are sought to improve their performances, especially for ride comfort and road holding. Although active suspension has advanced capabilities, it still fails in vehicle production due to its aforementioned drawbacks. As a result, the SAVS concept is introduced. However, few researches have investigated the effect of suspension geometry arrangement on the dynamics behavior of suspension system. In addition, there are also few researches on how to design the control algorithm for low bandwidth SAVGS.

1.3 Research Objectives

The propose of this research is to study the characteristic response of the sprung mass of the quarter car (mini scale) which retrofit with series active variable geometry suspension (SAVGS). The SAVGS, which is classified as an active low bandwidth suspension, was designed the controller to actively controls the velocity and position of a single-link in a term rotation direction.

1.4 Scope of Research

The scope of this research focuses on:

➢ Design the prototype for a double wishbone quarter-car retrofitted with SAVGS.

➢ Design the controller for SAVGS

1.5 Contribution

The contributions of this research are:

➢ Full kinematic linkage of double wishbone as we as SAVGS bloc have been analyzed.

➢ Implement theoretical control of SAVGS used Linear Quadratic Regulator controller (LQR) scheme into "**Simscape Multibody**", which is a toolbox of Matlab, in order to make a virtual experimentation.

➢ The quarter-car model is simulated at two different configurations as well as at two cases of single-link rotation range for each configuration.

CHAPTER 2
LITERATURE REVIEW

2.1 Historical

In recent decades, an alternative suspension system of vehicles, which is called Series Active Variable Geometry Suspension (SAVGS), has been introduced another concept and is proposed to enhance its performance. The SAVGS not only has maintained some advantages of passive systems but also has contributed to the avoid impacts of other active solutions [6]. An extra single link is retrofitted to the passive suspensions or semi-active suspensions [19] as shown in Figure 2.1. This link, is jointed between the chassis and the upper-end of spring damper unit instead of joining upper end suspension directly to the chassis, and is actively rotated respect to chassis reference axle by powered mechanism of electromechanical actuator to regulate the force of suspension strut [1], thus there is no added unsprung mass and little increase sprung mass. Currently, there is some research on the SAVGS and its improvement. Most of those researches are focused on double wishbone arrangement [1], [2], [6], [7], [13], [18]–[20]. The SAVGS concept practically focuses on several purposes, such as vehicle ride comfort and road holding [7], [13], limit and reduce pitch rotation of the car chassis [6], controlled of chassis roll and pitch motions [19], [20].
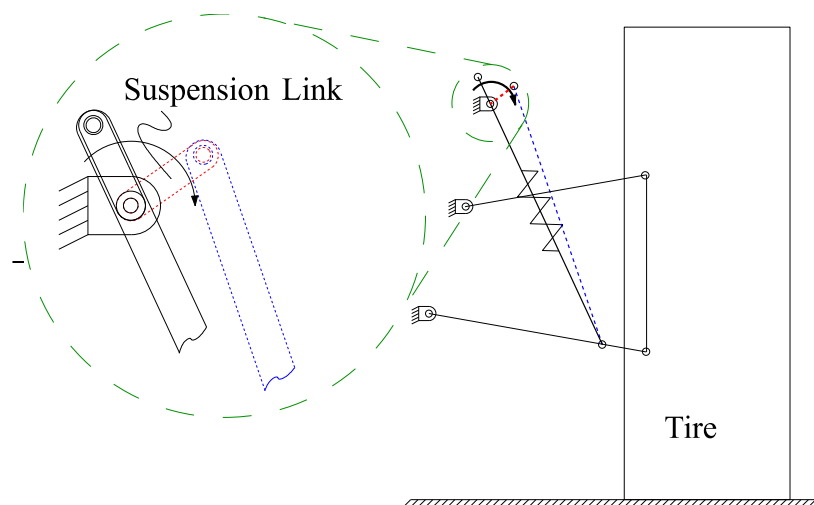
Figure 2.1 Sketch of SAVGS which actively rotate the single link [6].

The non-linear full car model has been developed for a generic high-performance sports car [6], [18]–[20], a fully laden SUV [19] and general road vehicles [18]. The study maneuvers are investigated during acceleration and braking event [6], cornering and combined cornering and braking events [20]. The design process, as well as the actuator modeling and selection, is presented and based on off-the-shelf components for a specific application [18]. The appropriate control approach which consists of actuator dynamics and respects all actuator constraints is presented in pitch attitude motion control system and correction algorithms to confirm that the physical and design constraints are satisfied [6], [18], [20]. A cascaded control scheme is presented to control the four independent actuators (one per wheel [20]. The intuition of the SAVGS performance, its requirements, operation, and influence on the vehicle direction response were demonstrated by simulation with a wide range set that respected standard open-loop maneuvers. The other is a co-design methodology [19] which consists of the component dimensioning framework and a multi-objective control scheme has been introduced to optimize the control abilities of SAVGS, while it is feasible in a vehicle and actuator design constraints. The dimensioning framework contains; the virtual work-based for a steady-state mathematical model; an algorithm for dimensioning the main SAVGS components respected to any given vehicle properties and steady-state performance objectives; and a detailed parameter sensitivity analysis on the dependencies that has existed between the chassis, the properties of the passive suspension, and the SAVGS. A general multi-objective control scheme that was able to serve for general application and a particular aspect of a combined chassis attitude control and overturning couple distribution control is detailed developed. The fast dynamics of the electromechanical actuators is desired to be uncoupled, thus the feasible low-pass of filtered measurements had been recorded. Then the terms for attitude and overturning couple distribution (OCD) control were presented [19]. A promising perform SAVGS concept is accepted, such as fail-safe operation, low power, and energy consumption, and using well known available technologies [6]. The results have confirmed that the proposed system is a worthy improvement of the chassis attitude control [18], [20]. The SAVGS with available geometric actuator and corresponding control system

is able to maintain well behaviour and roll motion at zero for the interval of normal acceleration and 0.9 of gravity [20]. Moreover, a developed SAVGS in the researches also able to successfully implemented with a combined pitch and roll events, such as the brake in turn maneuver. In steady-state situations, one actuator is approximately 6 kg and other off-the-shelf components have been selected, these selected actuators are able to maintain the chassis-level except in over demanding situations [18].
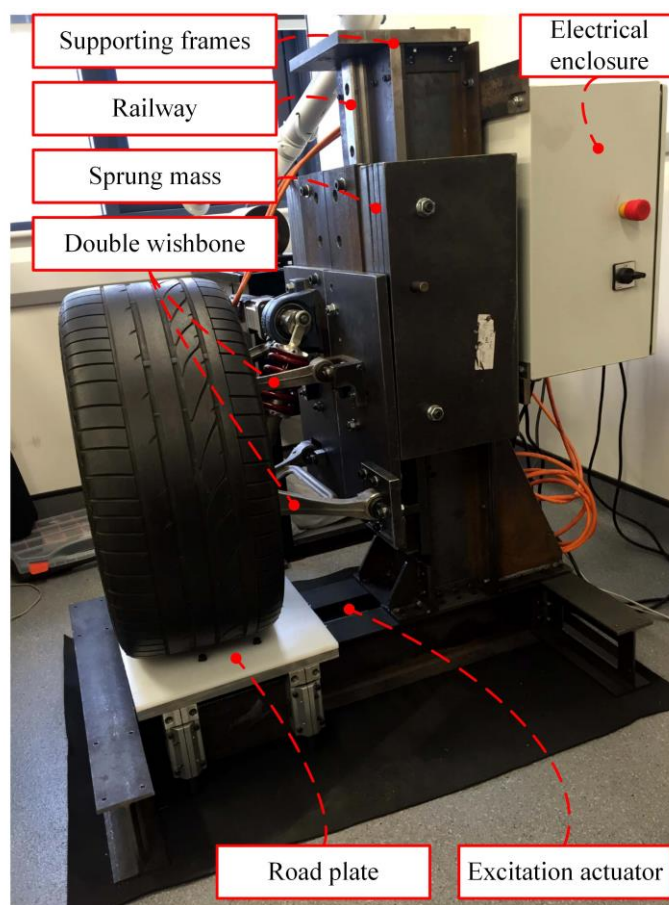
Figure 2.2 A design of mechanical quarter-car test rig with implementation of the SAVGS [2]

The 500w is the maximum allowable power consumption per actuator, the peak squatting/diving angles during transients are decreased by at least 30%. The more accurate prediction can be achieved by softening the spring of suspension [6], thus Active Variable Geometry Suspension (AVGS) could effectively adjust the single-

link toward the desired performance, which is an aspect of pitch motion and chassis attitude control [6], [19] and is required only low bandwidth actuation.

Apart from this , a nonlinear quarter car model of a high-performance car (represented one corner of car) with SAVGS, which represents accurately the vertical dynamics and car's geometry, has been presented [7]. The nonlinear quarter car model has been subsequently made the model identification based on the rig's experimental frequency response and a theoretical quarter car model [1] and made the robust control assessment [1], [2], [7], [13]. To ensure the test rig functionalities, the initial experimental test rig has been validated through both the passive and the active cases [1]. Then the SAVGS, which retrofitted into a GT (Grand Tourer), has been thereafter studied with experimentation and done a realistic quarter-car test rig on SAVGS's development of mechatronic system, as well as has been implemented with a road excitation mechanism [2] as shown in Figure 2.2.
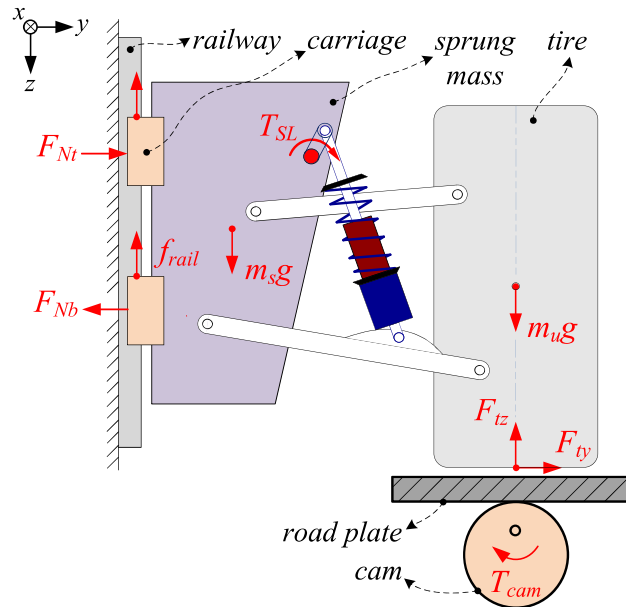
Figure 2.3 Schematic of the nonlinear model of the SAVGS quarter-car test rig [2]

A mechanical quarter-car test rig in Figure 2.2 was made its schematic shown in Figure 2.3. The schematic of quarter-car test-rig composes quarter-car components,

8

cam and road plate exciting as road disturbance, and railway guiding sprung mass component in purely vertical direction.

In addition of aforementioned concept, a linear equivalent model of one corner car of a Grand Tourer (GT), which based on the energy conservation principles, is successfully implemented [13], and has adopted to synthesize an H-infinity control scheme [1], [2], [7], [13]. The H-infinity control had been designed to track the external effects, then to stabilize the single-link position at lower frequencies, or to regulate the single-link velocity at higher frequencies [2], [7]. Then the controller which is simplified for this quarter-car linear model tuned the parameters through the singular value decomposition of the system's transfer matrix instead of iteration based on control bandwidth and simulation results [13]. A synthesis H-infinity controller has further taken into account, the signals measuring with expected availability of sensors, actuator dynamics and its (inner) position control loops [13], and the external disturbance of standard wide range beyond as normal road [7], [13] to enhance the ability of tracking suspension defection at low frequencies, which deflected as a result of the present of load transfer during longitudinal and/or lateral vehicle accelerations. The theoretical nonlinear quarter-car simulations, which include a further practical feature to compensate the difference between the theoretical and testing behaviours, subsequently illustrated that SAVGS is the potential improvements of suspension performance in terms of ride comfort and road holding [2]. The quarter-car experiments have been conducted concerning a sinusoidal road, a smoothed bump and hole, and a random road representative [2] to evaluate the SAVGS realistic capabilities and suspension performance improvement, the accuracy of the model, and the control schemes robustness. The experimentations within the initial feasibility of the SAVGS illustrated that; the vehicle dynamics, as well as the sprung mass vertical acceleration and the suspension deflection, are greatly reduced at around 2 Hz; the H-infinity controller is robust enough, although there are impacts of sensor noise, friction, and other factors [1]. The results compared to conventional passive suspension showed that the ride comfort improvement is up to 41%, whereas the SAVGS actuator which is at levels below 500 W is consumes very low power [2]. Moreover, the designed controllers have been further tried in the full-car nonlinear

model. The obtained results are significantly consistent and will assist as a basic clue for the develop of full-car specific controllers [13].

Besides the aforementioned concept, historically, the performance of low bandwidth active suspension control with continuously variable damper has been studied and simulated for the active quarter car models [12]. The LQR controller is designed and iteratively selected the damping ratio as well as the penalized factors in order to optimize the dynamic response of the system. The simulations are conducted under a road disturbance model which is evaluated by a real highway profile measurement. The results comparing to passive and high bandwidth active suspension systems, shows that ride comfort can be significantly increased while it is satisfying to the given constraints for road holding and suspension travel.

Recently, the quarter-car has been studied for passive and active suspension with the case of variable linkage geometry of the lower arm [14]. The dynamics response of sprung mass has been investigated under harmonic and bump excitation for each suspension behaviour. The result shows that the variation of lower arm geometry has greatly influenced on the sprung mass acceleration in passive case. However, it seems a less significant change in active-suspension case when the actuator is in non-saturations controlled.

2.2 Basic Theory

The main basis theories considered in this section are introduced two main points, which are a linear equivalent model of a quarter car retrofitted with SAVGS and a synthesized LQR control scheme designed to minimize the dynamic response of the multibody system under road excitation.

2.2.1 Linear Equivalent Model

The linear equivalent modelling method for the SAVS quarter car is used in [1]. This method, which compensates the nonlinear geometry of the SAVSG, allows the single-link has a large range of rotation angle. The linear equivalent model shown in Figure 2.4, is transformed from the non-linear multibody system in Figure 2.1
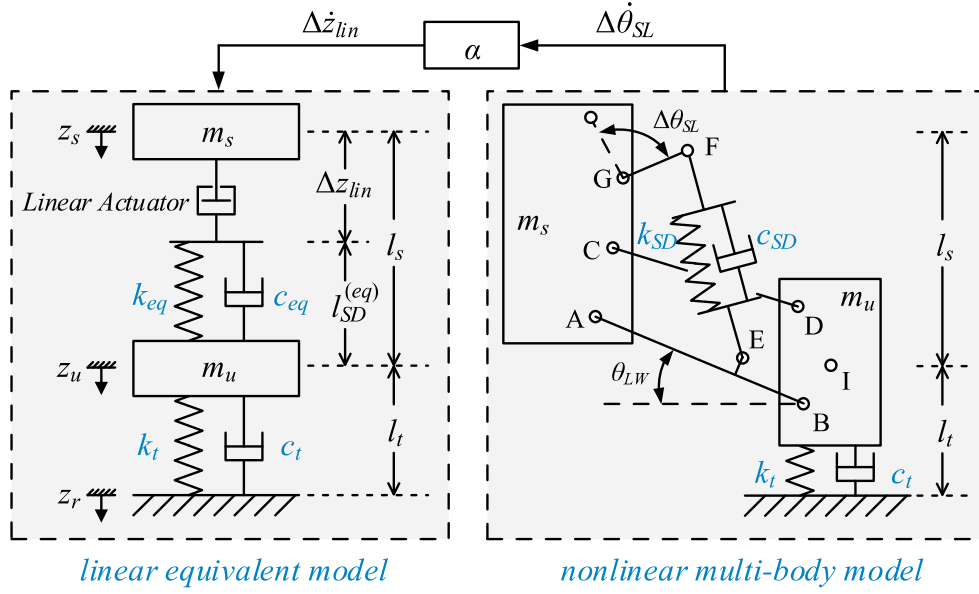
Figure 2.4 Linear equivalent model and non-linear multi-body model [1].

The velocity of the linear equivalent actuator and of the single-link actuator are reversibly converted through block α function [1], which compensates the nonlinear geometry of single-link. The function α is defined as below:

$$\alpha = \frac{\Delta \dot{z}_{lin}}{\Delta \dot{\theta}_{sl}},$$

(2.1)

where Δz_{lin} is the displacement of linear equivalent actuator and $\Delta \theta_{sl}$ is the rotation angle of the single-link which respects the reference point as in Figure 2.4 (right).

The linear equivalent is defined based on the non-linear multibody model, which exists some assumptions [2]:

1) Both models have the same suspension deflection and the same tire deflection

   ➤ $l_s = z_u - z_s$, assigned as the vertical distance between the sprung mass center and the unsprung mass center

   ➤ $l_t = z_r - z_u$, assigned as the vertical distance between the road surface and the unsprung mass center

$$l_s = \Delta z_{lin} + l^{(eq)}_{SD},$$
(2.2)

where $l^{(eq)}_{SD}$ is the length of the equivalent spring damper.

2) The single-link actuator and the equivalent linear actuator have the same power output:

$$T_{SL}\dot{\theta}_{SL} = F^{(eq)}_{SD} \Delta\dot{z}_{lin},$$
(2.3)

where $F^{(eq)}_{SD}$ denotes the equivalent spring force and T_{SL} is the torque produced by single-link.

3) The equivalent spring satisfies Hooke's law, while the equivalent damper has the same energy dissipation as the real one [13]

$$k_{eq} = k_{SD}R_{SD}^2 - F_{SD}\frac{dR_{SD}}{dz_I}$$

$$c_{eq} = c_{SD}R_{SD}^2,$$
(2.4)

where k_{eq} is the equivalent spring stiffness, c_{eq} is the equivalent damping, and R_{SD} is the installation ratio of suspension in Figure 2.4 (right) and can be defined as:

$$R_{SD} = \frac{dl_{SD}}{dz_I}$$
(2.5)

The equation motion of linear equivalent model of the SAVGS is described as [1]:

$$m_s\ddot{z}_s = k_{eq}(\Delta l_s - \Delta z_{lin}) + c_{eq}(\Delta\dot{l}_s - \Delta\dot{z}_{lin})$$

$$m_u\ddot{z}_u = -k_{eq}(\Delta l_s - \Delta z_{lin}) - c_{eq}(\Delta\dot{l}_s - \Delta\dot{z}_{lin}) + k_t\Delta l_t + c_t\Delta\dot{l}_t$$
(2.6)

2.2.2 Suspension Controller Design

The quarter car model of the low bandwidth active suspension (LBAS) has been studied and implemented with Linear Quadratic Regulator (LQR) in [12]. The linear model of LBAS is described in Figure 2.5.
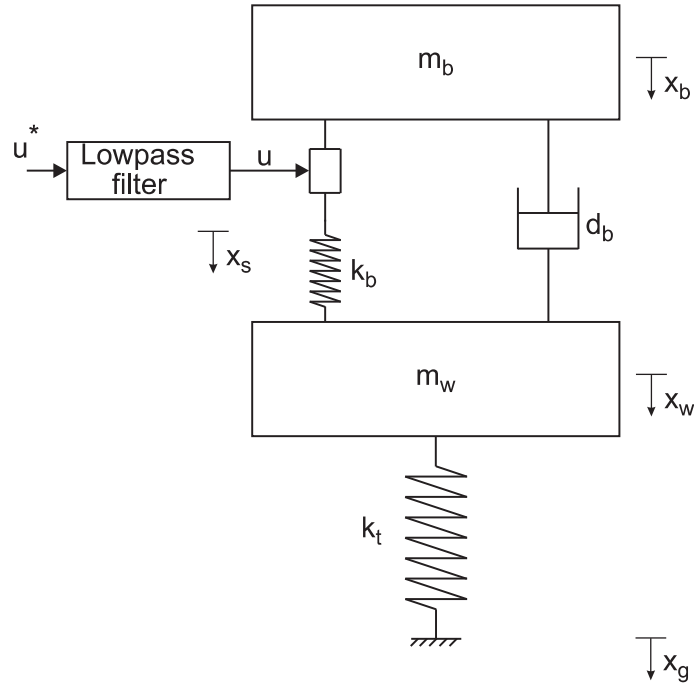
Figure 2.5 Low bandwidth active suspension (LBAS) model [12]

The design controller parameters in this sub-section are respected to the system in Figure 2.5. The design controller has proposed for the fourth-order system using linear quadratic regulator (LQR) design techniques [12]. Therefore, all states assumed that can be measurable. The used measurement signal responses under road disturbance are the vertical acceleration of sprung mass $\ddot{x}_b$, the suspension deflection $x_b - x_w$ and the measurement of the tire deflection $x_w - x_g$

The quadratic performance index is defined as

$$J = \lim_{t \to \infty} E\left[r_1 y_1^{\,2} + r_2 y_2^{\,2} + r_3 y_3^{\,2} \right], \tag{2.7}$$

where $E[.]$ denotes the expectation value. It consists the three important performance indices: Sprung mass acceleration y_1, suspension deflection y_2, and tire deflection y_3. The penalized factors r_2 and r_3 are varied in order to achieve the performance trade-off between ride comfort, suspension travel, and road holding; whereas r_1 is fixed at value of 1.

The resulting state feedback control law is [12]

$$u^* = -\mathbf{k}^T \mathbf{x}, \tag{2.8}$$

For the determination of the feedback gain k^T, the performance index in (2.7) is first rewritten as [12]

$$
\begin{aligned}
J &= \lim_{t \to \infty} E\left[\mathbf{y}^T \underbrace{\mathrm{diag}(1, r_2, r_3)}_{\tilde{\mathbf{R}}} \mathbf{y} \right] \\
&= \lim_{t \to \infty} E\left[\mathbf{x}^T \underbrace{\mathbf{C}^T \tilde{\mathbf{R}} \mathbf{C}}_{\mathbf{R_1}} \mathbf{x} + u \underbrace{\mathbf{d}^T \tilde{\mathbf{R}} \mathbf{d}}_{\mathbf{R_2}} u + \mathbf{x}^T \underbrace{\mathbf{C}^T \tilde{\mathbf{R}} \mathbf{d}}_{\mathbf{R_3}} u + u \underbrace{\mathbf{d}^T \tilde{\mathbf{R}} \mathbf{C}}_{\mathbf{R_3}^T} \mathbf{x} \right],
\end{aligned}
\tag{2.9}
$$

From (2.9), the controller gain vector is derived as

$$\mathbf{k}^T = R_2^{-1}(\mathbf{b}^T \mathbf{P} + \mathbf{R_3}^T) \tag{2.10}$$

where $\mathbf{P}$ is the symmetric, positive definite solution of the extended algebraic Riccati equation

$$\mathbf{0} = \mathbf{A}^T \mathbf{P} + \mathbf{P} \mathbf{A} - (\mathbf{P} \mathbf{b} + \mathbf{R_3}) R_2^{-1} (\mathbf{P} \mathbf{b} + \mathbf{R_3})^T + \mathbf{R_1} \tag{2.11}$$

14

2.2.3 Spring Stiffness Constant (k_{SD}) and Damping Coefficient (c_{SD}) of Suspension

The suspension used in simulation is "Gmade 1/10 Truck Shocks Suspension Piggy Back XD Aluminum 93MM'' as shown in Figure 2.6. The experiment was conducted to find spring stiffness constant and damping coefficient of suspension.

$$k_{SD} = \frac{F}{d} \tag{2.12}$$

Figure 2.6 Gmade 1/10 Truck Shocks Suspension Piggy Back XD Aluminum 93MM

where *F(N)* is axial force applies to the spring unit and *d(m)* is spring deflected length

$$c_{SD} = \frac{F}{v_{ins}}$$

(2.13)

where v_{ins} is instant deflected velocity of damper under external axial force. To simplify of the experiment, there are some assumptions:

➢ Spring stiffness will have constant values when applying the different load level

➢ The instant velocity (v_{ins}) is the same as the average velocity of damper travel (v_{av}) which is defined as below:

$$v_{av} = \frac{d}{t}$$

(2.14)

where $t(s)$ travel time.

The experimental procedure is followed as, the data for calculating the damping coefficient is collected at three different load levels. Each level takes the average of eight data. The damping coefficient is taken the average values of each load level. For spring stiffness is taken the data at three different load levels, then takes its average. The experimental results are shown in Table 2.1 and

Table 2.2.

Table 2.1 Experimental data for deriving the spring stiffness of suspension

Load Mass (g)	Original Spring's Length (mm)	Final Spring's Length (mm)	Deflected Length (mm)	Stiffness (N/m)
445		53.5	5.8	823.15
885	59.3	45.5	13.8	766.06
1015		42	17.3	759.61
The Average Stiffness (N/m)				782.94

Table 2.2 Experimental data for deriving the damping coefficient of suspension

Load Mass (g)	Travel Distance (mm)	Travel Time (s)	Average Damping Constant
95	22.4	0.98	50.290

		1.18	
		1.37	
		1.11	
		1.2	
		1.4	
		1.25	
		1.18	
165	22.4	0.53	41.099
		0.53	
		0.53	
		0.6	
		0.65	
		0.53	
		0.59	
		0.59	
220	22.4	0.39	35.408
		0.33	
		0.39	
		0.39	
		0.39	
		0.39	
		0.33	
		0.33	
The Average Damping Constant (N.s/m)			**42.265**

This page is blank

CHAPTER 3
METHODOLOGY

The methodology in this research will be divided into three main tasks, which are the linearization hand-derived of quarter-car model, the synthesis of LQR controller, and the virtual experimentation. For the task of virtually experimental made, the nonlinear multibody model will be built in "**Simscape Multibody**" in which the implementation of the designed controller (taken from simulation of linear equivalent model) validates the achievable suspension performance. To achieve later goal, the flow of works is shown in Figure 3.1
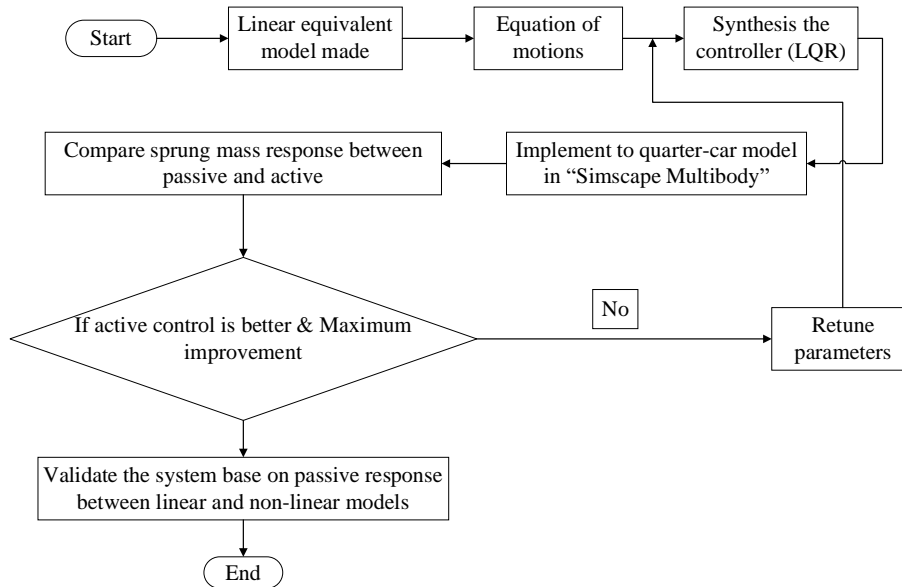
Figure 3.1 Flow of works

The methodology of the research will follow the task steps as shown in Figure 3.1. The first step of the works is linear equivalent made and deriving the equations of motion with compensated nonlinearity bloc of SAVGS (used the equations in [13]) that represent the dynamic response of multibody system. Then synthesize the LQR controller and tune of penalized parameters. The synthesized controller will simulate the linear equivalent model in "**MATLAB Simulink**". Furthermore, it will be thereafter implemented to the model of double wishbone

quarter-car, which will be virtually experimental. After that, the virtual experiment will be conducted under excitation mechanism (rotational cam) and compare the results of performance responses. If the active controller is better than passive one and maximum improvement reached, then the work is done. Otherwise, the penalized parameters will be retuned for other values. Lastly, the systems are validated based on the comparisons of sprung mass acceleration in passive case between linear and non-linear simulations.

3.1 Linearization of The Quarter-car Retrofitted with SAVGS

Nonlinear multi-body models of the vehicle and its suspension are available in software, as well as appropriate for virtually testing the SAVGS. However, they are not the best representation of the system for control synthesis. Linear models, on the other hand, enable the application of a wider range of control techniques and facilitate the study of the system dynamics [13]. A linear model of double wishbone quarter-car is required for LQR controller synthesis. In this section, the linearization of a quarter-car is discussed. Firstly, SAVGS concept prioritizes to be introduced, a single-link (SL) is retrofitted to the passive suspensions [19] as shown in Figure 3.2. This link that is jointed between the chassis (point G) and the upper-end of spring damper unit (point F) is actively rotated with respect to longitudinal axle (point G) by powered mechanism of electromechanical actuator. Torque T_{SL} acted at point G with respect to longitudinal axis. When no torque applied (left), the system is in passive static equilibrium state. In contrast, the system (right) variates suspension force and installation ratio as well [1].
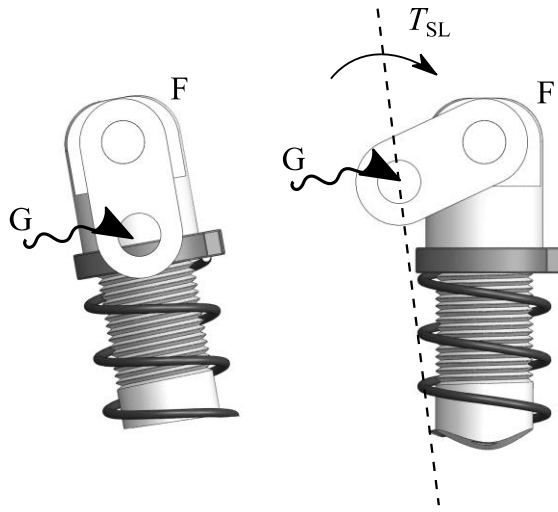
Figure 3.2 A retrofitted SL forms SAVGS

The parameter values for the suspension system are listed in Table 3.1 and two configurations of the designed double wishbone quarter-car model are shown in Figure 3.3. On the other hand, the notations of parameters are redefined and used in this work starting from this section.

Table 3.1 Suspension System Parameters

Parameter (unit)	Value	
	Configuration 1	Configuration 2
Sprung mass, m_s (kg)	0.46	
Unsprung mass, m_u (kg)	0.19	
Suspension stiffness coefficient, k_{Sus} (N/m)	782.94	
Suspension damping coefficient, c_{Sus} (N.s/m)	42.26	
Tire vertical stiffness, k_t (N/m)	2912.5	
Tire damping coefficient, c_t (N.s/m)	5.1	
Suspension unloaded stroke, l_{SD0} (mm)	18.095	
Single-link length, l_{SL} (mm)	5	
Low pass filter damping ratio, ζ_f (-)	0.707	
Low pass filter cut-off frequency, ω_c (rad/s)	varied	
Upper arm length, $\overline{BC}$ (mm)	81.54	91.43

Lower arm length, $\overline{AD}$ (mm)	101.34	111.26

(a)   (b)
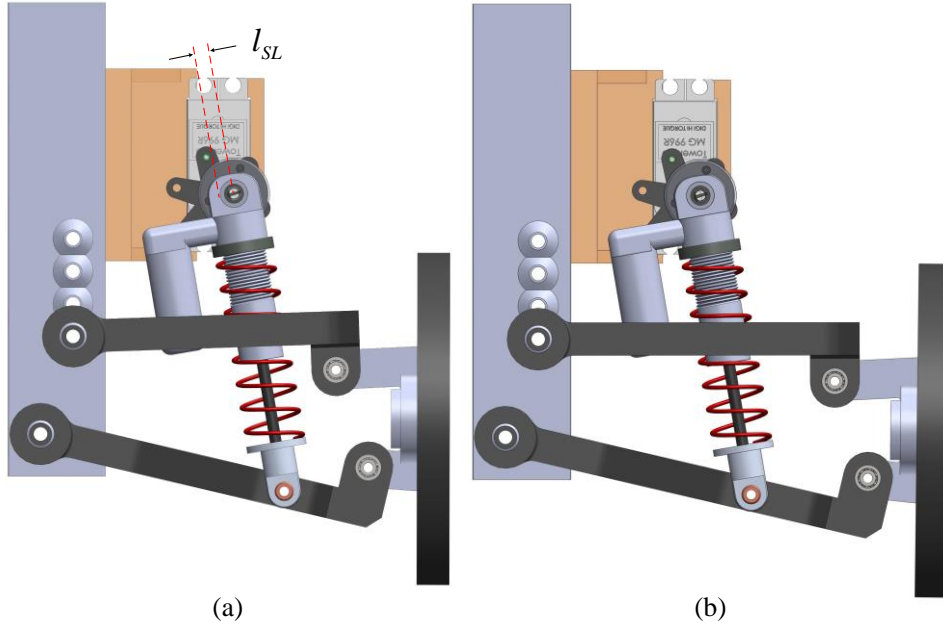
Figure 3.3 Double wishbone quarter-car model, configuration 1 (a) and configuration 2 (b)

3.1.1 Embodiment and Linearization

Figure 3.4 illustrates a planar quarter-car with double wishbone arrangement (a) and linear model (b). The former model presents wheel assembly (unsprung mass, m_u) connected to vehicle body (sprung mass, m_s) through lower arm ($\overline{AD}$) and upper arm ($\overline{BC}$) using the revolute joint. The suspension end-strut is variated due to the rotation of SL ($\overline{FG}$) respected to point G for any $\Delta\alpha_{SL}$ from the static equilibrium state, which is the minimal state of single-link $\alpha_{SL}^{(min)}$. The positive direction of α_{SL} is clockwise angle. This model (a) is made as equivalent as the latter model (b) through theoretical analysis proposed in section 2.2.
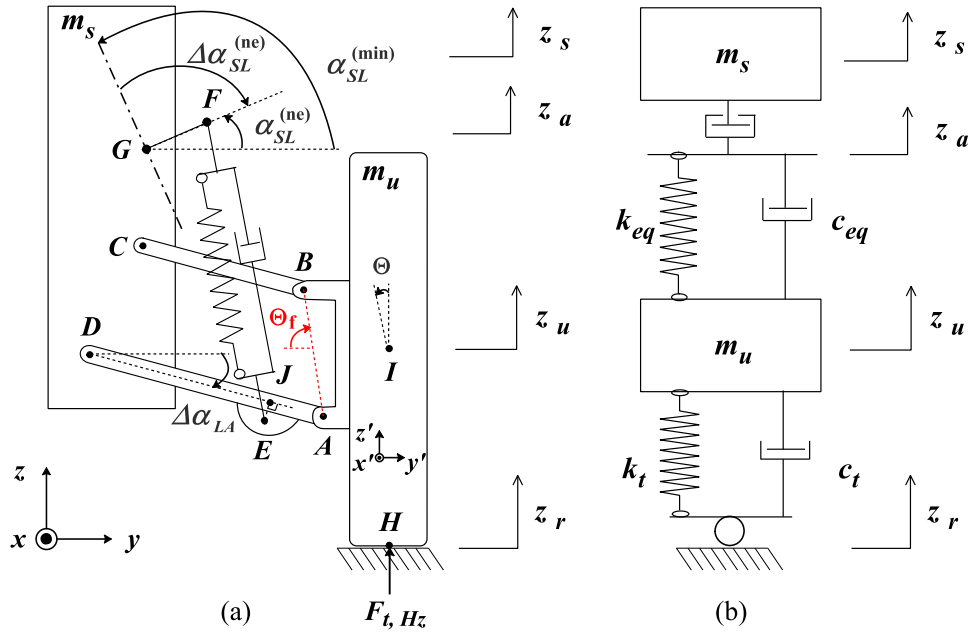
Figure 3.4 Quarter-car model, (a) a double wishbone arrangement and (b) a linear model

Quarter-car model in Figure 3.4 are defined their respective free body diagram in Figure 3.5 and Figure 3.6 for double wishbone arrangement and linear model, respectively. The wheel assembly bloc of double wishbone likely composes the force elements, such as F_A, F_B and F_D acting at point A, B and D, respectively. However, the forces acting at these points are considered to be diminished in this work, then $F_{k_{eq}}$ and $F_{c_{eq}}$ are the forces acted by suspension spring stiffness and damper of equivalent model instead. These two coefficients will be derived next.
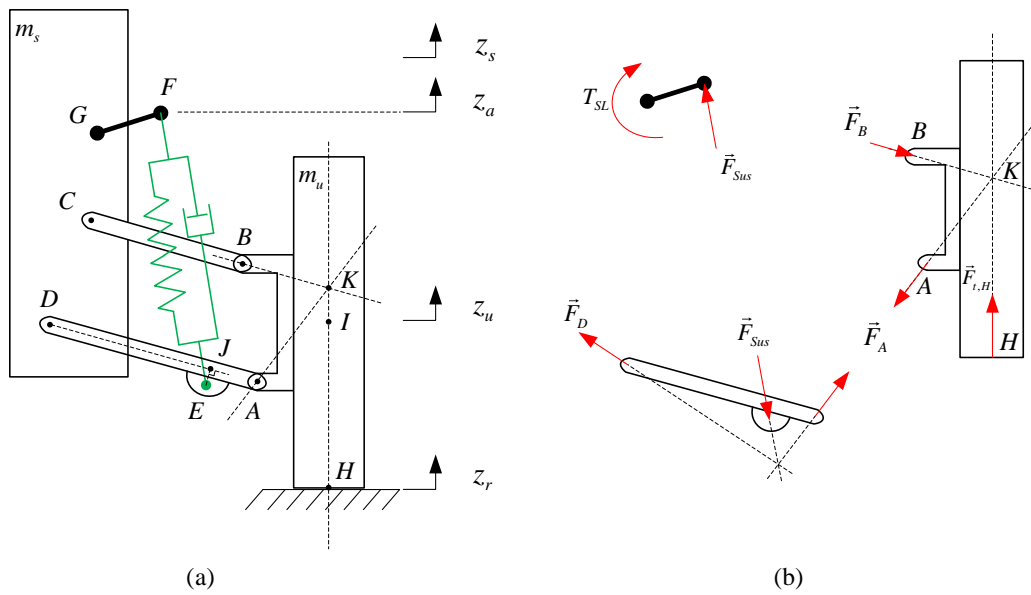
Figure 3.5 Quarter-car double wishbone (a), its free body diagram (b)
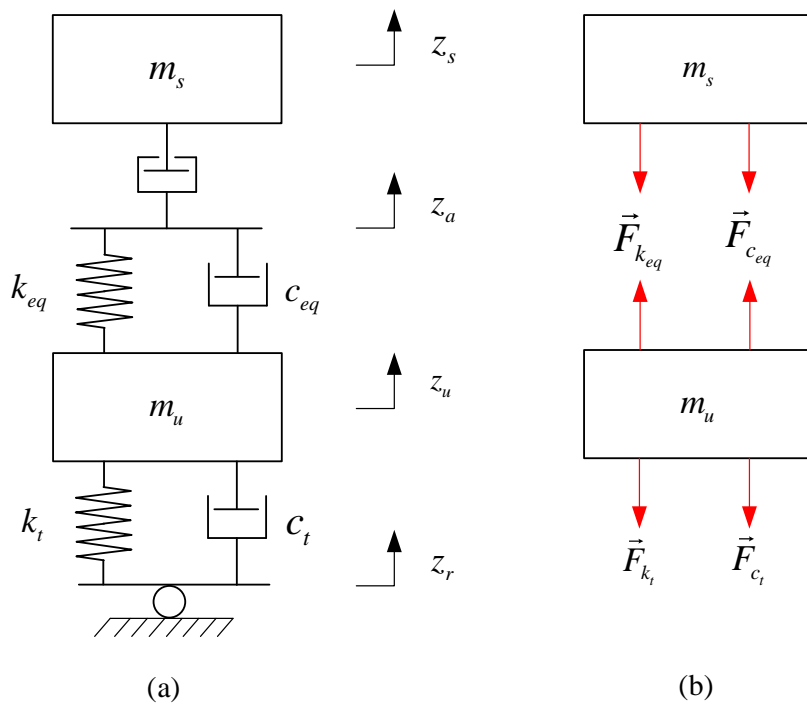
Figure 3.6 Quarter-car linear model (a), its free body diagram (b)

The linearization process flows are shown in Figure 3.7. As we see that we should find where is minimal state of single-link used as reference for system model. Then we will offset 90° angle of single-link from minimal state in order to

find the nominal state of single-link. The reasons why we need to find nominal state will discuss next. After the nominal state found, the equilibrium system will linear at that state. In each stage of flow will use some assumptions and formulation.
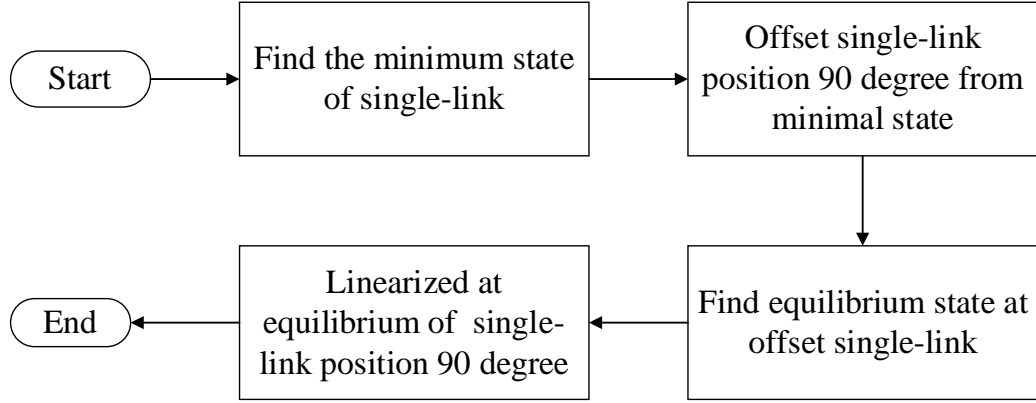
Figure 3.7 Linearization process flows

The three main assumptions considered from (2.2) to (2.4). **First assumption**, geometric equivalence: the vertical suspension deflections of model (a) and (b) in Figure 3.4 are the same and the tire deflections of those of model are the same as well. They are defined as

$$l_{SD} = z_a - z_u$$

(3.1)

$$l_t = z_u - z_r$$

where l_t is tire deflection

Second assumption, actuator equivalence: the power consumption of rotary actuator in model (a) is the same as that of linear actuator in model (b). The formulations can be derived as:

$$T_{SL}\dot{\alpha}_{SL} = F_{Sus}^* u$$

(3.2)

where $\dot{\alpha}_{SL}$ is the angular velocity of single-link, F_{Sus}^* is suspension force of model (b) and $u = \dot{z}_s - \dot{z}_a$ is linear equivalent actuator speed. T_{SL} is the torque applied to SL (model A) and can be obtained by applying the principle of virtual power to the SL. The formula illustrated that:

$$T_{SL} = F_{Sus}\frac{dl_{Sus}}{d\alpha_{SL}} \tag{3.3}$$

where F_{Sus} and l_{Sus} is suspension force and suspension length in model (a), respectively.

Starting from the static equilibrium state as stated in Figure 3.7, the suspension deflected length of model (a) is prioritized to be defined in order to figure out the $\alpha_{SL}^{(\min)}$ in the subsequent step. Applying the principle of virtual work in [2] acted to model (a) by suspension force:

$$F_{Sus}^{se}\delta l_{Sus} + m_u g \delta I_z = F_{t,H_z}^{se}\delta H_z \tag{3.4}$$

where F_{Sus}^{se}, F_{t,H_z}^{se}, g, and H_z are; the suspension force of model (a) at static equilibrium denoted as (se), the tire force at static equilibrium, the gravitational acceleration, and the displacement of point H in z direction; respectively. F_{t,H_z}^{se} and F_{Sus}^{se} can be defined as:

$$F_{t,H_z}^{se} = (m_s + m_u)g$$
$$\tag{3.5}$$
$$F_{Sus}^{se} = k_{Sus}(l_{Sus0} - l_{Sus}^{se})$$

where l_{Sus0} is unloaded suspension length and l_{Sus}^{se} is static suspension length of model (a).

Defining R_{Sus} as the installation ratio of suspension in model (a):

$$R_{Sus} = \frac{dl_{Sus}}{dI_z} = \frac{dl_{Sus}}{d\alpha_{LA}}\frac{d\alpha_{LA}}{dI_z} \tag{3.6}$$

where I_z is displacement of point I in z axis, α_{LA} is the clockwise angle of lower arm respected to horizontal axis, substituting (3.6) and (3.5) into (3.4) as well as assuming $\delta H_z \approx \delta I_z$ due to the small chamber angles, l_{Sus}^{se} can be determined as:

26

$$l_{Sus}^{se} = l_{Sus0} - \frac{m_s g}{k_{Sus} R_{Sus}^{se}} \qquad (3.7)$$

Now first step of linearization is found by calculating l_{Sus}^{se}, we can achieve $\alpha_{SL}^{(min)}$ by using the value of l_{Sus}^{se} set into **prototype** sketched in **Solidworks** as well as set single-link parallel with suspension. Then $\alpha_{SL}^{(min)} = 106.15°$ and $\alpha_{SL}^{(min)} = 106.33°$ respect to horizontal axis, for configuration 1 and configuration 2, respectively. Second step of linearization process is offset the position of single-link 90° of clockwise angle from minimal state. Third step is just do as similar as first step except shifting the position of single-link, then we got lower arm angle α_{LA} at equilibrium state as well as at nominal single-link state $\alpha_{SL}^{(nom)} = \alpha_{SL}^{(min)} + 90°$ by measuring in **Solidworks**. $\alpha_{LA} = -0.5442°$ and $\alpha_{LA} = -0.4732°$ for configuration 1 and configuration 2, respectively.

Kinematic linkage of arm wishbone can be represented a polygon with the relationship of cosine and sine theorem triangular.
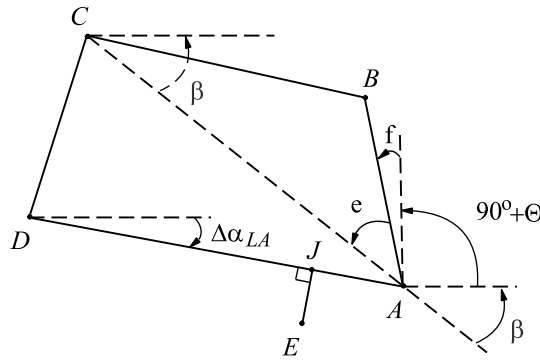
Figure 3.8 Kinematic linkage analysis of arm wishbone

The instant suspension length can be defined through kinematic analysis:

$$l_{Sus} = \overline{EF} = \sqrt{\overrightarrow{EF}.\overrightarrow{EF}} \qquad (3.8)$$

where $\overrightarrow{EF} = \overrightarrow{DF} - \overrightarrow{DE}$, $\overrightarrow{DF}$ and $\overrightarrow{DE}$ are 2-vector components which consist y and z directions. Their vector components are defined as:

$$\vec{DF} = \begin{bmatrix} \overline{DG}_y + l_{SL}\cos(\alpha_{SL}^{(min)} - \Delta\alpha_{SL}) \\ \overline{DG}_z + l_{SL}\sin(\alpha_{SL}^{(min)} - \Delta\alpha_{SL}) \end{bmatrix} \tag{3.9}$$

$$\vec{DE} = \begin{bmatrix} \overline{DJ}\cos(\Delta\alpha_{LA}) - \overline{EJ}\sin(\Delta\alpha_{LA}) \\ -\overline{DJ}\sin(\Delta\alpha_{LA}) - \overline{EJ}\cos(\Delta\alpha_{LA}) \end{bmatrix} \tag{3.10}$$

Substituting (3.9) and (3.10) into (3.8), then rewrite the instant suspension length in model (a)

$$l_{Sus} = \sqrt{\left(\overline{DG}_y + c_2 l_{SL} - c_1\overline{DJ} + s_1\overline{EJ}\right)^2 + \left(\overline{DG}_z + s_2 l_{SL} + s_1\overline{DJ} + c_1\overline{EJ}\right)^2} \tag{3.11}$$

Where

$c_1 = \cos(\Delta\alpha_{LA})$

$c_2 = \cos(\alpha_{SL}^{(min)} - \Delta\alpha_{SL})$,

$s_1 = \sin(\Delta\alpha_{LA})$,

$s_2 = \sin(\alpha_{SL}^{(min)} - \Delta\alpha_{SL})$,

$\overline{DG}_y = 54.69$ mm,

$\overline{DG}_z = 72.45$ mm,

$\overline{DJ} = 76.3637$ mm / $\overline{DJ} = 76.4725$ mm, for configuration 1 / configuration 2

$\overline{EJ} = 9.8779$ mm / $\overline{EJ} = 8.9967$ mm, for configuration 1 / configuration 2

and the subscript y and z indicate the projections in the y and z directions, respectively. Therefore, the term $\frac{dl_{Sus}}{d\alpha_{SL}}$ in (3.3) can calculated via the derivative of l_{Sus} in (3.11) respects to α_{SL}, derived as

$$\frac{dl_{Sus}}{d\alpha_{SL}} = \frac{1}{2l_{Sus}}\left\{ \begin{array}{l} -2l_{SL}s_2\left(\overline{DG}_y + l_{SL}c_2 - \overline{DJ}c_1 + \overline{EJ}s_1\right) \\ +2l_{SL}c_2\left(\overline{DG}_z + l_{SL}s_2 + \overline{DJ}s_1 + \overline{EJ}c_1\right) \end{array} \right\} \tag{3.12}$$

Or $\frac{dl_{Sus}}{d\alpha_{SL}}$ can be simplified as

$$\frac{dl_{Sus}}{d\alpha_{SL}} = \frac{l_{SL}}{l_{Sus}} \left[c_2 \overline{DG}_z - s_2 \overline{DG}_y + \overline{DJ}(c_1 s_2 + c_2 s_1) + \overline{EJ}(c_1 c_2 - s_1 s_2) \right] \qquad (3.13)$$

Furthermore, term $\frac{dl_{Sus}}{d\alpha_{LA}}$ in (3.6) can be derived via the derivative of l_{Sus} in (3.11) respects to α_{LA}:

$$\frac{dl_{Sus}}{d\alpha_{LA}} = \frac{1}{2l_{Sus}} \left\{ \begin{array}{l} 2(\overline{DJ}s_1 + \overline{EJ}c_1)(\overline{DG}_y + l_{SL}c_2 - \overline{DJ}c_1 + \overline{EJ}s_1) \\ +2(\overline{DJ}c_1 - \overline{EJ}s_1)(\overline{DG}_z + l_{SL}s_2 + \overline{DJ}s_1 + \overline{EJ}c_1) \end{array} \right\} \qquad (3.14)$$

final simplify term $\frac{dl_{Sus}}{d\alpha_{LA}}$ can be obtained:

$$\frac{dl_{Sus}}{d\alpha_{LA}} = \frac{1}{l_{Sus}} \left[a_1 s_1 + a_2 c_1 + l_{SL} \overline{DJ}(s_1 c_2 + s_2 c_1) + l_{SL} \overline{EJ}(c_1 c_2 - s_1 s_2) \right] \qquad (3.15)$$

where

$a_1 = \overline{DJ}.\overline{DG}_y - \overline{EJ}.\overline{DG}_z,$

$a_2 = \overline{EJ}.\overline{DG}_y + \overline{DJ}.\overline{DG}_z,$

Term $\frac{d\alpha_{LA}}{dI_z}$ in (3.6) as a part of calculating suspension installation ratio is more complicated to express this term. However, this term can be written that:

$$\frac{d\alpha_{LA}}{dI_z} = \frac{1}{\frac{dI_z}{d\alpha_{LA}}} \qquad (3.16)$$

where $\frac{dI_z}{d\alpha_{LA}}$ solely depends on the passive geometry, can be computed through kinematic analysis, firstly we have to define point I_z as a function of α_{LA}. This point can be written as

$$I_z = -s_1 \overline{AD} + \overline{AI}_{y'} \sin \Theta - \overline{AI}_{z'} \cos \Theta \qquad (3.17)$$

where Θ is the angle of wheel respects to vertical axis, the subscript y' and z' indicate the projections in the y' and z' directions, respectively; And

$\overline{AD} = 101.3373$ mm / $\overline{AD} = 111.2620$ mm , for configuration 1 / configuration 2

$\overline{AI}_{y'} = 20$ mm / $\overline{AI}_{y'} = 19.8$ mm, for configuration 1 / configuration 2

$\overline{AI}_{z'} = 15$ mm / $\overline{AI}_{z'} = 14.75$ mm, for configuration 1 / configuration 2

Derivation I_z with respect to α_{LA}, then

$$\frac{dI_z}{d\alpha_{LA}} = -c_1\overline{AD} + \overline{AI}_{y'}\frac{d\Theta}{d\alpha_{LA}}\cos\Theta - \overline{AI}_{z'}\frac{d\Theta}{d\alpha_{LA}}\sin\Theta \tag{3.18}$$

now we fact with another unknown Θ, which need to be defined as a function of α_{LA}. This wheel angle can be defined via kinematic analysis of linkages in Figure 3.8.

$$\Theta = 180° - 90° - \beta - e - f \tag{3.19}$$

Starting from β angle, it can be written as

$$\beta = \arccos\left(\frac{\overrightarrow{AC}_y}{\overline{AC}}\right) \tag{3.20}$$

where $\overline{AC} = \sqrt{\left(\overrightarrow{AC}_y\right)^2 + \left(\overrightarrow{AC}_z\right)^2}$ and

$\overline{AC}_y = c_1\overline{AD} - \overline{CD}_y$

$\overline{AC}_z = s_1\overline{AD} + \overline{CD}_z$

$\overline{CD}_y = 10$ mm

$\overline{CD}_z = 30$ mm

e in (3.19) can be defined by using "**Law of cosine**", applying to triangular ABC

$$e = \arccos\left(\frac{\overline{AB}^2 + \overline{AC}^2 - \overline{BC}^2}{2\overline{AB}.\overline{AC}}\right) \tag{3.21}$$

where

$\overline{AB} = 31.6227$ mm / $\overline{AB} = 31.2795$ mm, for configuration 1 / configuration 2

$\overline{BC} = 81.5429$ mm / $\overline{BC} = 91.4289$ mm, for configuration 1 / configuration 2

f in (3.19) is the angle between $\overline{AB}$ and wheel. Therefore, $f = 18.435°$ / $f = 19.419°$, for configuration 1 / configuration 2, respectively. The wheel angle Θ in (3.19) can be rewritten by substituting (3.20), (3.21) and f:

$$\Theta = \Theta_f - \arccos\left(\frac{\overline{AC}_y}{\overline{AC}}\right) - \arccos\left(\frac{\overline{AB}^2 + \overline{AC}^2 - \overline{BC}^2}{2\overline{AB}.\overline{AC}}\right) \tag{3.22}$$

where Θ_f is the angle between $\overline{AB}$ and y' axis, $\Theta_f = 71.565º/\Theta_f = 70.58º$ for configuration 1/configuration 2, respectively.

Now Θ is obtained, then term $\frac{\partial\Theta}{\partial\alpha_{LA}}$ in (3.18) can be obtained by derivation of Θ respects with α_{LA}.

$$\frac{d\Theta}{d\alpha_{LA}} = \left\{ \begin{array}{c} \dfrac{\overline{AC}_y'\overline{AC} - \overline{AC}_y\overline{AC}'}{\overline{AC}^2\sqrt{1 - b_1^2}} \\[2em] -\dfrac{(\overline{AC}^2)'(2\overline{AB}.\overline{AC}) - 2\overline{AB}(\overline{AB}^2 + \overline{AC}^2 - \overline{BC}^2)\overline{AC}'}{(2\overline{AB}.\overline{AC})^2\sqrt{1 - b_2^2}} \end{array} \right\} \tag{3.23}$$

Where

$\overline{AC}_y' = -s_1\overline{AD}$

$\overline{AC}' = \frac{\overline{AD}}{\overline{AC}}\left(c_1\overline{CD}_z + s_1\overline{CD}_y\right)$

$(\overline{AC}^2)' = 2\overline{AC}'.\overline{AC}$

$b_1 = \frac{\overline{AC}_y}{\overline{AC}}$

$b_2 = \frac{\overline{AB}^2 + \overline{AC}^2 - \overline{BC}^2}{2\overline{AB}.\overline{AC}}$

The suspension force F_{Sus} in model (a) and that of F_{Sus}^* in model (b) are related such that:

$$F_{Sus}^* = R_{Sus}F_{Sus} \tag{3.24}$$

The displacement of point F in z direction in model (a) can be reversibly transformed that of z_a in model (b) through Γ function as stated in (2.1), which is shown that:

$$\Gamma = \frac{u}{\dot{\alpha}_{SL}} \tag{3.25}$$

Substituting (3.3) and (3.24) to (3.2), Γ can be defined that:

$$u = \frac{1}{R_{Sus}} \frac{dl_{Sus}}{d\alpha_{SL}} \dot{\alpha}_{SL} \Rightarrow \Gamma = \frac{1}{R_{Sus}} \frac{dl_{Sus}}{d\alpha_{SL}} \qquad (3.26)$$

Starting from now, the quarter-car model (a) will be linearized at a trim state corresponding to the nominal state ($\Delta\alpha_{SL}^{(ne)} = 90^o$) due to effective control at that position [13]. Figure 3.9 illustrated the variation of Γ function among variables $\Delta\alpha_{SL}$ and $\Delta\alpha_{LA}$. The lower arm angles ranged from static equilibrium to maximum suspension deflection are -0.4205^o to -10.5186^o and from -0.3398^o to -9.8699^o for configuration 1 and configuration 2, respectively. It illustrated that Γ significantly depended on $\Delta\alpha_{SL}$; at $\Delta\alpha_{SL} = 0^o$ and $\Delta\alpha_{SL} = 180^o$, it across the zero values. However, it is less effected by $\Delta\alpha_{LA}$. Variation of Γ is reasonably small when comparing of the nominal lower arm angle state (-5.32^o and -5.04^o for configurations 1 and 2, respectively) to its static state, with offset bandwidth ~0.39% and ~1.72% for configurations 1 and 2, respectively.
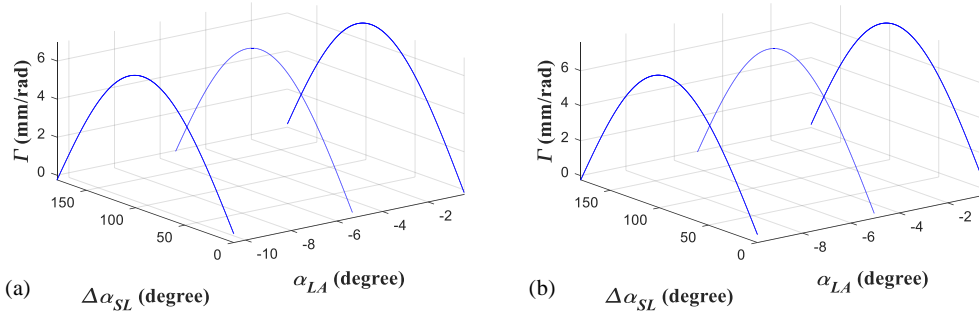
Figure 3.9 Illustration of Γ as a function of $\Delta\alpha_{SL} = \alpha_{SL} - \alpha_{SL}^{min}$, (a) for configuration 1 and (b) for configuration 2

Figure 3.10 illustrates the Γ magnitude along the variations of single-link angle, the lower arm angles are set at static equilibrium state of each respective configuration (-0.4205^o and -0.3398^o for configurations 1 and 2, respectively). At nominal state of single-link angle ($\Delta\alpha_{SL}^{nom} = 90^o$), $\Gamma_{C1} = 6.926$ mm/rad for configuration 1 somewhat is smaller than that of configuration 2, which is $\Gamma_{C2} = 7.562$ mm/rad
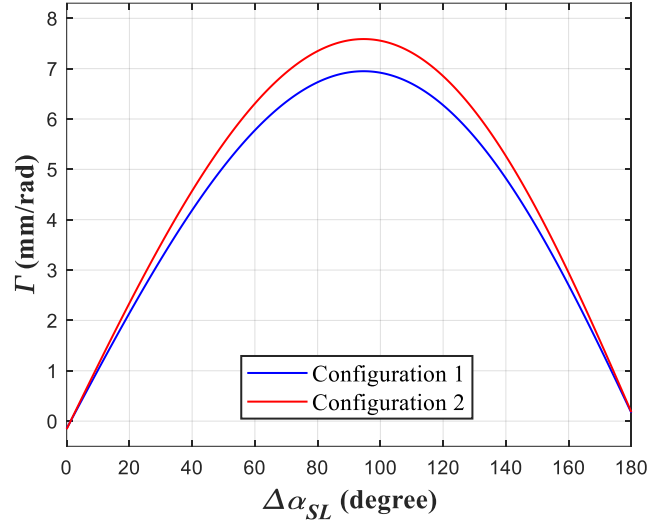
Figure 3.10 Variations of Γ along $\Delta\alpha_{SL}$ at respective static equilibrium of each configuration

These Γ curves at static state of lower arm angle can be interpreted by polynomial functions derived for system configuration 1 and configuration 2, respectively:

$$\begin{cases} \Gamma_{Config\ 1} = 0.2203\Delta\alpha_{SL}^4 - 1.5543\Delta\alpha_{SL}^3 + 0.7171\Delta\alpha_{SL}^2 + 6.3324\Delta\alpha_{SL} \\ \qquad\qquad -0.1069; \text{where } 0 \leq \Delta\alpha_{SL} \leq 180^o \end{cases} \quad (3.27)$$

$$\begin{cases} \Gamma_{Config\ 2} = 0.2407\Delta\alpha_{SL}^4 - 1.6997\Delta\alpha_{SL}^3 + 0.7925\Delta\alpha_{SL}^2 + 6.9051\Delta\alpha_{SL} \\ \qquad\qquad -0.1143; \text{where } 0 \leq \Delta\alpha_{SL} \leq 180^o \end{cases} \quad (3.28)$$

k_{eq} and c_{eq} is equivalent spring stiffness and damping coefficients from model (a) to model (b). **Third assumption** taken in (2.4), the rate of change of energy stored as well as that of energy dissipation in model (a) must be the same as in model (b).

$$k_{eq} = k_{Sus}R_{Sus}^2 - F_{Sus}\frac{dR_{Sus}}{dI_z}, \qquad c_{eq} = c_{Sus}R_{Sus}^2 \qquad (3.29)$$

Figure 3.11 and Figure 3.12 are estimated values of k_{eq} and c_{eq}, respectively. The lower arm angles of each respective configuration are ranged the same as in Figure

3.9. At fixed SL angle, k_{eq} and c_{eq} are slightly changed, as well as at low slope when comparing among both configurations along the variation of lower arm angle. In contrast, both values are significantly suffered by the variation of SL angle. However at the minimum SL angle ($\Delta\alpha_{SL} = 0^o$) and the maximum SL angle ($\Delta\alpha_{SL} = 180^o$), k_{eq} and c_{eq} tent to equal to their values at those states.
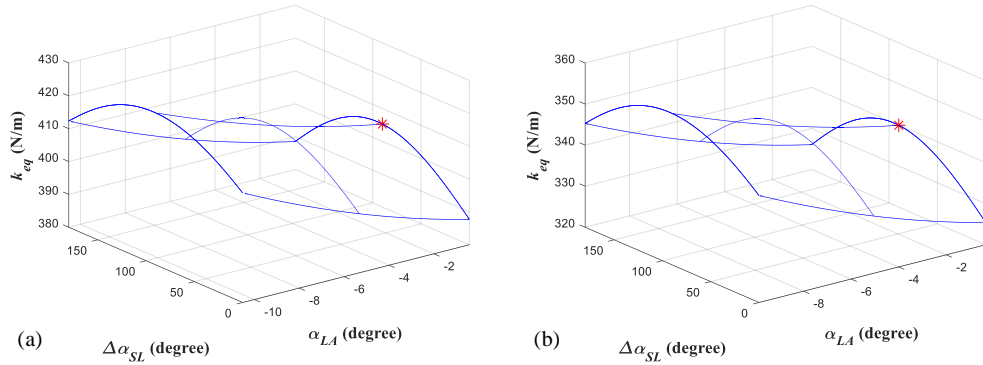
Figure 3.11 Illustration of k_{eq}, (a) for configuration 1 and (b) for configuration 2
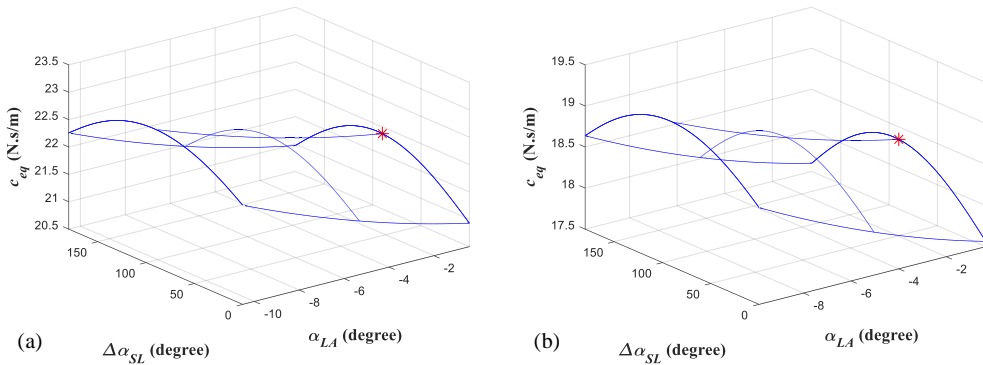
Figure 3.12 Illustration of c_{eq}, (a) for configuration 1 and (b) for configuration 2

Figure 3.13 and Figure 3.14 are the comparisons of equivalent spring stiffness and damping coefficients between configuration 1 and configuration 2, respectively. k_{eq} and c_{eq} at the nominal state (asterisk point) are a pair of configuration 1 and configuration 2; 405.3 N/m and 21.88 N.s/m, and 339.93 N/m and 18.35 N.s/m; respectively. Observing on these, k_{eq} and c_{eq} are larger than those of value in configuration 2.
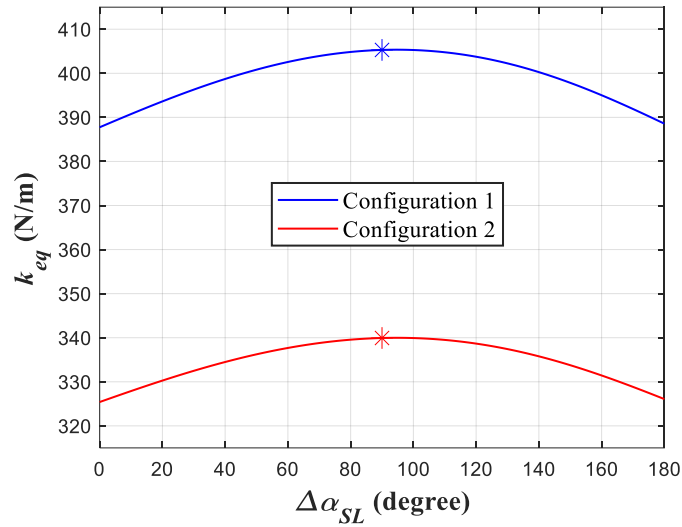
Figure 3.13 Variations of k_{eq} along $\Delta\alpha_{SL}$ at respective static equilibrium of each configuration
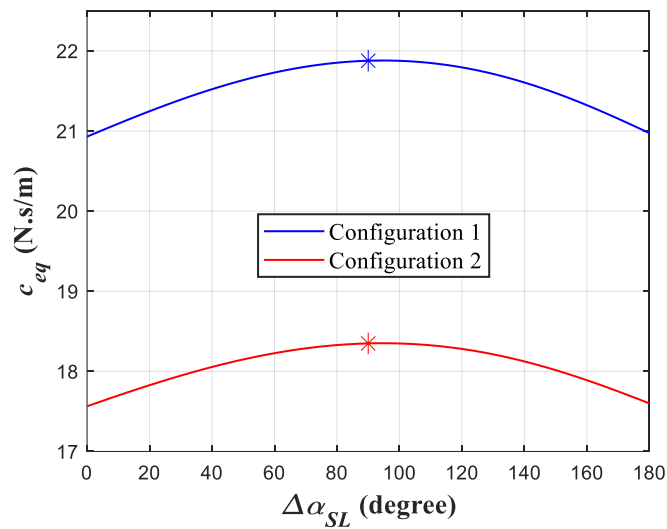
Figure 3.14 Variations of c_{eq} along $\Delta\alpha_{SL}$ at respective static equilibrium of each configuration

Lastly, the equation motions of linear equivalent model of quarter-car retrofitted with SAVGS deriving from free body diagram in Figure 3.6 are defined as:

$$m_s \ddot{z}_s = -k_{eq}(z_a - z_u) - c_{eq}(\dot{z}_s - \dot{z}_u) + c_{eq}u$$

$$m_u \ddot{z}_u = k_{eq}(z_a - z_u) + c_{eq}(\dot{z}_s - \dot{z}_u) - k_t(z_u - z_r) - c_t(\dot{z}_u - \dot{z}_r) \qquad (3.30)$$
$$- c_{eq}u$$

3.2 Controller Synthesis

In this section controller designed is discussed. Before we design controller, let us introduce some theories control. Regard with systems controller, it is fundamentally required dynamic equations which represent dynamic behaviours of full multibody systems. The dynamic equations can be presented by transfer function or state space equation. Transfer function represented in the frequency domain is classified as classical control theory. In contrast, systems were represented in the time domain by a type of differential equation called a state space equation. Performance and robustness specifications also were specified in the time domain, often in the form of a quadratic performance index.

Linear Quadratic Regulator is such a type of optimal control as well as used for linear time-invariant system. A state-space representation for a linear time-invariant system has the general form

$$\dot{x}(t) = Ax(t) + Bu(t)$$

$$y(t) = Cx(t) + Du(t) \qquad (3.31)$$

$$x(t_0) = 0$$

in which $x(t) = 0$ is the n-dimensional state vector, $u(t)$ is the m-dimensional input vector and $y(t)$ is the p-dimensional output vector. The state vector $x(t)$ is composed of a minimum set of internal system variables that uniquely describes the future response of the system given the current state, the input, and the dynamic equations. The input vector $u(t)$ contains variables used to actuate the system, and the output vector $y(t)$ contains the measurable quantities.

3.2.1 Controller Design Criteria

As a first step of design controller, in this work we have to check our system with three main criteria which exist in [21]

1. *Controllability*

We consider the linear time-invariant state differential equation

$$\dot{x}(t) = Ax(t) + Bu(t) \tag{3.32}$$

$$x(t_0) = x_0$$

Definition A state $x \in \mathbb{R}^n$ is **controllable to the origin** if for a given initial time t_0 there exists a finite final time $t_f > t_0$ and a piecewise continuous input signal $u(.)$ defined on $[t_0, t_f]$ such that with initial state $x(t_0) = x_0$, the final state satisfies

$$x(t_f) = e^{A(t_f - t_0)}x_0 + \int_{t_0}^{t_f} e^{A(t_f - \tau)} Bu(\tau)d\tau = 0 \in \mathbb{R}^n \tag{3.33}$$

The state equation (3.32) is controllable if every state $x \in \mathbb{R}^n$ is controllable to the origin. The linear state is controllable if and only if

$$rank[B \quad AB \quad A^2 B \quad \cdots \quad A^{n-1}B] = n \tag{3.34}$$

> ➢ We refer to this matrix as the **controllability matrix** and denote it by *CM*
> ➢ The theorem asserts that controllability of the state equation (3.32) is equivalent to *CM* having full-row rank
> ➢ For the general multiple-input case, *CM* has dimension $n \times (nm)$ and therefore has more columns than rows in the multiple-input case.
> ➢ For the single-input case, *CM* has dimension $n \times n$
>> ❖ a single-input linear state equation is controllable if and only if the associated controllability matrix is non-singular.
>> ❖ We can check that *CM* is non-singular by verifying that *CM* has a nonzero determinant.

2. *Observability*

We consider the linear time-invariant state differential equation

$$\dot{x}(t) = Ax(t) + Bu(t)$$

$$y(t) = Cx(t) + Du(t) \tag{3.35}$$

$$x(t_0) = x_0$$

we assume that the input signal $u(t)$ and the output signal $y(t)$ can be measured over a finite time interval. if the initial state can be uniquely determined, then this, along with knowledge of the input signal, yields the entire state trajectory via

$$x(t) = e^{A(t-t_0)}x_0 + \int_{t_0}^{t} e^{A(t-\tau)} Bu(\tau)d\tau \text{ for } t \geq t_0 \tag{3.36}$$

the zero-state response can be extracted from the complete response $y(t)$,

$$y(t) - \left[\int_{t_0}^{t} Ce^{A(t-\tau)}Bu(\tau)d\tau + Du(t) \right] = Ce^{A(t-t_0)}x_0 \tag{3.37}$$

assume without loss of generality that $u(t) \equiv 0$ for all $t \geq t_0$ and instead consider the homogeneous state equation

$$\dot{x}(t) = Ax(t)$$

$$y(t) = Cx(t) \tag{3.38}$$

$$x(t_0) = x_0$$

Definition: A state $x0 \in \mathbb{R}^n$ is **unobservable** if the zero-input response of the linear state equation (3.35) with initial state $x(t_0) = x_0$ is $y(t) \equiv 0$ for all $t \geq t_0$. The state equation (3.35) is **observable** if the zero vector $0 \in \mathbb{R}^n$ is the only unobservable state. The linear state is observable if and only if

$$rank \begin{bmatrix} C \\ CA \\ CA^2 \\ \vdots \\ CA^{n-1} \end{bmatrix} = n \qquad (3.39)$$

➢ We refer to this matrix as the **observability matrix** and denote it as *OM*.

➢ For the general multiple-output case, *OM* has dimension $(np) \times n$ and therefore has more rows than columns. Consequently, *OM* satisfying the preceding rank condition is said to have full-column rank.

➢ For the single-output case, *OM* is a square n ×n matrix.

❖ A single-output linear state equation is observable if and only if the observability matrix is non-singular.

❖ We can check that *OM* is non-singular by verifying that it has a nonzero determinant.

3. *Internal Stability*

Our ultimate focus is on the homogeneous linear time-invariant state equation

$$\dot{x}(t) = Ax(t)$$

$$x(0) = x_0 \qquad (3.40)$$

for which $\tilde{x} = 0 \in \mathbb{R}^n$ is seen easily to be an equilibrium state. The equilibrium state $\tilde{x} = 0$ of Equation (3.40) is:

➢ **Stable** if and only if all eigenvalues of *A* have a nonpositive real part and the geometric multiplicity of any eigenvalue with zero real part equals the associated algebraic multiplicity.

➢ **(Globally) asymptotically stable** if and only if every eigenvalue of *A* has strictly negative real part.

Lyapunov Stability Analysis, the fundamental discovery of Lyapunov is that the equilibrium $\tilde{x} = 0$ is

- ➢ **Stable** if $\dot{W}(x)$ is **negative semidefinite**; that is, $\dot{W}(x) \le 0$ for all x in a neighbourhood of the origin.
- ➢ **Asymptotically stable** if $\dot{W}(x)$ is **negative definite**; that is, $\dot{W}(x) < 0$ for all $x \ne 0$ in a neighbourhood of the origin.

A positive-definite function $W(x)$ for which $\dot{W}(x)$ is at least negative semidefinite is called a **Lyapunov function**. Stability of an equilibrium can be determined directly from the system dynamics without explicit knowledge of system trajectories. This approach is referred to as **Lyapunov's direct method**.

For the linear state equation (3.40), Lyapunov stability analysis can be made much more explicit. We can focus on energy-like functions that are quadratic forms given by

$$W(x) = x^T P' x \qquad (3.41)$$

in which the associated matrix P' is symmetric. A quadratic form is a positive-definite function over all of $\mathbb{R}^n$ if and only if P' is a positive-definite symmetric matrix. A symmetric $n \times n$ matrix $\boldsymbol{P'}$ is **positive definite** if and only if every eigenvalue of P' is real and positive

The gradient of the quadratic form $W(x) = x^T P' x$ is

$$\frac{\partial W}{\partial x}(x) = 2x^T P' \qquad (3.42)$$

Using this and the linear dynamics in (3.40), we can compute $\dot{W}(x)$ according to

$$\dot{W}(x) = \frac{\partial W}{\partial x}(x) f(x)$$

$$= (2x^T P')(Ax) \qquad (3.43)$$

$$= x^T A^T P' x + x^T P' A x$$

$$= x^T (A^T P' + P' A) x$$

A sufficient condition for asymptotic stability of the equilibrium state $\tilde{x} = 0$ is the existence of a **symmetric positive-definite matrix** $\boldsymbol{P'}$ for which $A^T P' + P'A$ is negative definite.

MATLAB for Stability Analysis, the following MATLAB function is useful for Lyapunov stability analysis:

$\boldsymbol{lyap(A^T, Q')}$ Solve $\boldsymbol{A^T P' + P'A = -Q'}$ for matrix $\boldsymbol{P'}$, given a positive-definite matrix $\boldsymbol{Q'}$.

3.2.2 LQR Controller Design for Suspension Plant

We now turn our attention to the steady-state linear quadratic regulator problem, in which the performance index becomes

$$J = \frac{1}{2} \int_0^\infty [x^T(t)Qx(t) + u^T(t)Ru(t)]dt \tag{3.44}$$

We assume that the weighting matrices $\boldsymbol{Q}$ and $\boldsymbol{R}$ are each symmetric, with $\boldsymbol{Q}$ positive semidefinite and $\boldsymbol{R}$ positive definite. Regulator design for a linear time-invariant state equation with the goal of minimizing a quadratic performance index naturally is referred to as the linear quadratic regulator (LQR) problem. In contrast to the challenges that arise in the general nonlinear optimal control problem, the linear quadratic regulator problem admits an analytical solution that we will derive in the sequel.

Here we explicitly see the manner in which the quadratic performance index captures a trade-off between regulation performance and control effort. In particular, if the quadratic terms involving the state are "**large**" compared with the quadratic term involving the input, then the optimal state trajectory will exhibit "**good**" regulation performance in that the response to a nonzero initial state will return rapidly to the equilibrium state at the origin, but this may come at the expense of "**large**" control energy. Conversely, if the input is penalized more heavily than the state, then the optimal control signal may not require a great deal of energy, but the regulation performance may not be acceptable.

Defining $x_1 = z_a - z_u, x_2 = z_u - z_r, x_3 = \dot{z}_s, x_4 = \dot{z}_u$ and $w = \dot{z}_r$ as the suspension deflection, the tire deflection, the sprung mass velocity, the unsprung

mass velocity and the disturbance input; respectively. Substituting these variables into (3.30). Then, the state space form of quarter-car suspension system can be derived as in algebraic form:

$$\dot{x}_p(t) = A_p x_p(t) + B_u u(t) + B_w w(t)$$

$$y(t) = C_p x_p(t)$$

(3.45)

where $x_p = [x_1 \ x_2 \ x_3 \ x_4]^T$ is the suspension system state at time t,

$$A_p = \begin{bmatrix} 0 & 0 & 1 & -1 \\ 0 & 0 & 0 & 1 \\ -\dfrac{k_{eq}}{m_s} & 0 & -\dfrac{c_{eq}}{m_s} & \dfrac{c_{eq}}{m_s} \\ \dfrac{k_{eq}}{m_u} & -\dfrac{k_t}{m_u} & \dfrac{c_{eq}}{m_u} & -\dfrac{c_{eq}+c_t}{m_u} \end{bmatrix}$$

$$B_u = \begin{bmatrix} -1 \\ 0 \\ \dfrac{c_{eq}}{m_s} \\ -\dfrac{c_{eq}}{m_u} \end{bmatrix}$$

(3.46)

$$B_w = \begin{bmatrix} 0 \\ -1 \\ 0 \\ \dfrac{c_t}{m_u} \end{bmatrix}, \text{ and}$$

$$C_p = \begin{bmatrix} 1 & 0 & 0 & 0 \\ 0 & 1 & 0 & 0 \\ 0 & 0 & 1 & 0 \\ 0 & 0 & 0 & 1 \end{bmatrix}$$

The passive case is used the same suspension system state as the active case except ignoring the term of $B_u u(t)$.

Now we get the state space matrix equation so that the aforementioned controller design criteria are discussed as the following:

1. *Controllability checked*

Substituting k_{eq}, c_{eq} found in Sec 3.1.1 and others parameter in Table 3.1 into equation (3.46), then we got:

➢ Configuration 1:

$$A_p = \begin{bmatrix} 0 & 0 & 1 & -1 \\ 0 & 0 & 0 & 1 \\ -881.09 & 0 & -47.565 & 47.565 \\ 2.131 \times 10^3 & -1.531 \times 10^4 & 115.03 & -141.84 \end{bmatrix}$$

$$B_u = \begin{bmatrix} -1 \\ 0 \\ 47.565 \\ -115.03 \end{bmatrix}$$

Implementing (3.34) then **controllability matrix CM** derived as:

$$CM = \begin{bmatrix} B_u & A_p B_u & A_p^2 B_u & A_p^3 B_u \end{bmatrix} =$$

$$\begin{bmatrix} -1 & 162.6 & -2.651 \times 10^4 & 2.586 \times 10^6 \\ 0 & -115.03 & 1.966 \times 10^4 & -1.469 \times 10^6 \\ 47.565 & -6852.8 & 1.118 \times 10^6 & -9.966 \times 10^7 \\ -115.03 & 1.966 \times 10^4 & -1.469 \times 10^6 & -2.058 \times 10^7 \end{bmatrix}$$

Calculating determinant of matrix CM

$\det(CM) = -2.706 \times 10^{15} \neq 0$, hence controllability matrix of suspension system configuration 1 is full rank matrix.

➢ Configuration 2

$$A_p = \begin{bmatrix} 0 & 0 & 1 & -1 \\ 0 & 0 & 0 & 1 \\ -738.98 & 0 & -39.891 & 39.891 \\ 1.787 \times 10^3 & -1.531 \times 10^4 & 96.472 & -123.28 \end{bmatrix}$$

$$B_u = \begin{bmatrix} -1 \\ 0 \\ 39.891 \\ -96.472 \end{bmatrix}$$

Similar as in previously, then **controllability matrix CM** derived as:

$$CM = \begin{bmatrix} -1 & 136.36 & -1.866 \times 10^4 & 1.096 \times 10^6 \\ 0 & -96.472 & 1.395 \times 10^4 & -4.530 \times 10^5 \\ 39.891 & -4700.7 & 6.434 \times 10^5 & -2.995 \times 10^7 \\ -96.472 & 1.395 \times 10^4 & -4.530 \times 10^5 & -1.291 \times 10^8 \end{bmatrix}$$

Calculating determinant of matrix CM

$\det(CM) = -1.596 \times 10^{15} \neq 0$, hence controllability matrix of suspension system configuration 2 is full rank matrix.

Therefore, both configurations of suspension system are assumed to be controllable.

2. *Observability checked*

Defining observability matrix OM in (3.39)

$$OM = \begin{bmatrix} C_p \\ C_p A_p \\ C_p A_p^2 \\ C_p A_p^3 \end{bmatrix}, \text{ then}$$

➢ Configuration 1

$OM =$

$$\begin{bmatrix}
1 & 0 & 0 & 0 \\
0 & 1 & 0 & 0 \\
0 & 0 & 1 & 0 \\
0 & 0 & 0 & 1 \\
0 & 0 & 1 & -1 \\
0 & 0 & 0 & 1 \\
-881.09 & 0 & -47.565 & 47.565 \\
2130.8 & -1.531 \times 10^4 & 115.03 & -141.84 \\
-3011.9 & 1.531 \times 10^4 & -162.6 & 189.41 \\
2130.8 & -1.531 \times 10^4 & 115.03 & -141.84 \\
1.433 \times 10^5 & -7.283 \times 10^5 & 6852.8 & -8128.2 \\
-4.036 \times 10^5 & 2.172 \times 10^6 & -1.966 \times 10^4 & 8148.1 \\
5.468 \times 10^5 & -2.9 \times 10^6 & 2.651 \times 10^4 & -1.628 \times 10^4 \\
-4.036 \times 10^5 & 2.172 \times 10^6 & -1.966 \times 10^4 & 8148.1 \\
-2.336 \times 10^7 & 1.245 \times 10^8 & -1.118 \times 10^6 & 6.073 \times 10^5 \\
3.468 \times 10^7 & -1.248 \times 10^8 & 1.469 \times 10^6 & 4.847 \times 10^5
\end{bmatrix}$$

Rank matrix OM can be calculated in MATLAB via $rank(OM)$, and we found that $rank(OM) = 4$, which **full-column rank** matrix.

➢ Configuration 2

$$OM = \begin{bmatrix} 1 & 0 & 0 & 0 \\ 0 & 1 & 0 & 0 \\ 0 & 0 & 1 & 0 \\ 0 & 0 & 0 & 1 \\ 0 & 0 & 1 & -1 \\ 0 & 0 & 0 & 1 \\ -738.98 & 0 & -39.891 & 39.891 \\ 1787.1 & -1.531 \times 10^4 & 96.472 & -123.28 \\ -2526.1 & 1.531 \times 10^4 & -136.36 & 163.18 \\ 1787.1 & -1.531 \times 10^4 & 96.472 & -123.28 \\ 1.008 \times 10^5 & -6.108 \times 10^5 & 4700.7 & -5770.3 \\ -2.916 \times 10^5 & 1.888 \times 10^6 & -1.395 \times 10^4 & 1948.4 \\ 3.924 \times 10^5 & -2.499 \times 10^6 & 1.866 \times 10^4 & -7718.7 \\ -2.916 \times 10^5 & 1.888 \times 10^6 & -1.395 \times 10^4 & 1948.4 \\ -1.379 \times 10^7 & 8.835 \times 10^7 & -6.434 \times 10^5 & 1.873 \times 10^5 \\ 1.379 \times 10^7 & -2.983 \times 10^7 & 4.530 \times 10^5 & 1.382 \times 10^6 \end{bmatrix}$$

we found that $rank(OM) = 4$, which **full-column rank** matrix.

Therefore, both configurations of suspension system are assumed to be observable.

3. *Internal stability checked*

We will use **MATLAB** toolbox stated in previous section 3.2.1 to analyse the stability-checked of our system. Suppose that, taken $Q' = I$ for simplicity (obviously a symmetric positive-definite matrix) and proceed to solve the Lyapunov matrix

➢ Suspension configuration 1

The associated matrix P' gotten as:

$$P' = \begin{bmatrix} 11.386 & 6.284 & 1.132 \times 10^{-1} & 4.659 \times 10^{-2} \\ 6.284 & 108.77 & -8.096 \times 10^{-1} & 3.265 \times 10^{-5} \\ 1.132 \times 10^{-1} & -8.096 \times 10^{-1} & 1.997 \times 10^{-2} & 2.925 \times 10^{-3} \\ 4.659 \times 10^{-2} & 3.265 \times 10^{-5} & 2.925 \times 10^{-3} & 4.178 \times 10^{-3} \end{bmatrix}$$

Eigenvalues of matrix P' can be calculated via $eig(P')$ in MATLAB. Therefore, getting $\lambda_1 = 3.368 \times 10^{-3}$, $\lambda_2 = 1.223 \times 10^{-2}$, $\lambda_3 = 10.985$, and $\lambda_4 = 109.18$. All eigenvalues of matrix P' are real and positive.

➢ Suspension configuration 2

The associated matrix P' gotten as:

$$P' =$$

$$\begin{bmatrix} 11.056 & 5.799 & 9.538 \times 10^{-2} & 3.916 \times 10^{-2} \\ 5.799 & 107.76 & -8.113 \times 10^{-1} & 3.265 \times 10^{-5} \\ 9.538 \times 10^{-2} & -8.113 \times 10^{-1} & 2.095 \times 10^{-2} & 2.493 \times 10^{-3} \\ 3.916 \times 10^{-2} & 3.265 \times 10^{-5} & 2.493 \times 10^{-3} & 4.545 \times 10^{-3} \end{bmatrix}$$

Therefore, getting $\lambda_1 = 3.967 \times 10^{-3}$, $\lambda_2 = 1.348 \times 10^{-2}$, $\lambda_3 = 10.712$, and $\lambda_4 = 108.11$. All eigenvalues of matrix P' are real and positive. Hence, suspension system of both configurations is assumed to be **Asymptotically stable** in term of **Lyapunov Stability Analysis**.

Moving to next step of LQR controller design, here we introduce the state feedback control schema for our system shown in (3.10)

LQR generates feedback gain
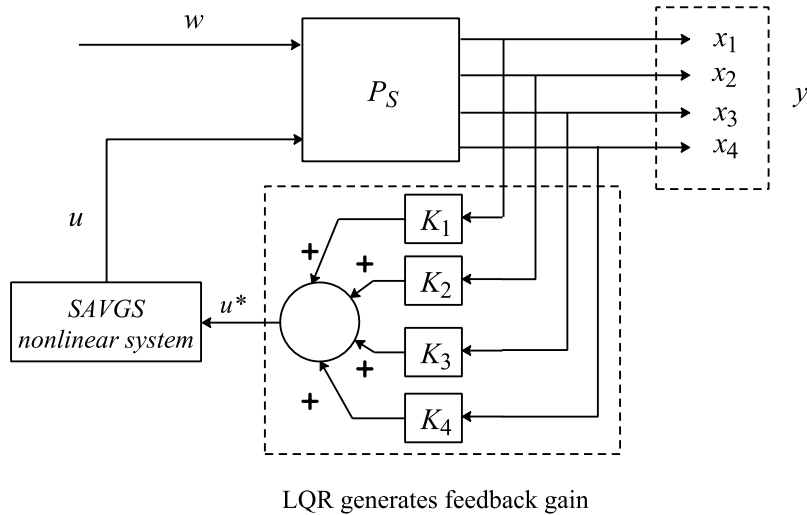
Figure 3.15 State feedback control

In this schema, $\boldsymbol{P_s}$ is realization plant that contained state equation and dynamics response of the system, $\boldsymbol{w(t)}$ is the input of system dynamics which is road disturbance in the vertical direction, $\boldsymbol{y(t)}$ is the output of the system which contained the dynamic response, $\boldsymbol{u(t)}$ is control input to the system which provided speed and position of single-link. $\boldsymbol{K}$ is generated by LQR controller bloc. In this work we seek somewhat value of $\boldsymbol{u(t)}$, which minimize the dynamics response under road disturbances, as a control input providing the optimal state trajectory will be exhibited "**good**".

46

The closed-loop state equation incorporated feedback gain of the system dynamic becomes

$$\dot{x}_p(\text{t}) = (A_p - B_u K)x_p(t)$$

$$y(t) = C_p x_p(t)$$

(3.47)

As we distinguish from Figure 3.15, $u(t)$ given by algebraic scalar product between state vector $x_p(t)$ and gain vector K. Therefore, K is a dominant parameter given by **LQR** design. The controller is designed for the fourth-order system (3.47) using linear quadratic regulator (LQR) design techniques. Hence, it is assumed that all states can be measured. The resulting system performance can therefore be regarded as an upper bound on what is achievable in practice. Frequently used measurement signals in production vehicles are the vertical acceleration of the chassis mass x_3, the suspension deflection x_1 and seldom the vertical acceleration of the wheel mass x_4 [12]. Especially the measurement of the tire deflection or the dynamic wheel load, respectively, can be complicated in reality. Although there exist tire deflection measurement concepts for test rigs or test-vehicles, an integration in production-vehicles fails so far due to costs and complexity of the sensors. However, as various approaches for observer design to estimate the vehicle states from measurement signals are described in [12], the assumptions above as well as angular position of the SL [13] can be dropped if an observer is used in the controller structure.

In regards to ride comfort, road holding and suspension deflection bound; the quadratic performance index (J); the input feedback ($u^*(t)$) (linear equivalent speed) commanded by controller; and the controller feedback gain vector (K) derived based on theories listed from (2.7), (2.8) and [21]. The quadratic performance index is

$$J = \lim_{t \to \infty} E[r_1 z_1^2 + r_2 z_2^2 + r_3 z_3^2]$$

(3.48)

where **E[.]** denoted as the expectation value consists of the three dominant performance indices ordered as: sprung mass acceleration, suspension deflection,

and tire deflection. The penalized factors r_1, r_2, and r_3 are varied to achieve the performance trade-off among ride comfort, suspension travel, and road holding.

We conclude that the steady-state linear quadratic regulator problem can be solved if the differential Riccati equation has a well-defined constant steady-state solution $\bar{P}$ that satisfies the **algebraic Riccati equation**. In this case, the optimal control feedback law (linear equivalent speed) commanded by controller is time-invariant, given by:

$$u^*(t) = -K^T x_p, \text{ with}$$
$$\tag{3.49}$$
$$K = R^{-1}B^T\bar{P}$$

Riccati equation

$$A^T\bar{P} + \bar{P}A - \bar{P}BR^{-1}\bar{P} + Q = 0 \tag{3.50}$$

$\boldsymbol{u}^*(\boldsymbol{t})$ defined in (3.49), which is input feedback of aforementioned state space equations, is not incorporated bandwidth limitation. u considered on bandwidth limitation is generated after u^* surpassed the bloc "***SAVGS nonlinear system***" in Figure 3.16). The schema of generating $\boldsymbol{u}(\boldsymbol{t})$ is shown in Figure 3.16.
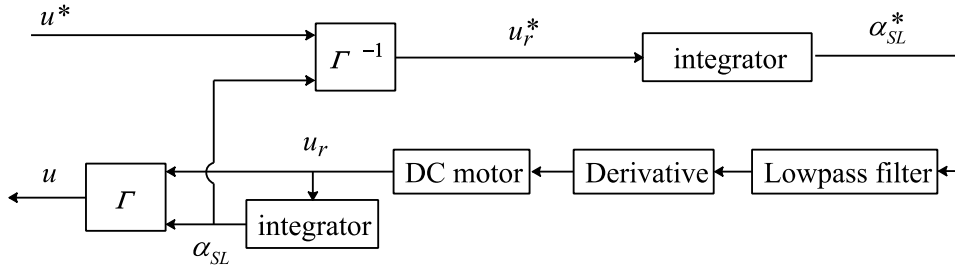
Figure 3.16 SAVGS nonlinear system bloc, $\boldsymbol{u_r}$ and $\boldsymbol{\alpha_{SL}}$ are the rotary actuator speed and that of single-link position, respectively. The asterisk (*) in superscript denoted as the commanded values of controller.

Considering the lowpass filter is described by

$$\ddot{\alpha}_{SL} + 2\zeta_f \omega_c \dot{\alpha}_{SL} + \omega_c^2 \alpha = \omega_c^2 \alpha_{SL}^* \tag{3.51}$$

where the cut-off frequency ω_c incorporates the bandwidth of the rotary actuator. Define $z_{f1} = \alpha_{SL}$ and $z_{f2} = \dot{\alpha}_{SL}$ as state variable for the low pass filter, the state space form of the low pass filter can be written as

$$\dot{z}_f = A_f z_f + B_f \alpha_{SL}^*$$

$$\alpha_{SL} = C_f z_f + D_f \alpha_{SL}^* \tag{3.52}$$

where $A_f = \begin{bmatrix} 0 & 1 \\ -\omega_c^2 & -2\zeta_f \omega_c \end{bmatrix}$, $B_f = \begin{bmatrix} 0 \\ \omega_c^2 \end{bmatrix}$, $C_f = [1 \quad 0]$ and $D_f = [0]$

1. *MATLAB for optimal control*

The following MATLAB functions are useful for design of state feedback control laws that solve the linear quadratic regulator problem:

$K = lqr(A_p, B_u, Q, R)$ directly calculates the optimal linear quadratic regulator gain matrix K, given the system dynamics matrix A_p, the input matrix B_u, and the weighting matrices Q and R.

3.2.3 LQR for DC Motor

In this section, the model DC motor incorporated with its controller is introduced. Some relation properties of DC plant discussed in this section is based on the reference in [22]. A common actuator in control systems is the DC motor. It directly provides rotary motion and, coupled with wheels or drums and cables, can provide translational motion. The electric equivalent circuit of the armature and the free-body diagram of the rotor are shown in Figure 3.17.
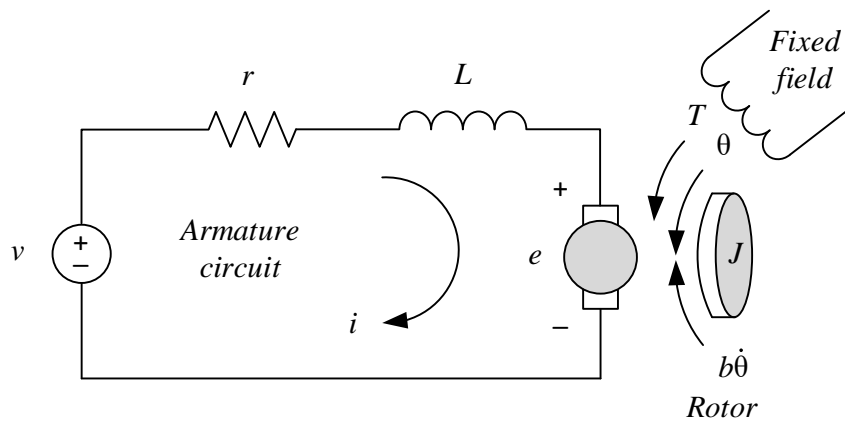
Figure 3.17 Schematic diagram of DC motor [22]

Taking that the input of the system is the voltage source (V) applied to the motor's armature, while the output is the rotational speed of the shaft $\dot{\theta}$. The rotor and shaft are assumed to be rigid. We further assume a viscous friction model, that is, the friction torque is proportional to shaft angular velocity. The physical parameters for DC motor used in our model is **FAULHABER 26572657W012CXR** with its parameters listed in Table 3.2:

Table 3.2 DC motor parameters [23]

Parameter	Symbol	Value	Unit
Moment of inertia of the rotor	J	1.7×10^{-6}	kg.m^2
Motor viscous friction constant	b	2×10^{-3}	N.m.s
Electromotive force constant	k_e	1.214×10^{-1}	V/rad/sec
Motor torque constant	k_t	1.933×10^{-2}	N.m/Amp
Electric resistance	r	7.2×10^{-1}	Ohm
Electric inductance	L	9×10^{-5}	H

3.2.3.1 System equations

In general, the torque generated by a DC motor is proportional to the armature current and the strength of the magnetic field. In this model we assumed that the magnetic field is constant and, therefore, that the motor torque is

50

proportional to only the armature current i by a constant factor k_t as shown in the equation below. This is referred to as an armature-controlled motor.

$$T = k_t i \tag{3.53}$$

The back emf, e, is proportional to the angular velocity of the shaft by a constant factor k_e

$$e = k_e \dot{\theta} \tag{3.54}$$

From Figure 3.17 above, we can derive the following governing equations based on **Newton's 2nd law** and **Kirchhoff's voltage law**.

$$J\ddot{\theta} = k_t i - b\dot{\theta} \tag{3.55}$$

$$L\frac{di}{dt} = V - k_e \dot{\theta} - ri \tag{3.56}$$

3.2.3.2 Controller design

In our suspension control system, the control output to single-link is position or speed of single-link motor so that the design control of DC motor is supposed to be angle speed control ($\dot{\theta} = \dot{\alpha}_{SL}$). In SI units, the motor torque and back emf constants are equal [22], that is, $k_t = k_e$; therefore, we will use k_e to represent both the motor torque constant and the back emf constant.

Define the following state variables, $x_{dc1} = i$, $x_{dc2} = \dot{\theta}$, and $u_{dc} = V$. Combined (3.55) and (3.56) of which are state space equation for DC motor derived as:

$$\dot{x}_{dc} = A_{dc}x_{dc} + B_{dc}u_{dc}$$
$$\tag{3.57}$$
$$y_{dc} = C_{dc}x_{dc}$$

where $x_{dc} = [x_{dc1} \ x_{dc2}]^T$ is the DC motor state at time t,

$$A_{dc} = \begin{bmatrix} -\dfrac{r}{L} & -\dfrac{k_e}{L} \\ \dfrac{k_e}{J} & -\dfrac{b}{J} \end{bmatrix}$$

$$B_{dc} = \begin{bmatrix} \dfrac{1}{L} \\ 0 \end{bmatrix} \tag{3.58}$$

$$C_{dc} = \begin{bmatrix} 0 & 0 \\ 0 & 1 \end{bmatrix}$$

3.2.3.3 Dynamic response of unit step input

The purpose of DC controlled is rotational speed $\dot\theta$ with steady state error improvement via iterative state-weighted. Suppose that, we want to command $\dot\theta$ to 1 rad/s started from zero initial state. The feedback gain obtained from LQR is $K_{dc} = [2.7556 \quad 8.2134 \times 10^{-1}]$.
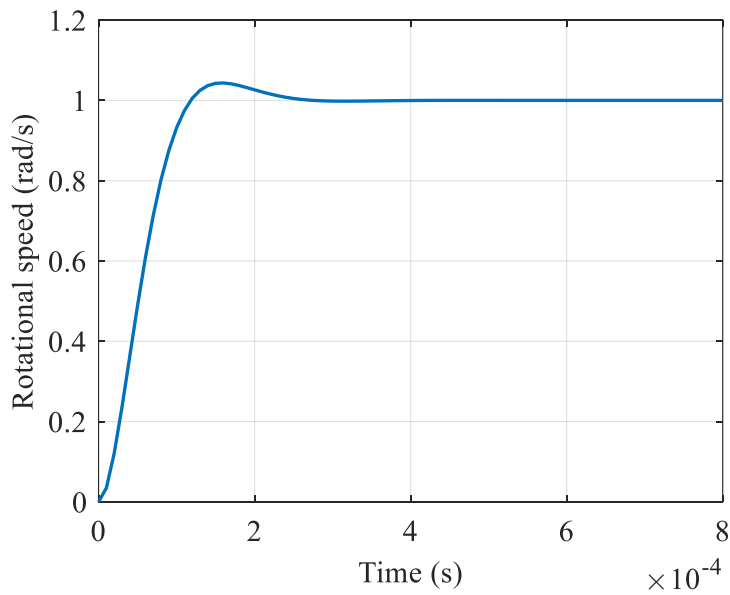

Figure 3.18 Unit step response of DC motor

The closed-loop state equation can be written as:

$$\dot{x}_{dc} = (A_{dc} - B_{dc}K_{dc})x_{dc} + B_{dc}u_{dc}$$

$$y_{dc} = C_{dc}x_{dc}$$

(3.59)

Steady-state error can be analyzed via **Final Value Theorem** in [24], then we have:

$$\lim_{s \to 0} sE(s) = \lim_{s \to 0} sR(s)[1 - \mathbf{C_{cd}}(s\mathbf{I} - \mathbf{A_{cl}})^{-1}\mathbf{B_{dc}}]$$

(3.60)

where $\mathbf{A_{cl}} = A_{dc} - B_{dc}K_{dc}$, substituting values of A_{dc}, B_{dc}, and K_{dc} into (3.59), then into (3.60), we obtain

$$e(\infty) = \lim_{s \to 0} \left(\frac{2.294 \times 10^{33}}{9 \times (3.21 \times 10^{23}s^2 + 1.28 \times 10^{28}s + 2.549 \times 10^{32})} - 1 \right)$$

(3.61)

Hence,

$$e(\infty) = 1.975 \times 10^{-5}$$

Transfer function of closed-loop can be derived as

$$T(s) = \mathbf{C_{cd}}(s\mathbf{I} - \mathbf{A_{cl}})^{-1}\mathbf{B_{dc}}$$

$$T(s) = \frac{7.937 \times 10^8}{s^2 + 3.979 \times 10^4 s + 7.937 \times 10^8}$$

(3.62)

In [21], the standard second-order transfer function formulated as

$$H(s) = \frac{\omega_n^2}{s^2 + 2\xi\omega_n s + \omega_n^2}$$

(3.63)

Comparing (3.62) and (3.63), then we got, $\omega_n = \sqrt{7.937 \times 10^8} = 2.817 \times 10^4$, and $\xi = 7.062 \times 10^{-1}$.

Rise time t_r is defined as the elapsed time between when the response first reaches 10 percent to 90 percent of the steady-state value.

$$t_r \cong \frac{2.16\xi + 0.6}{\omega_n} = 7.54 \times 10^{-5} \text{ s}$$

Peak time t_p is the time at which the peak response value is reached

$$t_p = \frac{\pi}{\omega_n\sqrt{1 - \xi^2}} = 1.575 \times 10^{-4} \text{ s}$$

Percent overshoot PO characterizes the relationship between the peak value and steady-state value

$$PO = 100e^{-\frac{\xi\pi}{\sqrt{1-\xi^2}}} = 4.35\%$$

Settling time t_ss is defined to be the time at which the response enters and remains within a ±2 percent band about the steady-state value

$$t_s \cong \frac{4}{\xi\omega_n} = 2.01 \times 10^{-4} \text{ s}$$

3.3 Model Road Disturbance

3.3.1 Highway Road Profile

The road disturbance model is commonly used of random road profile, which is approximated by a stationary random process. A frequent used approximation of a road displacement is given as power spectral density (PSD) [5], [12], [25]:

$$S_{z_r} = \frac{\varepsilon_f}{v}\left(\frac{2\pi f}{v}\right)^n \qquad\qquad (3.64)$$

where ε_f is a constant roughness factor, f is the excitation frequency and v is the constant vehicle velocity. The spatial spectral density of a measurement highway road profile is chosen in [12] as a reference for equation (3.64). It is reported that the closest approximation value is widely accepted when $n = -2$ coincides with

the commonly used assumption of **white noise**. The PSD ground velocity is given by [12]:

$$S_{\dot{z}_r} = (2\pi f)^2 . S_{z_r}(f) = \varepsilon_f v \tag{3.65}$$

depending on road conditions and driving speed.

3.3.1.1 Performance evaluation criterion

The performance analysis of dynamic suspension system; which is sprung mass acceleration, suspension travel, and tire deformation. These outputs are the root-mean-square (rms) of which normalized values used in [12] ensures compatibility of the systems performing independent of road disturbance. The normalization is obtained by dividing the rms values by the square root of the white noise intensity given as in [12]:

$$V_{\dot{z}_r} = 2\pi \varepsilon_f v \tag{3.66}$$

To evaluate the performance, the formula defined as

$$PC = \left(1 - \frac{N_y}{N_{ref,y}}\right) \times 100 \tag{3.67}$$

where PC is the performance-compared, N_y is the normalized rms performance to be evaluated and $N_{ref,y}$ is the normalized rms performance of a reference system (e.g., the normalized rms tire deflection of passive system $N_{p,y3}$).

3.3.2 Single Smooth Bump Road Profile

Another road disturbance model commonly used in simulation and test rig is bump road profile. In our study, a cam-driven excitation device is designed to convert the rotary motion of a cam into vertical translation motion of tire. As shown in Figure 3.29, an eccentric cylinder in Appendix 2 Fig. 25, which is driven by a rotary actuator, acts as the cam.

In [2], the road height (z_r) variation against the cam angle derived through the geometric relationship between the cam and the roller follower (tire) is defined as

$$z_r = h_{CAM}(1 - \cos \Delta\theta_{CAM}) \tag{3.68}$$

where h_{CAM} is the eccentricity between the cam's tip and center of rotation, and $\Delta\theta_{CAM}$ is cam rotating angle respective to its zero state of which it was shown in Figure 3.29. Based on our designed cam, $h_{CAM} = 5$ mm. However, a bump road profile representation used (3.68) for our system somehow exists bandwidth offset from measurement. Consequently, h_{CAM} in (3.68) is summed by any constant value which is iteratively selected to get the appropriate road representation. $\Delta\theta_{CAM}$ initialized at **0 rad** for our designed cam will cause high bump height so that we decide to initialize our cam angle at $\frac{\pi}{2}$ **rad**. A bump road representation for our system is rewritten as:

$$z_r = -(h_{CAM} + h_e) \cos\left(\theta_{CAM} + \frac{\pi}{2}\right) \tag{3.69}$$

where $h_e = 0.15$ mm is the existence bandwidth offset profile. θ_{CAM} with frequency of $f_r = 1.984$ Hz is sinusoidal signal representing forward and backward cam rotation directions is defined as

$$\begin{cases} \theta_{CAM} = 0.3708[1 - \cos(2\pi f_r t)] \Rightarrow 6T \leq t \leq 7T \\ \qquad\qquad T = \dfrac{1}{f_r} \\ \qquad 0, \Rightarrow \text{otherwise} \end{cases} \tag{3.70}$$

The simulation emulates the case of a car traveling at a speed of 1 km/h and running over a smoothed bump height 3.47 mm with 14 cm width, respectively. Figure 3.19 illustrated the bump road profile gotten from sinusoidal function in (3.69) and from measurement in Sim mechanic.
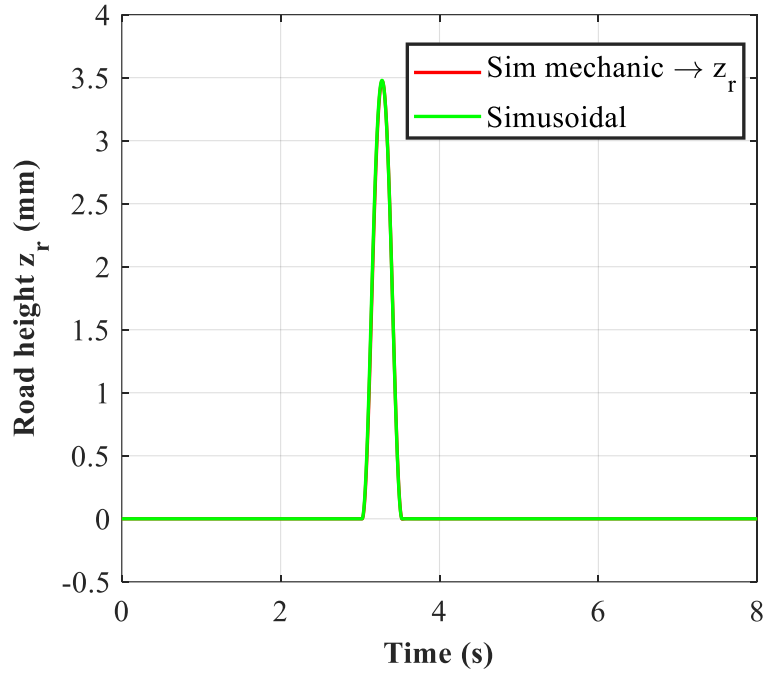
Figure 3.19 Bump road profile generated by the eccentric cam and the approximated sinusoidal function for the generation of target road profiles

Based bump road profile presented in (3.70), the road velocity disturbance can be represented by the derivative z_r in (3.70) respected with time so that the vertical road velocity is defined as

$$\dot{z}_r = (h_{CAM} + h_e) \times \frac{d\theta_{CAM}}{dt} \times \sin\left(\theta_{CAM} + \frac{\pi}{2}\right) \tag{3.71}$$

Figure 3.20 illustrates the signal of bump road velocity gotten from the road profile in Figure 3.19.
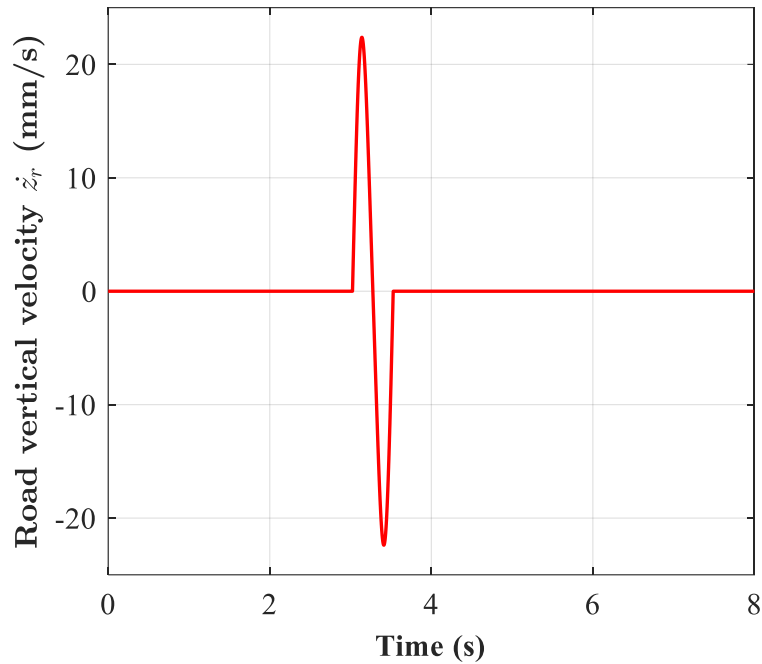
Figure 3.20 Bump vertical road velocity signal

3.4 Simscape Multibody

Simscape Multibody provides a multibody simulation environment for 3D mechanical systems, such as robots, vehicle suspensions, construction equipment, and aircraft landing gear [26]. We can model multibody systems using blocks representing bodies, joints, constraints, force elements, and sensors. **Simscape Multibody** formulates and solves the equations of motion for the complete mechanical system. We can import complete **CAD** assemblies, including all masses, inertias, joints, constraints, and 3D geometry, into our model. An automatically generated 3D animation lets you visualize the system dynamics.

Simscape Multibody helps us develop control systems and test system-level performance. We can parameterize our models using MATLAB variables and expressions, and design control systems for your multibody system in Simulink. We can integrate hydraulic, electrical, pneumatic, and other physical systems into our model using components from the Simscape family of products.

In our work, we used 3D CAD assemblies built in **Solidworks**. The step of works to achieve the active suspension system performances are shown in
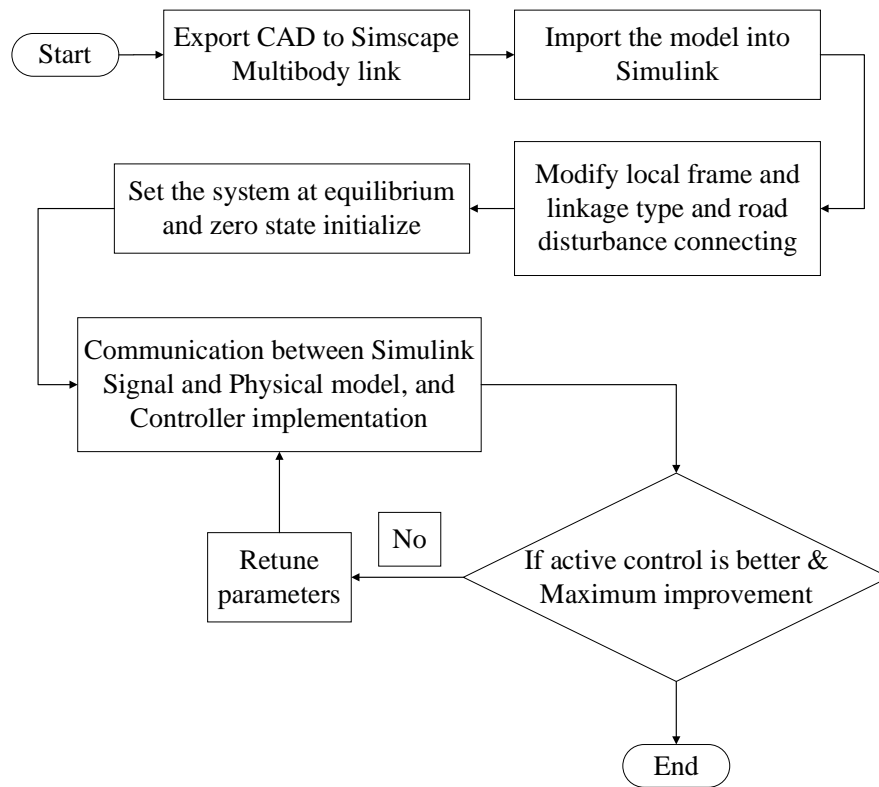
Figure 3.21 Simscape multibody built and controller implementation

As the first step of quarte double wishbone built in **Sim Mechanic**, we used the existing full assembly parts in **Solidworks** and export as **Simscape Multibody Link**. After that, the exported file with extension **.xml** is need to be imported into MATLAB Simulink.

Modify local frame and linkage type: Using Solidworks assembly parts and exporting it are very useful tool multibody system built in **Sim mechanic**. It provided the same geometry as in CAD. Moreover, it provided the coordinate transformation of each body's global frame which is used for localizing the linkage joint. The joint type will provide adapting to what has been characterized in CAD. However, the local frame and linkage type still not provided correctly, so that we need to modify them again. The joints used in our system presented with several types are shown Figure 3.22.
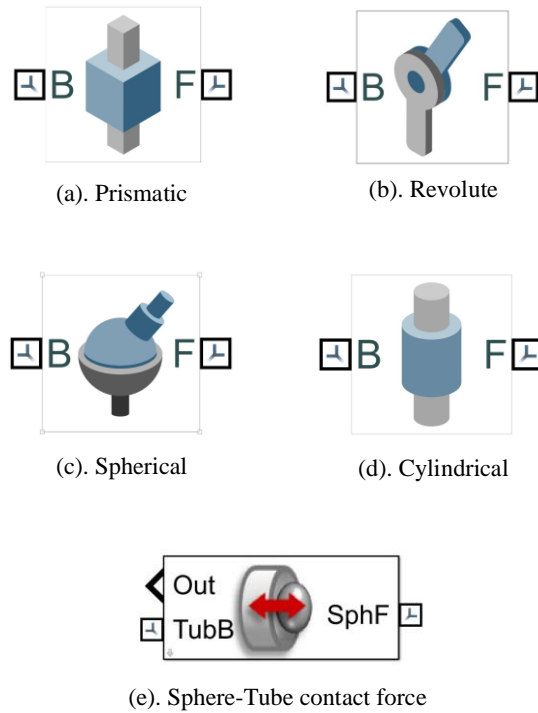
(a). Prismatic   (b). Revolute

(c). Spherical   (d). Cylindrical

(e). Sphere-Tube contact force

Figure 3.22 Joint linkage used

> (a) Prismatic joint admits only one translational degree of freedom used at:

  ❖ Joint between linear bearing SCS8UU and rod as a supporting frame

  ❖ Suspension spring-damper component: the internal mechanic also be filled such stiffness and damper coefficients.

  ❖ Joint between knuckle wheel hub and tire: we used it to represent the internal properties tire which are stiffness and damper coefficients of tire.

> (b) Revolute joint admits only one rotational degree of freedom used at:

  ❖ Joint between lower arm and chassis

  ❖ Joint between upper arm and chassis

  ❖ Joint between upper arm and knuckle wheel hub

  ❖ Joint between upper knuckle wheel hub and tire: used it to allow rotational motion of tire

❖ Joint between rotor and main body of servo motor: used for representing the motion of motor as well as allowed for external input as commanded by state feedback gain.

❖ Join between single-link and suspension end-strut

➢ (c) Spherical joint admits three degree of freedom of rotations

❖ Joint between suspension lower strut and sphere part which connects to the lower arm

➢ (d) Cylindrical joint admits one translational and one rotational degree of freedom: The reason why we don't use all revolute joint without cylindrical joint is that it would be exist in somewhere blocs with the alignment violation during modeling the system. So that some place used cylindrical joint instead of revolute joint to allow any translational displacement.

❖ Joint between lower arm and knuckle wheel hub

❖ Joint between sphere part at lower suspension strut and lower arm

➢ (e) Sphere-tube contact force is used to create the contact point between road disturbance profile (cam rotation) and tire which represent tube and sphere parameters, respectively. This library is an additional toolbox in "**Simscape Multibody Contact Forces Library**" and can be download in [27]

The fourth step of **Sim mechanic** built is setting the system at static equilibrium and zero state initialize. To do this, we need to know the information of state variables by using **Transform Sensor** bloc which can measure the position, velocity and acceleration of any point connected with Transform Sensor. Moreover, we can measure the aforementioned state by using **Sensing** in properties set of **joints** if the point we want to measure stayed in that joints. Consequently, we run the model for any suitable time range assuring the system reach static state. Taking these values of state variables, which can be displayed by addition bloc "**Physical to Simulink signals**" shown in Figure 3.23, and set as priority to **initial state** of related joints. Zero initialize state especially x_1 and x_2 can be set by subtracting any constant values from the measurement values gotten at static state.

(a). Physical to Simulink
signals

(b). Simulink to Physical
signals
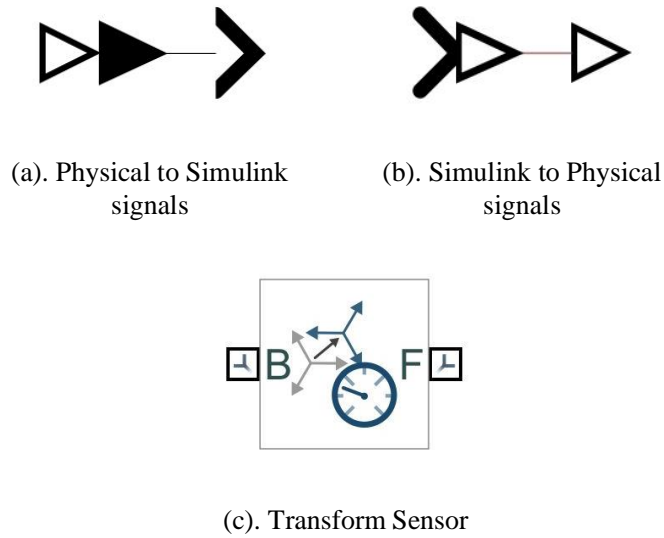

(c). Transform Sensor

Figure 3.23 Sim mechanic utility

The fifth step is **Communication between Simulink signal and Physical model, and Controller implementation**, this step would be extended as shown in
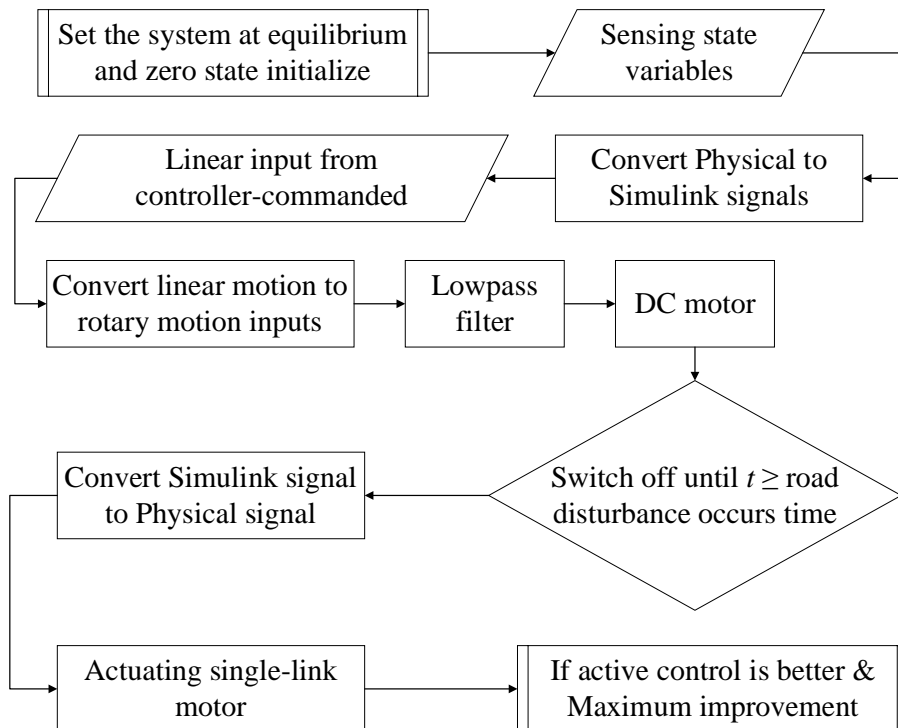

Figure 3.24 Extended bloc "Communication between Simulink Signal and Physical model, and Controller implementation" in Figure 3.21

3.5 Prototype Model of Double Wishbone Quarter-Car

The full quarter-car model in this work is built based on the **Solidworks** program. These models not only prefer enabling for **Sim mechanic** simulation but also for the hard-printed parts of real experiment. Due to the simultaneous desired, some part which can be merged are separated to ensure the **3D printer** can print those.

3.5.1 Three Dimensions Views

The overall full assembly views of quarter-car prototype model with double wishbone arrangement are shown from Figure 3.25 to Figure 3.31. Each Figure is shown with each respective side views.
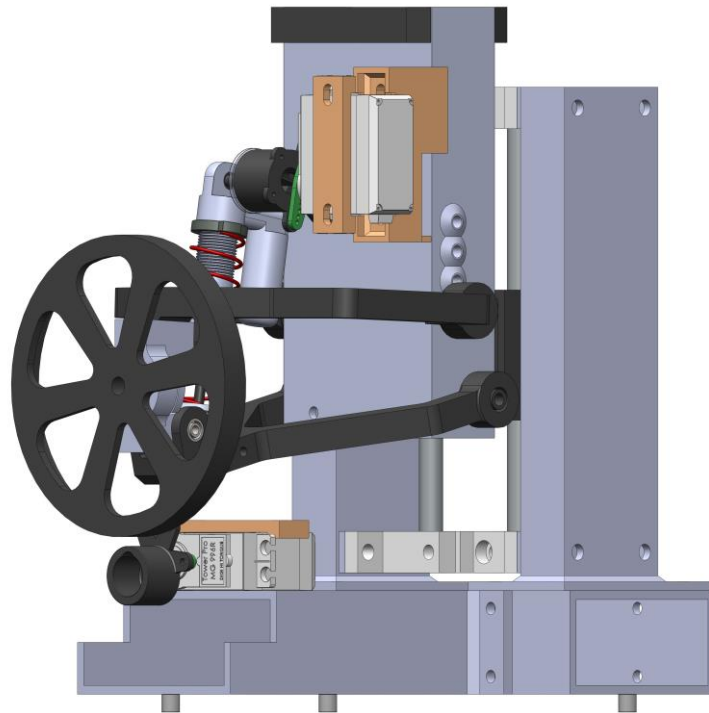
Figure 3.25 Quarter-car prototype at the front-right side view
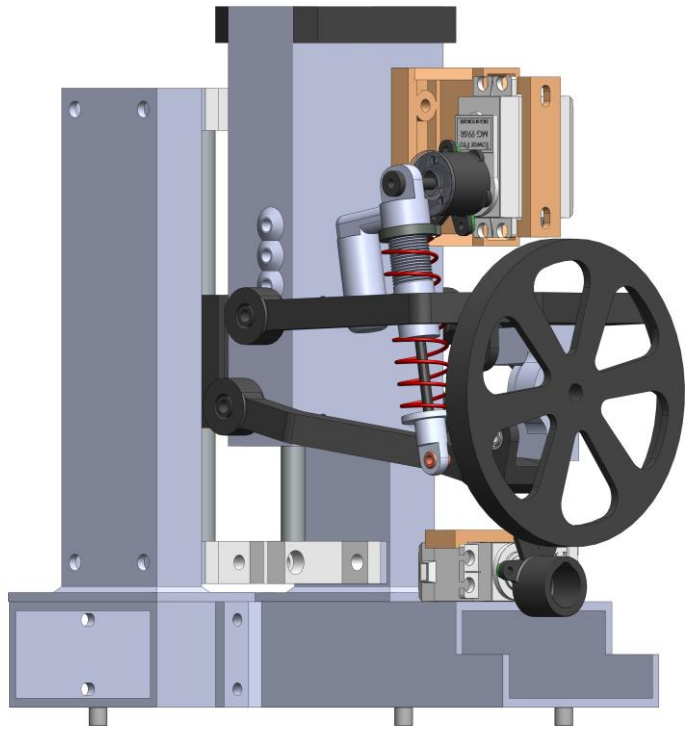
Figure 3.26 Quarter-car prototype at the front-left side view
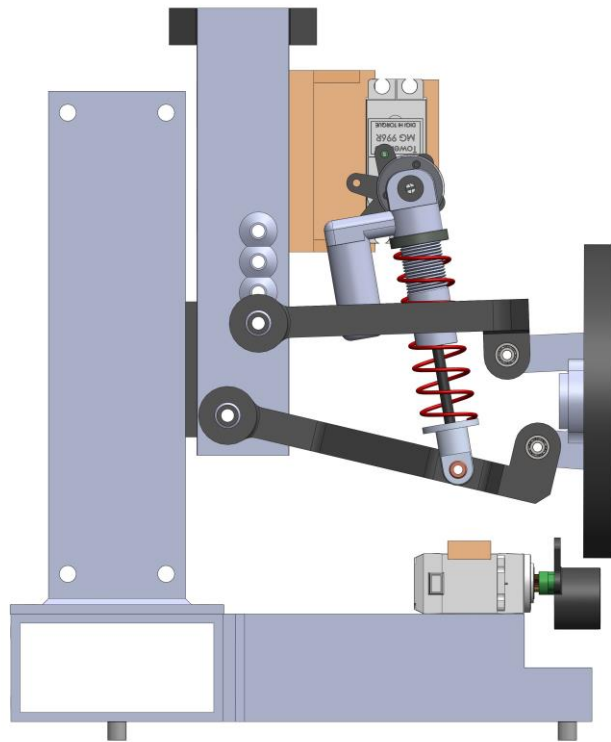
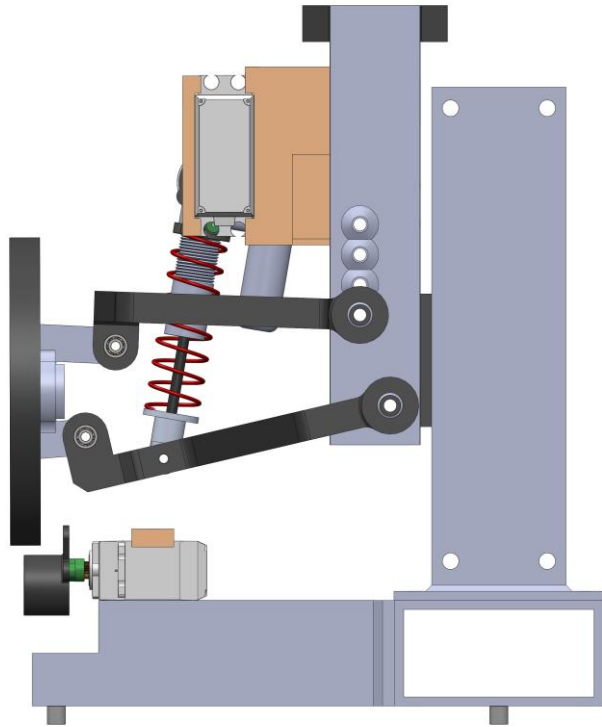Figure 3.27 Quarter-car prototype at left side view
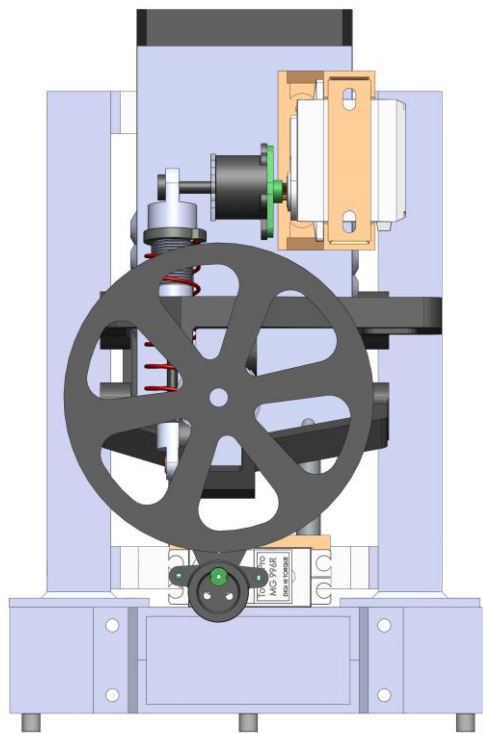
Figure 3.28 Quarter-car prototype at right side view

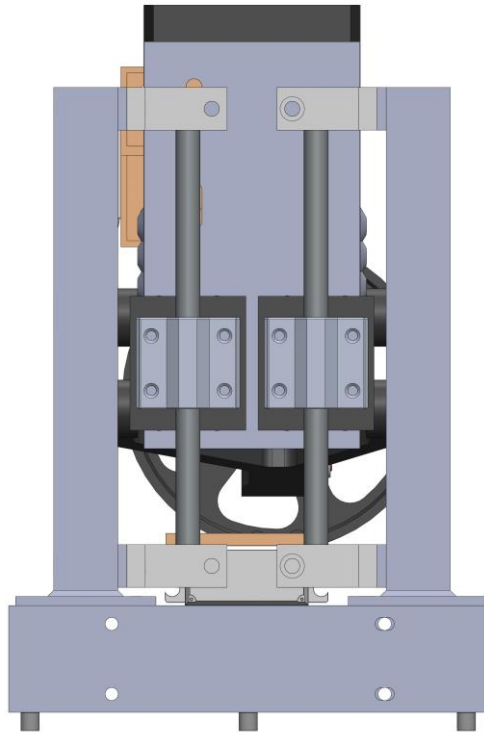Figure 3.29 Quarter-car prototype at front view

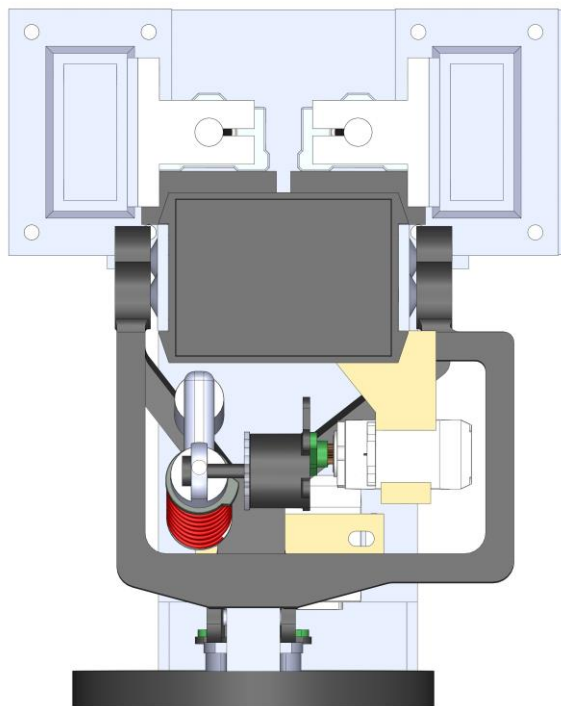Figure 3.30 Quarter-car prototype at the side behind

Figure 3.31 Quarter-car prototype at top view

3.5.2 The Main Components in 2-D

In this section, all parts of quarter-car prototype are listed. Those parts somewhat included the printable parts and available-marketed parts. It is separated into two subsections which are supported bloc and main components.

3.5.2.1 Main components

The full assembly for main component of quarter-car prototype configuration 1, which composes sprung mass and unsprung mass blocs, is shown in Figure 3.32. Numerous parts with different role described as the following:

➢ Chassis part

➢ Lower arm and Upper arm: used to arrange and allow relative motion of the wheel assembly to the chassis. The joint connected these arms to the chassis are revolute joint represented by rotary bearing. Two bearing used to connect each arm to the chassis.

➢ Tire: connected to the knuckle wheel hub by rotary bearing.

➢ Spring-damper unit: connected to lower arm by spherical joint and to the single-ink by rotary bearing. Two rotary bearings used to reduce the error of transmission of radial load created by spring-damper unit.

➢ Knuckle wheel hub part: used to connect the wheel to the arm and allow the wheel motion to roll axis.

➢ Knuckle washer part: used to fixed the rotary bearing, which allow the rotation of wheel, in bearing house.

➢ Bolt spacer part: used to fix the bearing core to the chassis.

➢ Joint baque: used to attached the suspension end-strut to the single-link.

➢ High-end spacer: used to reduce the clearance between suspension end-strut and joint baque.

➢ Single-link part

➢ Single-washer part: attached to single-link and used to fix the rotary bearing staying firmly in bearing house.

➢ Servo motor MG 996R: used to actuate the rotation of single-link

- Single-link motor supporter: used to support and offset the motor to the proper location.
- Servo fixer part: used to fix servo motor firmly.
- Linear bearing SCS8UU: used to align the chassis bloc stay in purely vertical motion.
- Linear bearing supporter: in this quarter design, it is required to offset the linear bearing from the chassis
- Load supporter: just additional case, if the experimentation aims to study at different load level, metal plates can be put in it.
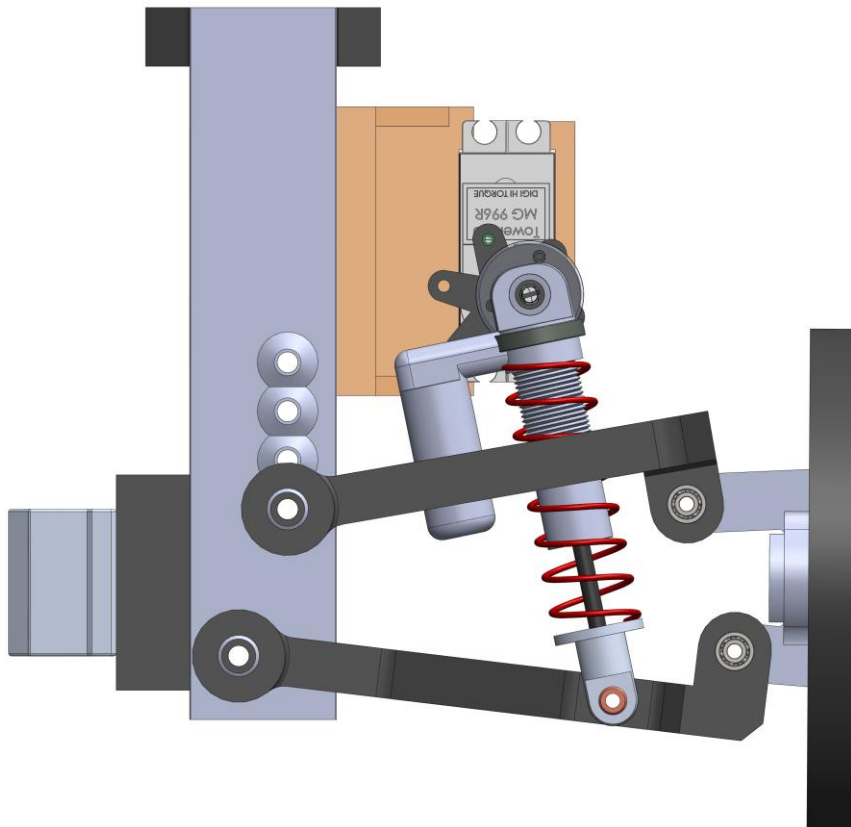

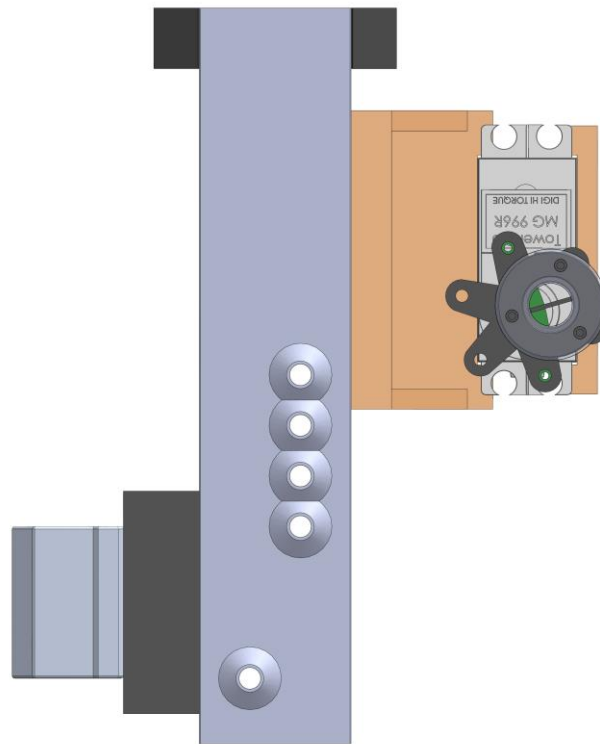Figure 3.32 Full assembly of main components

Figure 3.33 Sprung mass assembly

Figure 3.34 Unsprung mass assembly

All main component parts incorporated with dimensioning are appeared orderly as stated on the above description for configuration 1 and configuration 2 in **Appendix 1**.

3.5.2.2 Supporter components

The full assembly for supporter component of quarter-car prototype is shown in Figure 3.35.
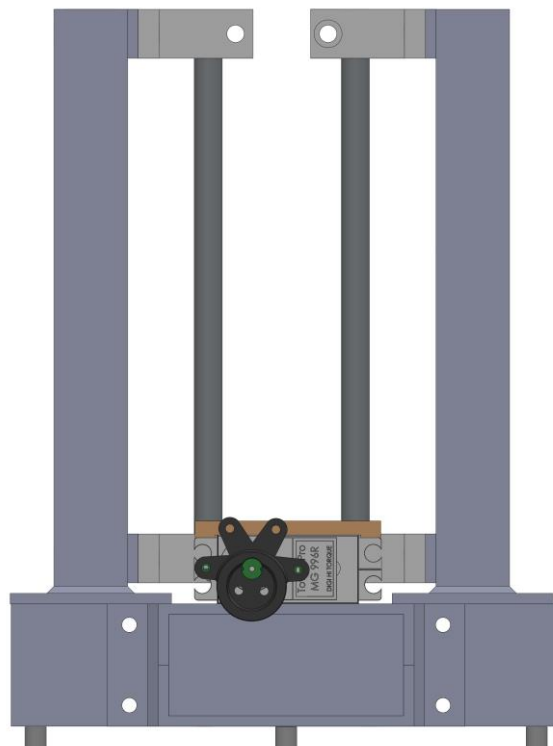

Figure 3.35 Full assembly of quarter-car supporter

All parts with different roles descripted as the following are placed in order in **Appendix 2**:

> ➢ Bottom support: it composes two parts, bottom support 1 and bottom support 2. They are used for standing the whole system as well as support for rails and excitation motor.
>
> ➢ Ground parts: there are three of it attached to bottom part and used to maintain the supporter bloc to be at static equilibrium.

- ➢ Servo motor MG996R: the cam is connected to excite as the road disturbance.
- ➢ Servo fixer part
- ➢ Rail supporter: it supports the rod as a guidance of sprung mass movement.
- ➢ SK8 rod housing: two in each rod
- ➢ Rail washer: used to offset SK8
- ➢ Rod: guidance of linear bearing

This page is blank

CHAPTER 4

RESULTS AND DISCUSSIONS

4.1 Simulink

4.1.1 Simulink Built

The simulation of linear equivalent quarter-car with subsequent blocs is shown in Figure 4.1. The conversion linear (rotary) actuator speed to rotary's (linear's) can be achieved by using Γ correlation discussed in Eqs. (3.27) and (3.28).
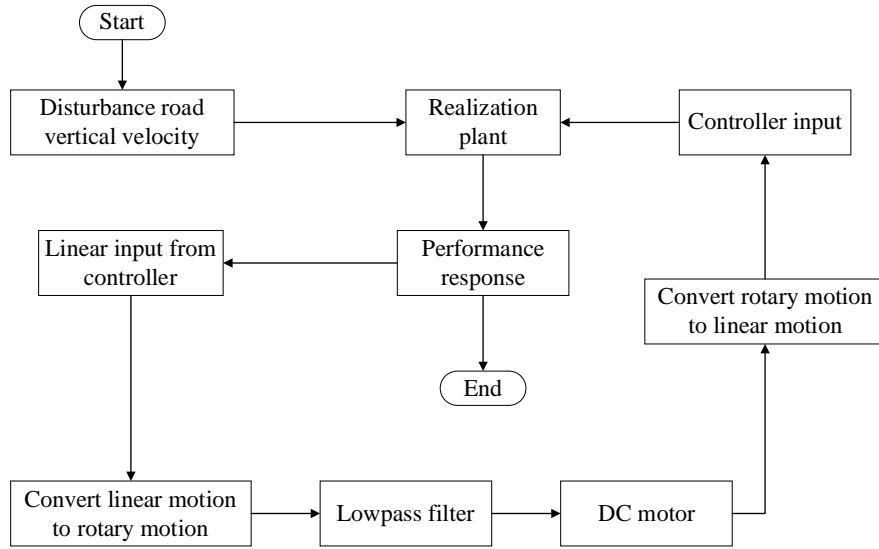
Figure 4.1 Simulation of linear equivalent model

4.1.2 Influence of Bandwidth

4.1.2.1 Highway road profile

To study the influence of bandwidth, firstly we choose $f_c = \frac{\omega_c}{2\pi} = 1$ Hz at which the controller weights are iteratively sought for the minimum sprung mass acceleration. After that, the optimal weighting at those frequent is applied to the SAVGS system in order to figure out the influences of varied bandwidth frequency to suspension performance. The actuator bandwidth f_c is varied from $0.1-5$ Hz.

For the disturbance in (3.65), the weighted controller seeking for the minimum vertical sprung mass acceleration under highway road disturbance at low pass frequency 1 Hz are likely located at; $r_1 = 8.4 \times 10^{25}$ and $r_2 = 8 \times 10^{28}$, and

$r_1 = 8.4 \times 10^{25}$ and $r_2 = 10^{28}$ for configuration 1 SL cases 1 and 2, respectively. For configuration 2, the optimal weight at those frequency are; $r_1 = 2 \times 10^{25}$ and $r_2 = 4 \times 10^{27}$, and $r_1 = 10^{20}$ and $r_2 = 10^{22}$ for SL cases 1 and 2, respectively.

These weighting values are used for the respective configuration to study the influence of bandwidth frequency in which Figure 4.2 illustrates.
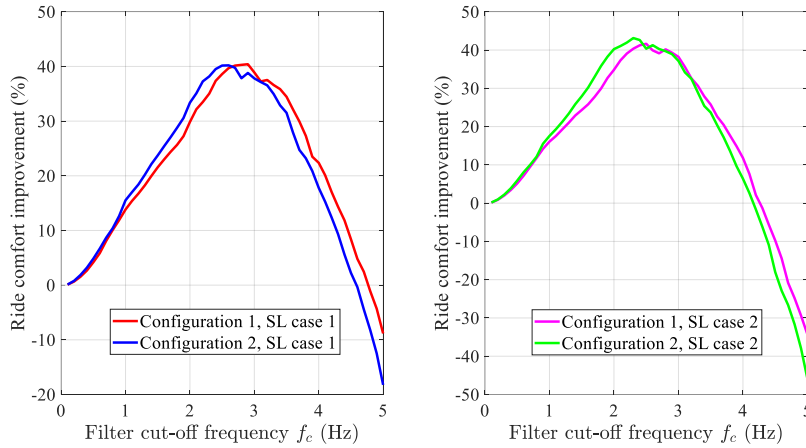

Figure 4.2 Ride comfort depending f_c under highway road profile: (a) Single-link rotation range case 1, (b) Single-link rotation range case 2.

Observing on Figure 4.2, the ride comfort improvements depending bandwidth frequency under a highway road likely have higher values at $f_c = 2.9$ Hz; 2.6 Hz; 2.6 Hz; and 2.3 Hz for suspension configuration 1 SL case 1, configuration 1 SL case 2, configuration 2 SL case 1, and configuration 2 SL case 2, respectively. These low pass frequency values will be used for iteratively seeking the optimal performance of SAVGS in **Simulink**.

4.1.3 Linear Equivalent Simulation Results
4.1.3.1 Simulation under highway road representation
1. Plot results

In order to point out the effect of SAVGS retrofitted in passive system as well as to compare those of different linkage geometries; the weighted on sprung mass acceleration (r_1) is fixed at value of **1** and the others, r_2 and r_3, are varied in

wide range; as well as the performance results of each SAVGS configuration are incorporated with those of individually passive configuration.

Two cases of the SL rotation range are studied. The SL rotation are ranged from 20° to 160° and 0° to 180°, which respected to its minimal state, for case 1 and case 2, respectively. The assumption of operating condition in [12] has taken the value of $\varepsilon_f = 4.9 \times 10^{-6}$ m and vehicle speed $v = 25$ m/s, which corresponds to a medium quality road; and the simulation duration is conducted for 6 s. Figure 4.3 and Figure 4.4 illustrated the normalized rms sprung mass acceleration corresponding to the varied r_2 and r_3 as well, for case 1 and case 2, respectively.
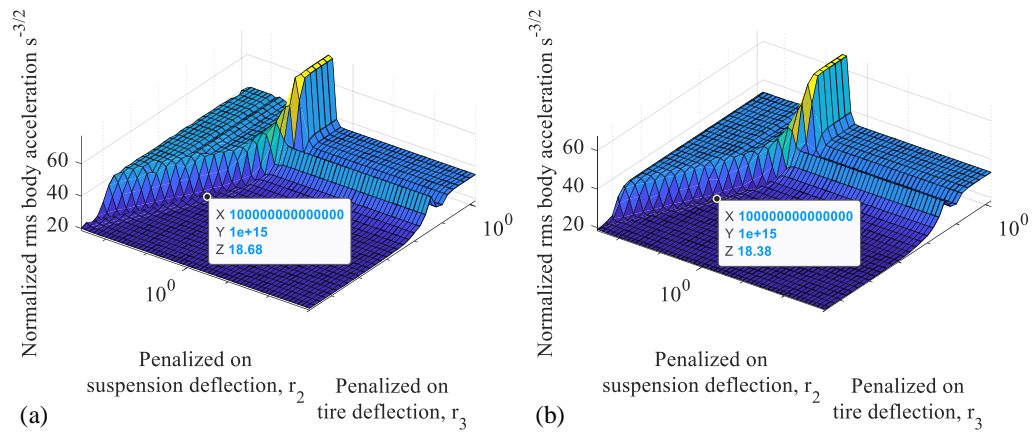

(a)　　　　　　　　　　　　　　　　　　　(b)

Figure 4.3 SL case 1: surface plot of the normalized rms body acceleration performance of SAVGS, (a) configuration 1 and (b) configuration 2
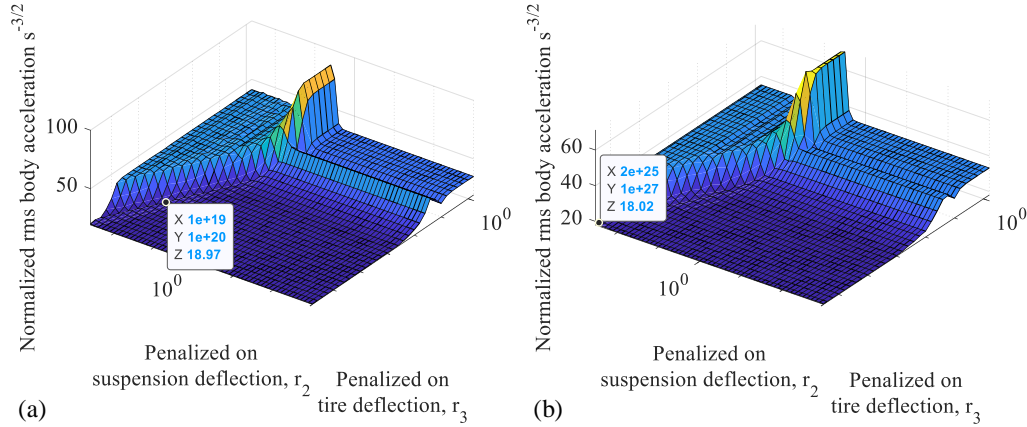
75

Figure 4.4 SL case 2: surface plot of the normalized rms body acceleration performance of SAVGS, (a) configuration 1 and (b) configuration 2

For configuration 1 (**C1**) in Figure 4.3a and Figure 4.4a, the penalized coefficients are ranging the values of r_2 from 10^{-30} to 8.4×10^{25} and r_3 from 10^{-1} to 8×10^{28}. Similarly, for configuration 2 (**C2**) in Figure 4.3b and Figure 4.4b, those of the values of r_2 from 10^{-30} to 2×10^{25} and r_3 from 10^{-1} to 4×10^{27}. The minimal normalized rms sprung mass accelerations in SL case 1; which are likely located at the trim state of $r_2 = 10^{14}$ and $r_3 = 10^{15}$ for **C1**, and $r_2 = 10^{14}$ and $r_3 = 10^{15}$ for **C2**; equal to 18.68 $s^{-\frac{3}{2}}$, and 18.38 $s^{-\frac{3}{2}}$, respectively.

Similarly, in case 2, those of values are likely located at the trim state of $r_2 = 10^{19}$ and $r_3 = 10^{20}$ for **C1**, and $r_2 = 2 \times 10^{25}$ and $r_3 = 10^{27}$ for **C2**; equal to 18.97 $s^{-\frac{3}{2}}$, and 18.02 $s^{-\frac{3}{2}}$, respectively. Remembered that those minimal states are not incorporated the constrained suspension deflection and tire deflection yet, the optimal states depended on constraints are considered next point.

2. *Optimization of controller weights incorporated with constraints*

The challenge is to minimize the normalized rms sprung mass accelerations of SAVGS ($N_{SAVGS,y1}$), which enhance the ride comfort, without violating their maximum allowable of normalized rms suspension deflection ($N_{y2,max}$) and that of tire deflection ($N_{y3,max}$), assuming that y is a normally distributed random variable assures that y remains within $\pm y_{max}$ for 99.7% of the time, if the rms-value is not exceeded. To achieve the optimal performance of each

configuration, the carpet plots introduced in [12] are used in an iterative optimization procedure with varied r_2 and r_3 while the maximum allowable suspension deflection $y2_{max}$ and tire deflection $y3_{max}$; $y2_{C1,max} = 18.1 \times 10^{-3}$ m and $y3_{C1,max} = 2.19 \times 10^{-3}$ m for C1, and $y2_{C2,max} = 18.67 \times 10^{-3}$ m and $y3_{C2,max} = 2.19 \times 10^{-3}$ m for C2, respectively. Applying (3.66), the $N_{y2,max}$ are $N_{y2_{C1},max} = 6.524 \times 10^{-1}$ s$^{\frac{1}{2}}$ and $N_{y2_{C2},max} = 6.729 \times 10^{-1}$ s$^{\frac{1}{2}}$, as well as the maximum allowable of normalized rms tire deflections are $N_{y3_{C1},max} = N_{y3_{C2},max} = 7.893 \times 10^{-2}$ s$^{\frac{1}{2}}$.
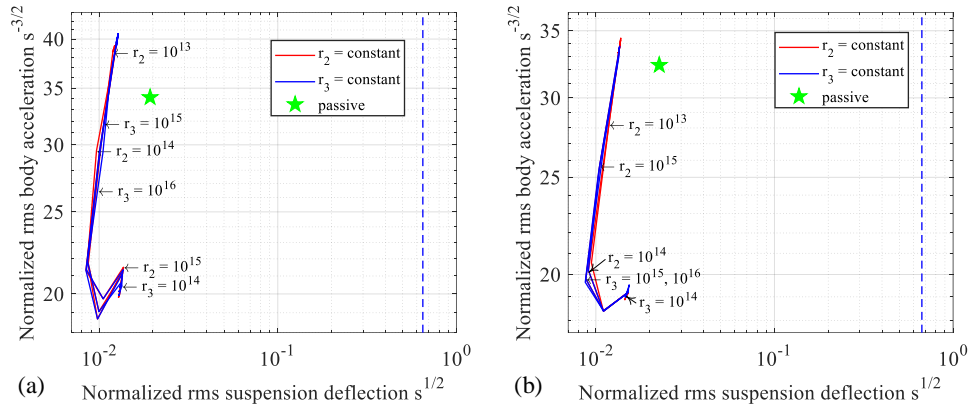

Figure 4.5 SL case 1: normalized rms suspension deflection corresponds to that of body acceleration, (a) configuration 1 and (b) configuration 2, (dashed line: maximum allowable value, star point: corresponded passive configuration)
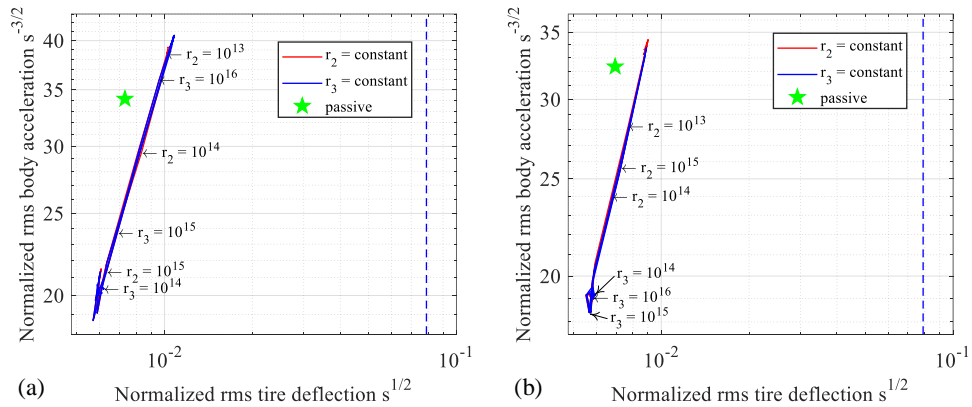

Figure 4.6 SL case 1: normalized rms tire deflection corresponds to that of body acceleration, (a) configuration 1 and (b) configuration 2, (dashed line: maximum allowable value, star point: corresponded passive configuration)
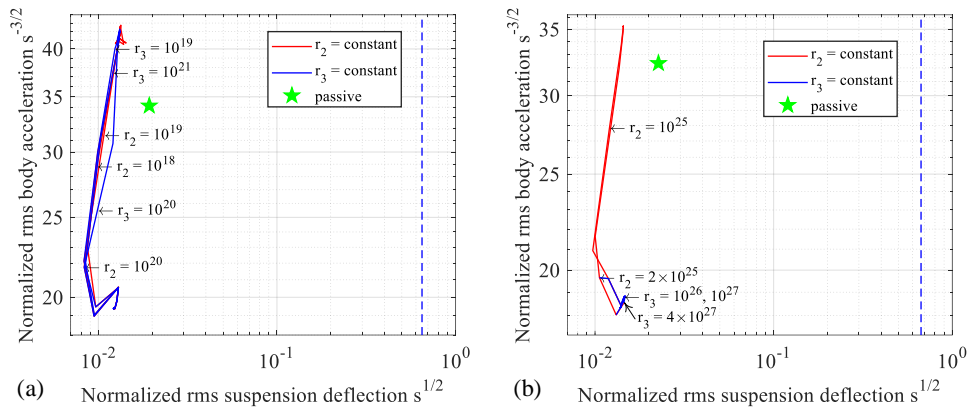
Figure 4.7 SL case 2: normalized rms suspension deflection corresponds to that of body acceleration, (a) configuration 1 and (b) configuration 2, (dashed line: maximum allowable value, star point: corresponded passive configuration)
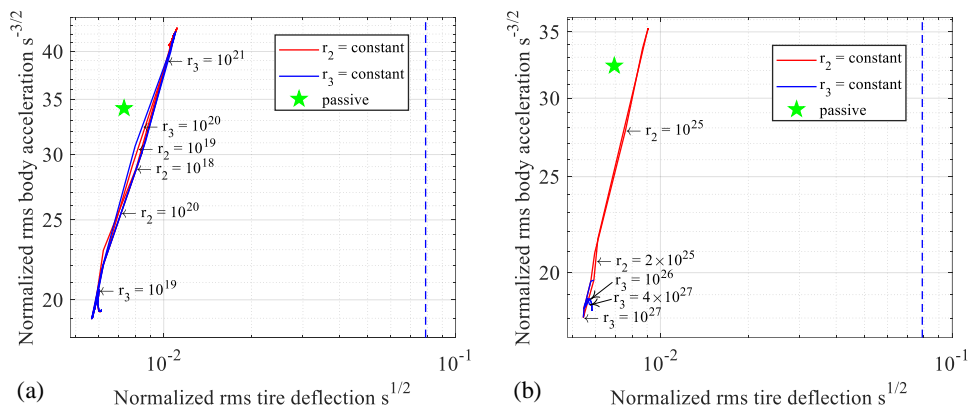

Figure 4.8 SL case 2: normalized rms tire deflection corresponds to that of body acceleration, (a) configuration 1 and (b) configuration 2, (dashed line: maximum allowable value, star point: corresponded passive configuration)

Figure 4.5 to Figure 4.8, which illustrate normalized rms suspension deflection as well as that of tire deflection corresponding to that of body acceleration, capture that the varied wide range of r_2 and r_3 does not violate on $N_{y2,max}$ and $N_{y3,max}$, as well as the normalized rms body acceleration cannot further improve beyond the r_2 and r_3 considered in Figure 4.3 due to the indefinite of state weighting matrices. Based on these figures, the performance optimization will be iteratively weighted at the nominal trim state discussed in "1. Surface plot".

78

Figure 4.9 to Figure 4.12 illustrate the simulation result of sprung mass acceleration, suspension deflection, tire deflection, and single-link position and road disturbance, respectively.
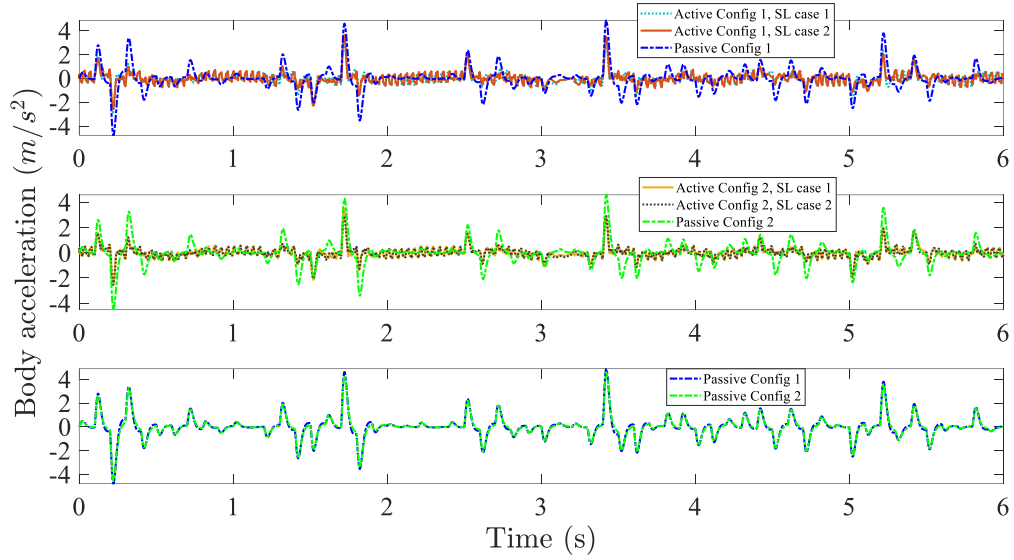

Figure 4.9 Simulation results of body acceleration under highway road
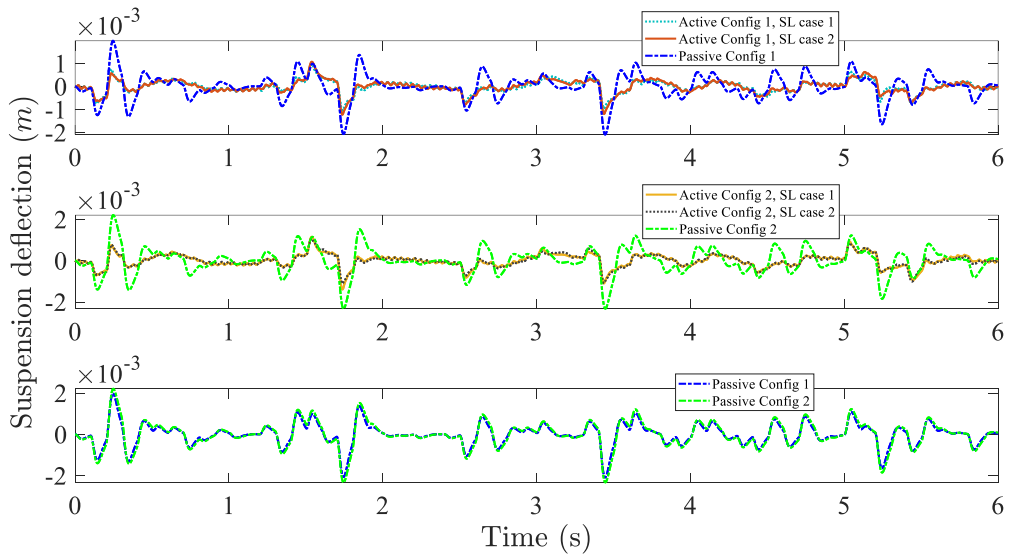

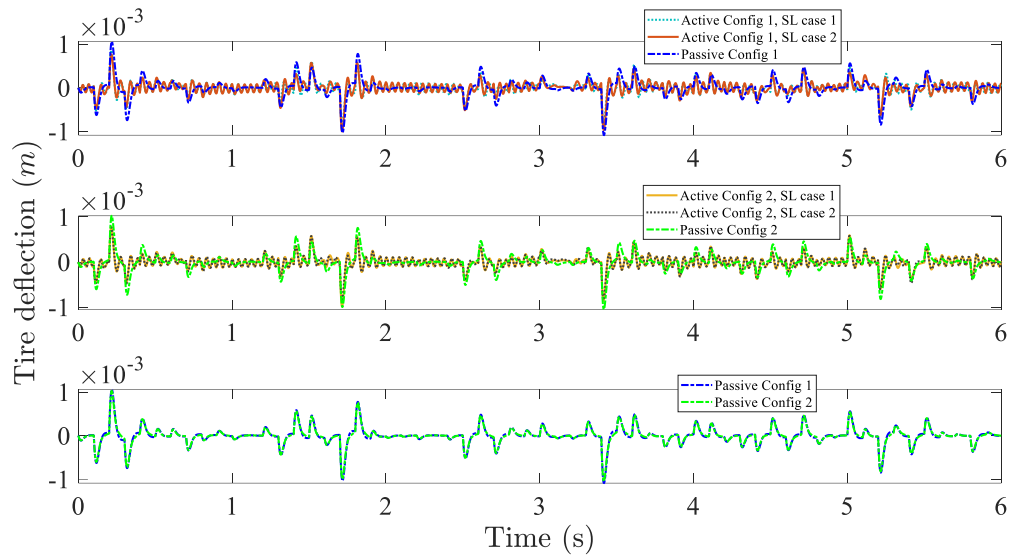Figure 4.10 Simulation results of suspension deflection under highway road

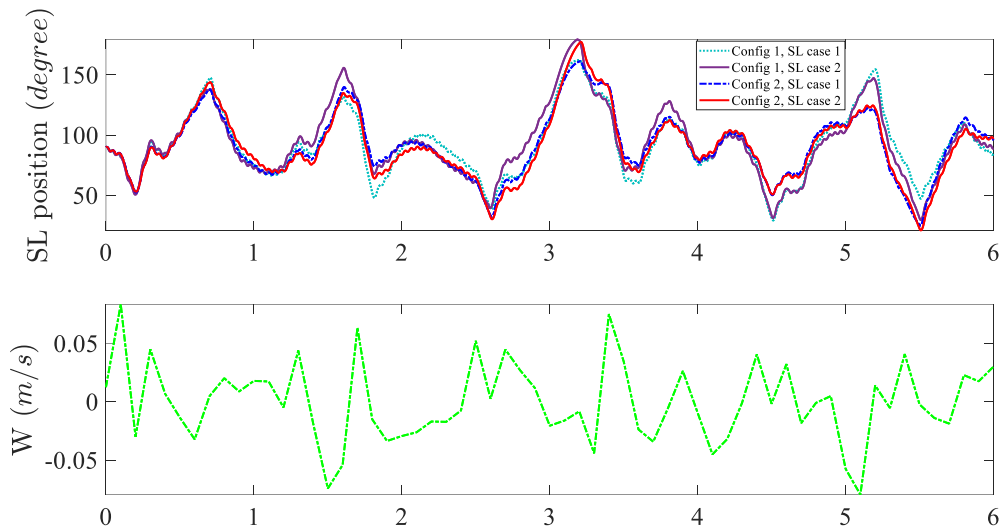Figure 4.11 Simulation results of tire deflection under highway road

Figure 4.12 Single-link position (top), highway road vertical velocity (bottom)

These above results are summarized their root-mean-square values in Table 4.1 and Table 4.2.

Table 4.1 Optimal Results for Single-link Case 1

Parameter	Symbol	Configuration 1	Configuration 2	Unit
LQR-weights	r_2	10^{14}	9.5×10^{13}	$(-)$
	r_3	9.5×10^{14}	1.5×10^{15}	$(-)$
	$N_{SAVGS,y1}$	18.578	17.490	$\left(s^{-3/2}\right)$

Optimal performance of SAVGS	$N_{SAVGS,y2}$	9.664×10^{-3}	1.162×10^{-2}	$\left(s^{1/2}\right)$
	$N_{SAVGS,y3}$	5.645×10^{-3}	5.475×10^{-3}	$\left(s^{1/2}\right)$
Performance of passive	$N_{P,y1}$	34.134	32.345	$\left(s^{-3/2}\right)$
	$N_{P,y2}$	1.928×10^{-2}	2.265×10^{-2}	$\left(s^{1/2}\right)$
	$N_{P,y3}$	7.316×10^{-3}	6.954×10^{-3}	$\left(s^{1/2}\right)$
Control input	$N_{SAVGS,u}$	1.1014	1.0596	$\left(s^{-1/2}\right)$
Ride comfort improvement SAVGS over passive C1	$PC_{SAVGS\|P_{C1},y1}$	45.57	48.76	(%)
Ride comfort improvement SAVGS over passive C2	$PC_{SAVGS\|P_{C2},y1}$	42.56	45.93	(%)

Table 4.2 Optimal Results for Single-link Case 2

Parameter	Symbol	Configuration 1	Configuration 2	Unit
LQR-weights	r_2	9×10^{18}	2×10^{25}	$(-)$
	r_3	1.5×10^{20}	4×10^{26}	$(-)$
Optimal performance of SAVGS	$N_{SAVGS,y1}$	18.834	17.048	$\left(s^{-3/2}\right)$
	$N_{SAVGS,y2}$	1.034×10^{-2}	1.139×10^{-2}	$\left(s^{1/2}\right)$
	$N_{SAVGS,y3}$	5.734×10^{-3}	5.380×10^{-3}	$\left(s^{1/2}\right)$
Control input	$N_{SAVGS,u}$	1.0998	1.0795	$\left(s^{-1/2}\right)$
Ride comfort improvement SAVGS over passive C1	$PC_{SAVGS\|P_{C1},y1}$	44.82	50.05	(%)
Ride comfort improvement SAVGS over passive C2	$PC_{SAVGS\|P_{C2},y1}$	41.77	47.29	(%)

According to the results of passive case in Table 4.1, the effect of linkage geometry significantly affected on the ride comfort performance that the passive model of configuration 1 has higher normalized sprung mass acceleration than that of configuration 2.

For the system retrofitted with SAVGS, it is illustrated that the ride comfort improvement of SAVGS retrofitted in [configuration 1, case1] is up to 45.57% and 42.56% compared to passive configuration 1 and configuration 2,

respectively. Parallelly, in [configuration 1, case2] is up to 44.82% and 41.77%, in [configuration 2, case1] is up to 48.76% and 45.93%, and in [configuration 2, case2] is up to 50.05% and 47.29%, respectively. The ride comfort improvement among two cases single-link rotation range of individual configuration are slightly different due to the less effect control of the single link far from the nominal state, as well as the ride comfort improvement respected to its passive case is no significant different even the changes in linkage geometry.

4.1.3.2 Simulation under single smooth bump road representation

To make a systematic comparisons between linear equivalent and non-linear simulations under the same road disturbance, we considered that the bandwidth frequency f_c used in respective non-linear simulations (Simscape Multibody in section 4.2.1) serves as a benchmark for the linear equivalent simulations.

1. *Plot results*

Similarly, the procedures of weighting controller for this road type and single-link rotation range are following to section 4.1.3.1. The vertical velocity of road disturbance is presented in Figure 3.20. The vehicle speed $v = 0.2777$ m/s, bump height 3.47 mm and bump width 0.14 m, respectively. Figure 4.13 and Figure 4.14 illustrated the rms sprung mass acceleration corresponding to the varied r_2 and r_3 as well, for case 1 and case 2, respectively.
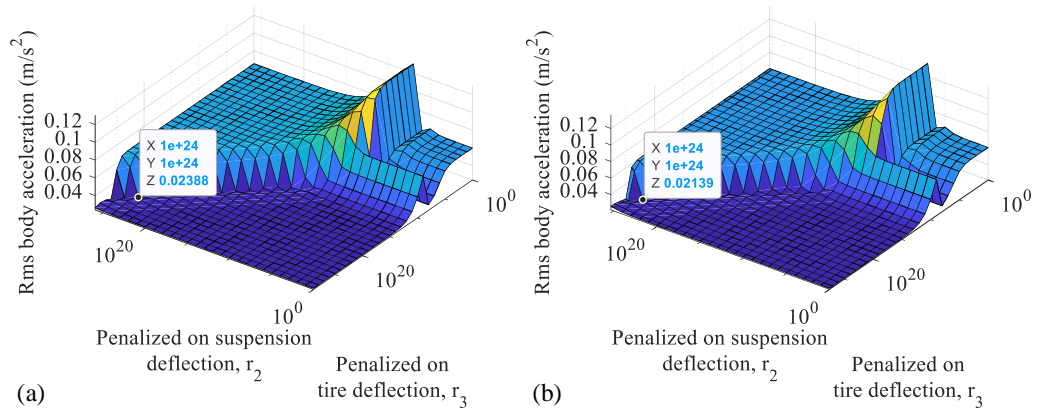
Figure 4.13 SL case 1: surface plot of the rms body acceleration performance of SAVGS under bump road, (a) configuration 1 and (b) configuration 2
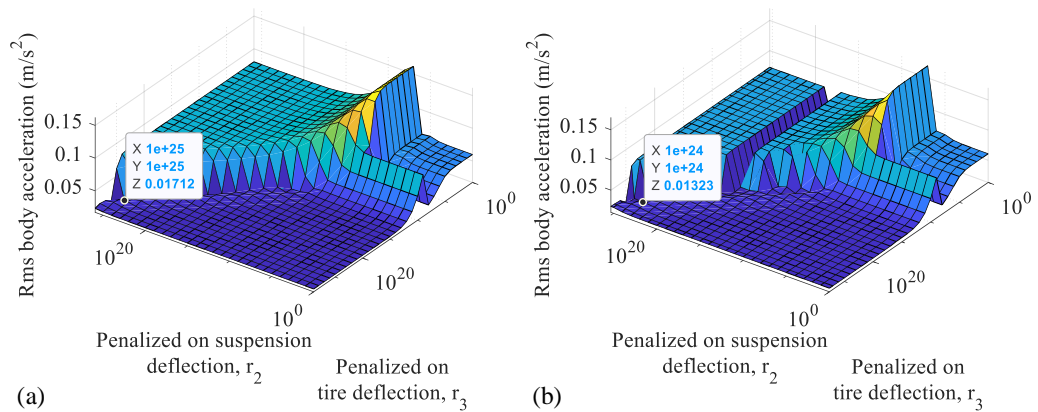

Figure 4.14 SL case 2: surface plot of the rms body acceleration performance of SAVGS under bump road, (a) configuration 1 and (b) configuration 2

For configuration 1 (**C1**) in Figure 4.13a and Figure 4.14a, the penalized coefficients are ranging the values of r_2 from 1 to 8.4×10^{25} and r_3 from 1 to 8×10^{28}. Similarly, for configuration 2 (C2) in Figure 4.3b and Figure 4.4b, those of the values of r_2 from 1 to 2×10^{25} and r_3 from 1 to 4×10^{27}. The minimal rms sprung mass accelerations in SL case 1; which are likely located at the trim state of $r_2 = 10^{24}$ and $r_3 = 10^{24}$ for **C1**, and $r_2 = 10^{24}$ and $r_3 = 10^{24}$ for **C2**; equal to 2.388×10^{-2} m/s^2, and 2.139×10^{-2} m/s^2, respectively.

Similarly, in case 2, those of values are likely located at the trim state of $r_2 = 10^{25}$ and $r_3 = 10^{25}$ for **C1**, and $r_2 = 10^{24}$ and $r_3 = 10^{24}$ for **C2**; equal to

1.712×10^{-2} m/s^2, and 1.323×10^{-2} m/s^2, respectively. Remembered that those minimal states are not incorporated the constrained suspension deflection and tire deflection yet. However, these constraints are not violated for highway road profile so that we supposed that, these constraints will not be violated at optimal control weight. After we got the optimal result, we will check for the aforementioned constraints.

Figure 4.15 to Figure 4.18 illustrate the simulation result of sprung mass acceleration, suspension deflection, tire deflection, and single-link position, respectively.
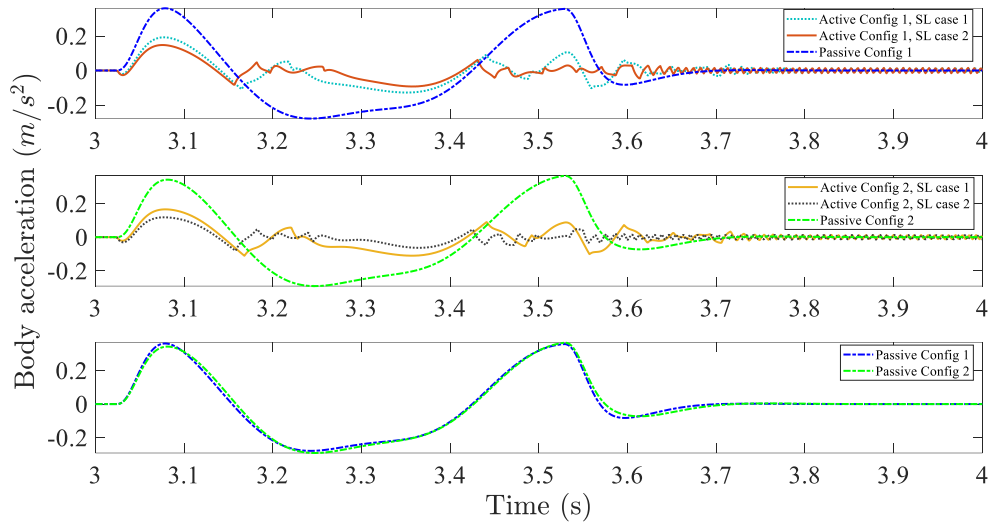
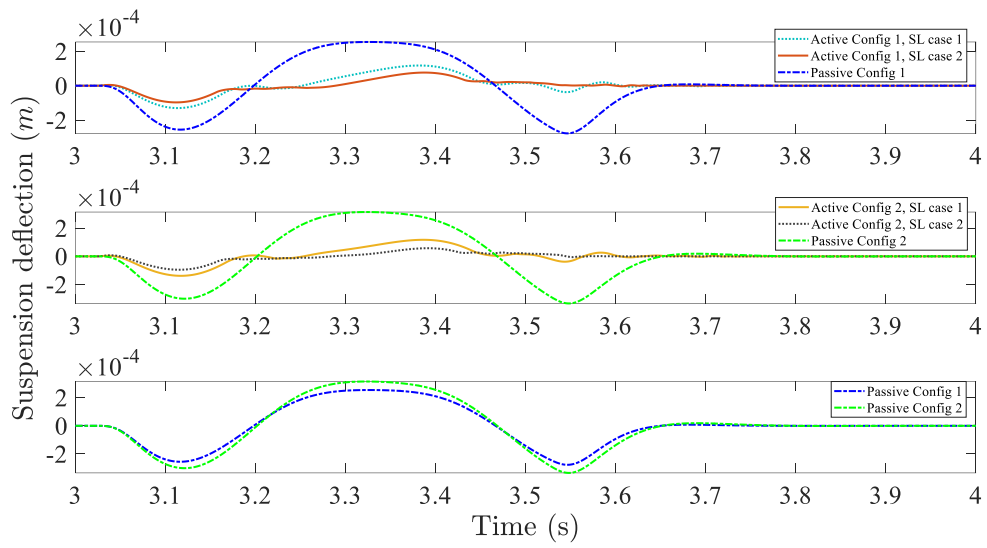Figure 4.15 Simulation results of body acceleration under bump road

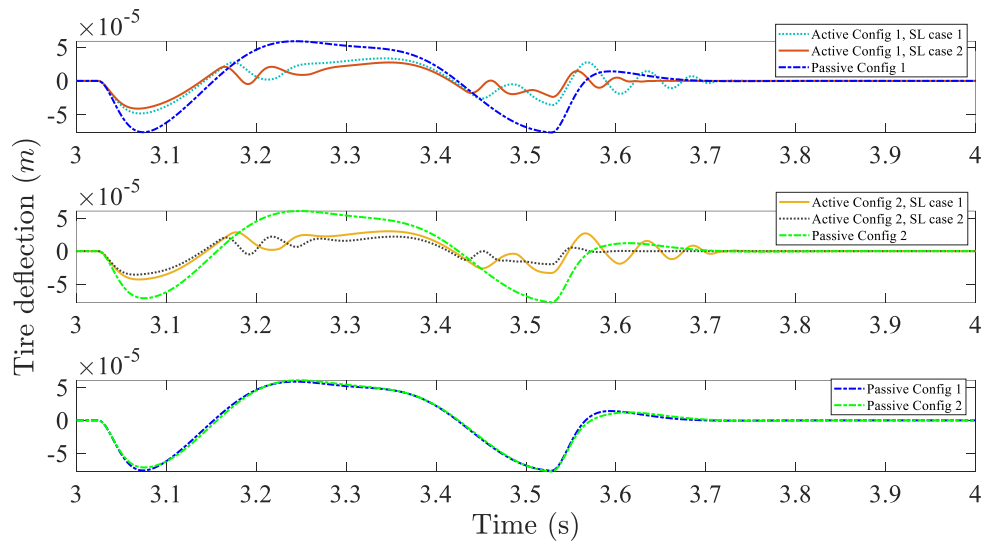Figure 4.16 Simulation results of suspension deflection under bump road

Figure 4.17 Simulation results of tire deflection under bump road
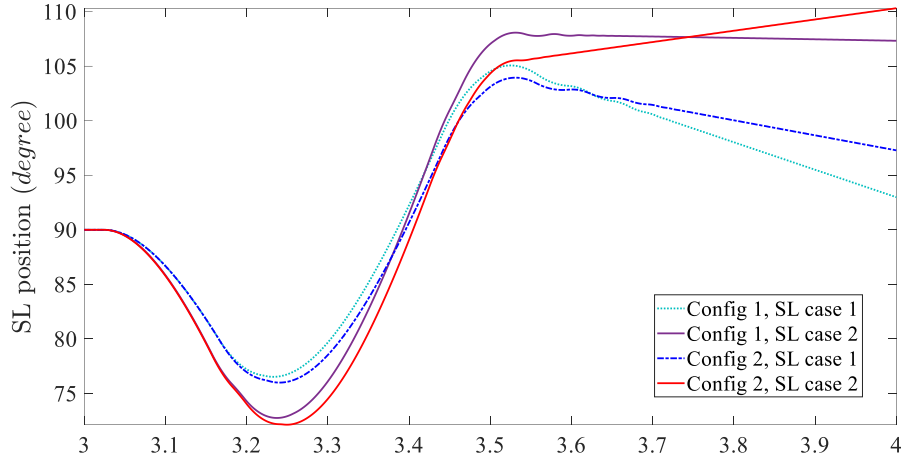
Figure 4.18 Simulation results of single position under bump road

These above results are summarized their root-mean-square values in Table 4.3 and Table 4.4.

Table 4.3 Optimal Results for Single-link Case 1

Parameter	Symbol	Configuration 1	Configuration 2	Unit
LQR-weights	r_2	10^{24}	10^{24}	$(-)$
	r_3	10^{24}	10^{24}	$(-)$
Optimal performance of SAVGS	$y1_{SAVGS}$	2.388×10^{-2}	2.139×10^{-2}	(m/s^2)
	$y2_{SAVGS}$	1.767×10^{-5}	1.787×10^{-5}	(m)
	$y3_{SAVGS}$	6.775×10^{-6}	6.353×10^{-6}	(m)
Performance of passive	$y1_p$	5.9176×10^{-2}	5.9892×10^{-2}	(m/s^2)
	$y2_p$	5.0381×10^{-5}	6.1304×10^{-5}	(m)
	$y3_p$	1.2606×10^{-5}	1.2662×10^{-5}	(m)
Control input	u_{SAVGS}	3.356×10^{-3}	3.383×10^{-3}	(m/s)
Ride comfort improvement SAVGS over passive C1	$PC_{SAVGS|P_{C1},y1}$	59.64	63.84	$(\%)$
Ride comfort improvement SAVGS over passive C2	$PC_{SAVGS|P_{C2},y1}$	60.13	64.28	$(\%)$

Table 4.4 Optimal Results for Single-link Case 2

Parameter	Symbol	Configuration 1	Configuration 2	Unit
LQR-weights	r_2	10^{25}	10^{24}	$(-)$

	r_3	10^{25}	10^{24}	$(-)$
Optimal performance of SAVGS	$y1_{SAVGS}$	1.712×10^{-2}	1.323×10^{-2}	(m/s^2)
	$y2_{SAVGS}$	1.158×10^{-5}	1.016×10^{-5}	(m)
	$y3_{SAVGS}$	5.242×10^{-6}	4.611×10^{-6}	(m)
Control input	u_{SAVGS}	3.553×10^{-3}	3.854×10^{-3}	(m/s)
Ride comfort improvement SAVGS over passive C1	$PC_{SAVGS|P_{C1},y1}$	71.07	77.64	(%)
Ride comfort improvement SAVGS over passive C2	$PC_{SAVGS|P_{C2},y1}$	71.41	77.91	(%)

According to the results of passive case in Table 4.3, the ride comfort performance under bump road still be affected by the varied linkage geometry. Unlike the results under highway road disturbance, the rms value of sprung mass acceleration of configuration 1 is lower than that of configuration 2. Observing on rms suspension deflection and rms tire deflection for all configurations and all SL cases, there are no violations with the constrained values while the maximum allowable suspension deflection $y2_{max}$ and tire deflection $y3_{max}$; $y2_{C1,max} = 18.1 \times 10^{-3}$ m and $y3_{C1,max} = 2.19 \times 10^{-3}$ m for C1, and $y2_{C2,max} = 18.67 \times 10^{-3}$ m and $y3_{C2,max} = 2.19 \times 10^{-3}$ m for C2, respectively.

For the system retrofitted with SAVGS, it is illustrated that the ride comfort improvement of SAVGS retrofitted in [configuration 1, case1] is up to 59.64% and 60.13% compared to passive configuration 1 and configuration 2, respectively. Parallelly, in [configuration 1, case2] is up to 71.07% and 71.41%, in [configuration 2, case1] is up to 63.84% and 64.28%, and in [configuration 2, case2] is up to 77.64% and 77.91%, respectively. The ride comfort improvement among two cases single-link rotation range of individual configuration are notable, as well as the ride comfort improvement of linkage configuration 2 is better than that of configuration 1.

4.2 Simscape Multibody

In section, due to the signal of highway road is complicated to present by rotation of eccentric cam, we decided to present only a bump exiting as road disturbance for **Simscape Multibody**. The simscape bloc built is referring to Figure 3.24.

4.2.1 Influence of Bandwidth

The influence of bandwidth in this section is followed the procedure as in section 4.1.2 above. The weighted controller seeking for the minimum vertical sprung mass acceleration under bump road disturbance at low pass frequency 1 Hz are likely located at; $r_1 = 4 \times 10^4$ and $r_3 = 10^{-6}$, and $r_1 = 4 \times 10^4$ and $r_3 = 7 \times 10^{-5}$ for configuration 1 and configuration 2, respectively. These weighting values are used for the respective configuration to study the influence of bandwidth frequency in which Figure 4.19 illustrates.
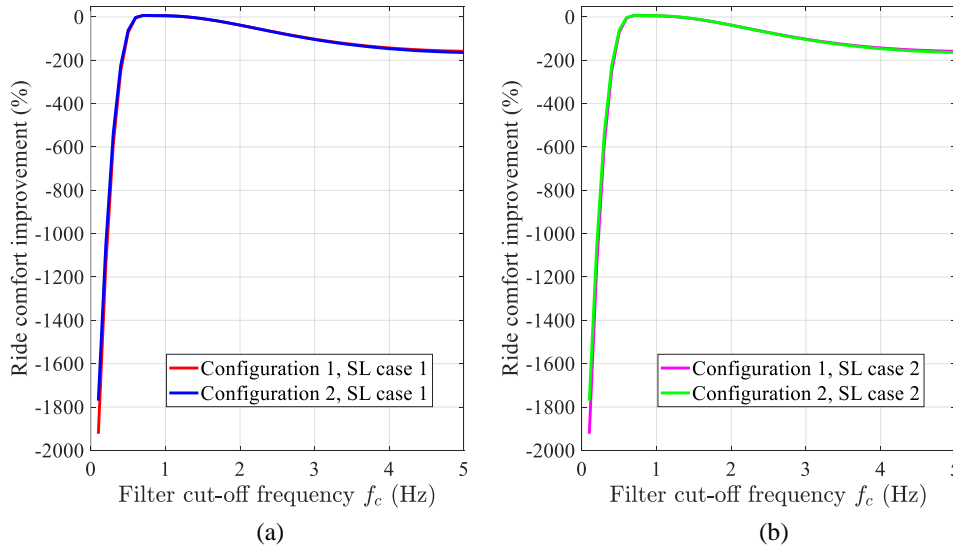
Figure 4.19 Ride comfort depending f_c: (a) Single-link rotation range case 1, (b) Single-link rotation range case 2.

Observing on Figure 4.19, the ride comfort improvements depending bandwidth frequency under a bump road likely have higher values at $f_c = 0.7$ Hz for all suspension configurations and all cases of SL rotation range. This low pass

frequency value will be used for iteratively seeking the optimal performance of SAVGS in **Sim mechanic**.

4.2.2 Plot results

In order to point out the effect of SAVGS retrofitted in passive system as well as to compare those of different linkage geometries; the weighted on suspension deflection $(\boldsymbol{r_2})$ is fixed at value of **1** and the others, r_1 and r_3, are varied in wide range; whereas the linear simulation in section 4.1.3 varied on r_2 and r_3 only. In physical model, vertical suspension deflection is severely nonlinear of which the controller weight could not produce the better performances. However, controller weighting on r_1 and r_3 is conducted in [2] as well so that we can use this approach for our benchmark controller weighting.

The single-link rotation range of both cases following the same as in linear equivalent model. Vehicle speed $v = 0.2777$ m/s and bump width 0.14 m, which are ten times scaled down of those of values in [2] due to the mini-scale of our system. However, the exciting frequency still be the same as that of in [2]. The road disturbance induced by aforementioned properties can be seen in Figure 3.19. Figure 4.20 and Figure 4.21 illustrated the rms sprung mass acceleration corresponding to the varied r_1 and r_3 as well, for SL case 1 and case 2, respectively.
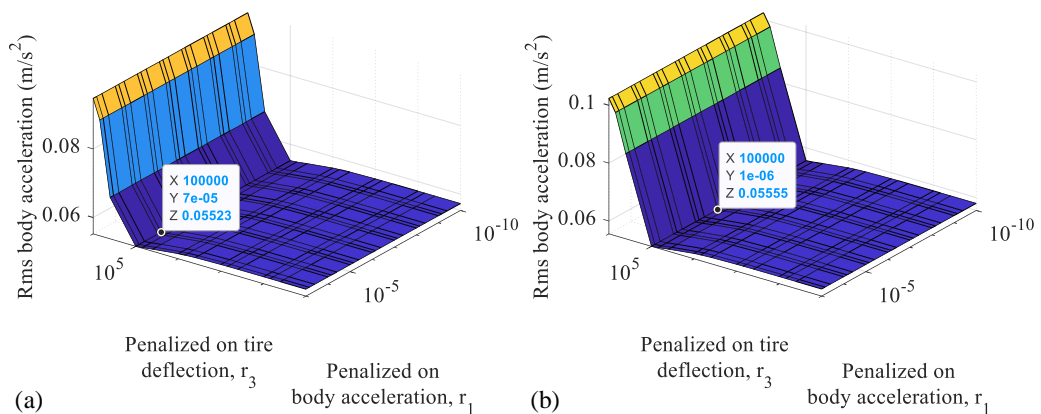

Figure 4.20 SL case 1: surface plot of the rms body acceleration performance of SAVGS under bump road, (a) configuration 1 and (b) configuration 2
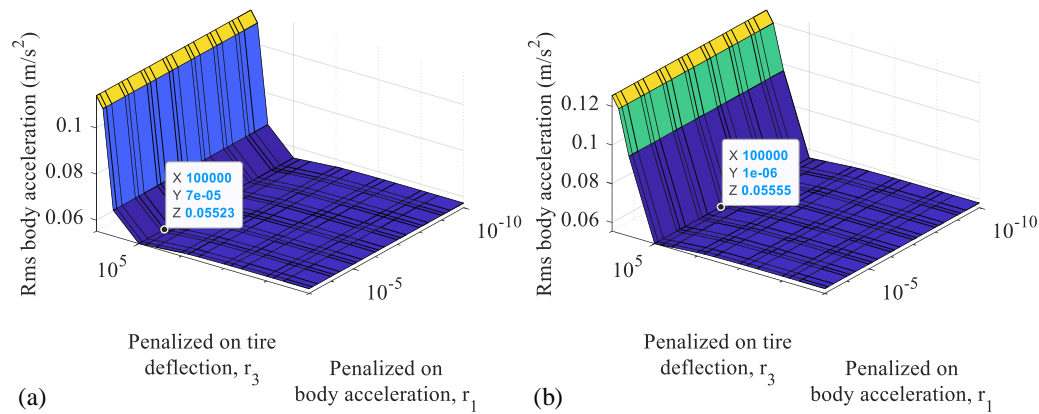
Figure 4.21 SL case 2: surface plot of the rms body acceleration performance of SAVGS under bump road, (a) configuration 1 and (b) configuration 2

From Figure 4.20 to Figure 4.21, the penalized coefficients are ranging the values of r_1 from 10^{-10} to 10^{-3} and r_3 from 10 to 10^6. The minimal rms sprung mass accelerations in linkage configuration 1; which are likely located at the trim state of $r_1 = 7 \times 10^{-5}$ and $r_3 = 10^5$ for both SL cases; equal to 5.523×10^{-2} m/s^2. Similarly, in linkage configuration 2, those of values are likely located at the trim state of $r_1 = 10^{-6}$ and $r_3 = 10^5$ for both SL cases; equal to 5.555×10^{-2} m/s^2. The suspension deflection and tire deflection incorporated with these constraints will be checked later.

Figure 4.22 to Figure 4.25 illustrate the simulation result of sprung mass acceleration, suspension deflection, tire deflection, and single-link position and power required, respectively.
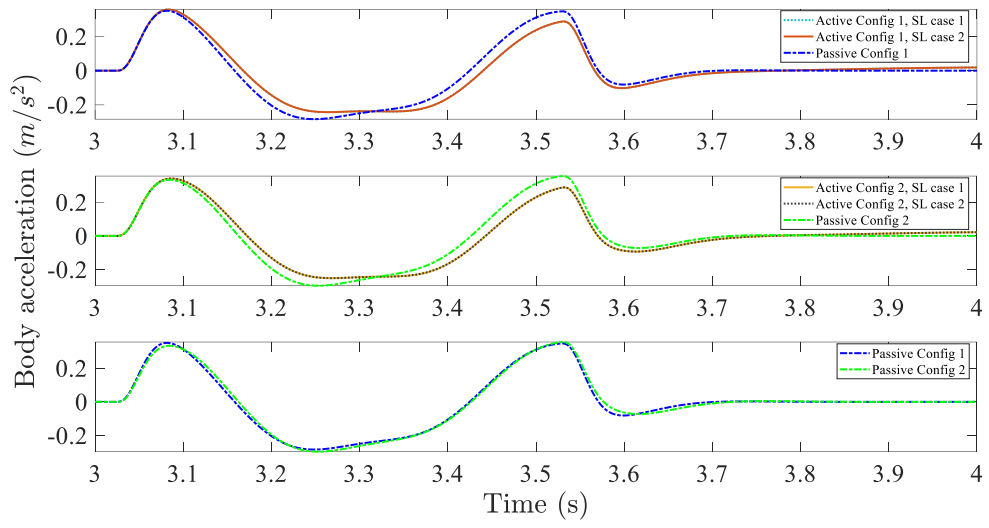
Figure 4.22 Simulation results of body acceleration under bump road
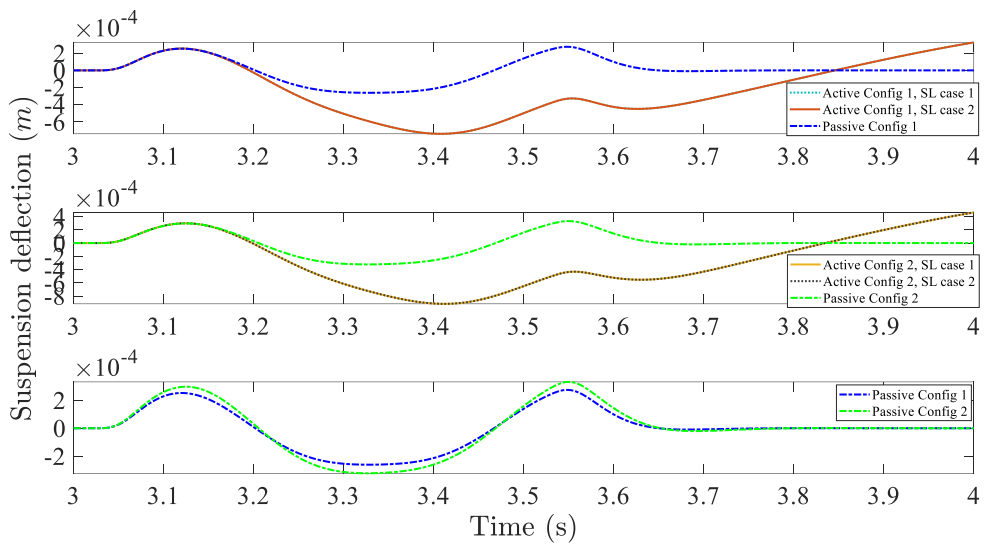
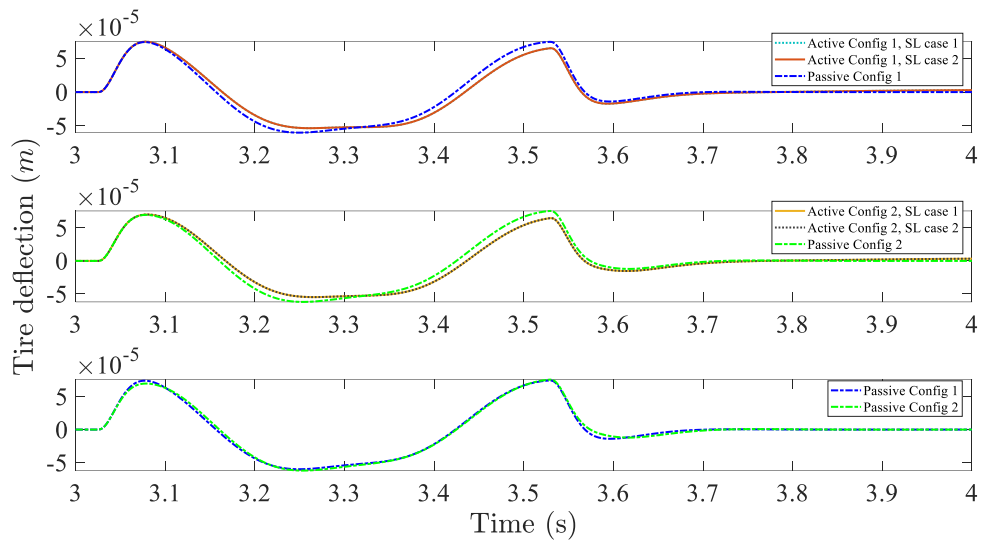Figure 4.23 Simulation results of suspension deflection under bump road

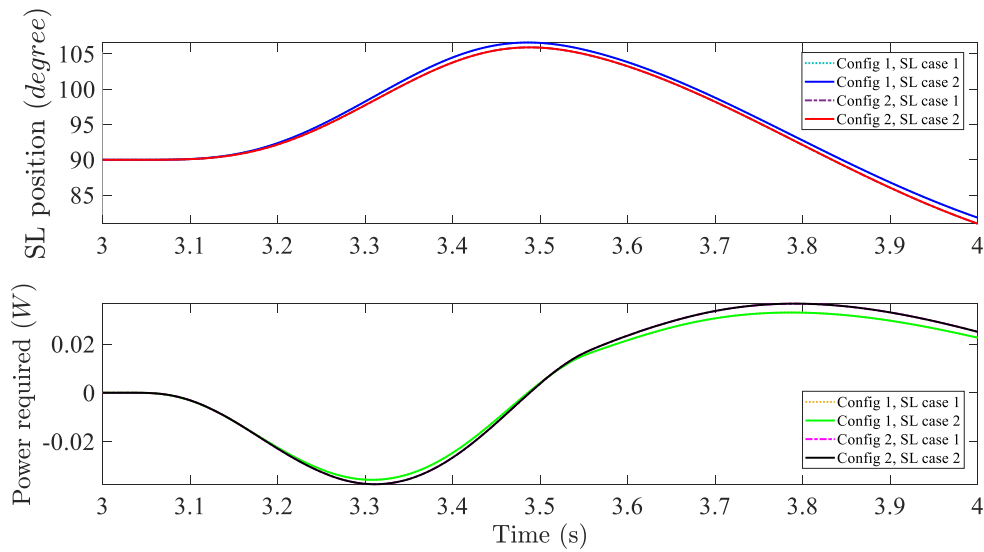Figure 4.24 Simulation results of tire deflection under bump road

Figure 4.25 Simulation results of single position (top), single-link power required (bottom)

These above results are summarized their root-mean-square values in Table 4.5 and Table 4.6.

Table 4.5 Optimal Results for Single-link Case 1

Parameter	Symbol	Configuration 1	Configuration 2	Unit
LQR-weights	r_1	7×10^{-5}	10^{-6}	$(-)$

	r_3	10^5	10^5	$(-)$
Optimal performance of SAVGS	$y1_{SAVGS}$	5.523×10^{-2}	5.555×10^{-2}	(m/s^2)
	$y2_{SAVGS}$	1.949×10^{-4}	2.578×10^{-4}	(m)
	$y3_{SAVGS}$	1.187×10^{-5}	1.184×10^{-5}	(m)
Performance of passive	$y1_p$	5.8947×10^{-2}	5.9736×10^{-2}	(m/s^2)
	$y2_p$	5.0595×10^{-5}	6.1511×10^{-5}	(m)
	$y3_p$	1.2568×10^{-5}	1.2637×10^{-5}	(m)
Ride comfort improvement SAVGS over passive C1	$PC_{SAVGS|P_{C1},y1}$	6.30	5.76	(%)
Ride comfort improvement SAVGS over passive C2	$PC_{SAVGS|P_{C2},y1}$	7.53	7.01	(%)

Table 4.6 Optimal Results for Single-link Case 2

Parameter	Symbol	Configuration 1	Configuration 2	Unit
LQR-weights	r_2	7×10^{-5}	10^{-6}	$(-)$
	r_3	10^5	10^5	$(-)$
Optimal performance of SAVGS	$y1_{SAVGS}$	5.523×10^{-2}	5.555×10^{-2}	(m/s^2)
	$y2_{SAVGS}$	1.949×10^{-4}	2.578×10^{-4}	(m)
	$y3_{SAVGS}$	1.187×10^{-5}	1.184×10^{-5}	(m)
Ride comfort improvement SAVGS over passive C1	$PC_{SAVGS|P_{C1},y1}$	6.30	5.76	(%)
Ride comfort improvement SAVGS over passive C2	$PC_{SAVGS|P_{C2},y1}$	7.53	7.01	(%)

According to the results of passive case in Table 4.5, the ride comfort performance characteristics are as similar as that of simulations in section 4.1.3.2 where the rms value of sprung mass acceleration of configuration 1 is lower than that of configuration 2. Observing on rms suspension deflection and rms tire deflection for all configurations and all SL cases, there are no violations with the constrained values as well. Moreover, the road holding quality also could can improved.

For the system retrofitted with SAVGS, it is illustrated that the ride comfort improvement of SAVGS retrofitted in configuration 1 is up to 6.30% and 7.53% compared to passive configuration 1 and configuration 2, respectively. Parallelly, in configuration 2 is up to 5.76% and 7.01% compared to passive configuration 1 and configuration 2, respectively. Observing on the plotted results and rms values listed in table above, it illustrates that there is no different ride comfort improvement among two cases of single-link rotation range of individual linkage configuration due to the farther from nominal state of SL and the higher non-linearity of physical model. However, the ride comfort respect to individual passive suspension can be seen that the SAVGS configuration 2 is a little bit better than that of configuration 1, whereas the ride comfort quality of SAVGS configuration 1 is better than that of SAVGS configuration 2.

Investigating on passive suspension results of bump road disturbing between linear equivalent model and physical model, the absolute error of root-mean-square values of body acceleration compared to the non-linear models are reasonably small enough, 0.39% and 0.26% for linkage configuration 1 and configuration 2, respectively. These qualities illustrated that our linear passive suspension models are sufficiently acceptable.

For the active suspensions with SAVGS, on the other hand, it is highly different ride comfort improvement among these two models. These high differences are the resulted of highly non-linearity of double wishbone arrangement and SAVGS bloc. However, the improvement results in **Sim mechanic** model would be acceptable enough. Furthermore, if we observe on the ride comfort improvement corresponded to their passive cases, the active configuration 2 is better improve. In physical meaning, if the single-link actuator commands the same angle to both configurations, the height of center wheel-hub in configuration 2 can adjust higher than that of in configuration 1. Higher center wheel-hub height adjustment means that the controller can handle higher road disturbance magnitude that why we got the gamma value at nominal state of single-link in configuration 2 greater than that of in configuration 1.

CHAPTER 5
CONCLUSIONS

The potential of series active variable geometry suspension retrofitted in passive system is studied. Linear equivalent model and Physical model (*Simscape multibody*) have been conducted. The linear equivalent model with full analysis of kinematic linkage of double wishbone arrangement and linkage of SAVGS can be served as a benchmark for designing the suspension system. The performances of system dynamic have been compared among the varied linkage geometries for SAVGS and those of for passive cases. The single-link angle ranges are studied in two cases, $20^o \leq \Delta\alpha_{SL} \leq 160^o$ and $0^o \leq \Delta\alpha_{SL} \leq 180^o$ for cases 1 and 2, respectively. The linear equivalent model of the quarter car based on energy conservation is adopted in synthesis LQR controller, the different linkage geometry resulting the differences in k_{eq} and c_{eq}. Chosen k_{eq} and c_{eq} at nominal state of single-link at which the SAVGS controller incorporated with lowpass filter and controlling DC motor are iteratively weighted on each feedback parameter that commanding the compensated nonlinearity of single-link bloc. The optimal weights are aimed to achieve the optimal of ride comfort (rms vertical sprung mass acceleration) and road holding (rms dynamic tire deflection) of individual suspension configuration.

In passive case, the root-mean-square of vertical sprung mass acceleration has been compared respect to non-linear models, the absolute errors are approximately 0.39% and 0.26% for linkage configuration 1 and configuration 2, respectively. The aforementioned root-mean-square is affected by the variation of linkage geometry. It becomes worse or better compared with the reference geometry depending on the road disturbance types. In highway road profile representation, the rms vertical sprung mass acceleration in configuration 2 is smaller 5.24% than configuration 1's. In contrast, road smooth bump representation, that value in configuration 2 is greater 1.21% and 1.34% than configuration 1's for the linear and non-linear models, respectively.

On the other hand, active case with SAVGS, the ride comfort improvement respected to corresponding passive case has illustrated that this quality in linkage configuration 2 is somehow slightly better than configuration 1's. Physically, the height of center wheel-hub in configuration 2 enabling to be adjusted higher than that of in configuration 1 when the single-link actuator command the same angles. The controller can handle higher road disturbance magnitude when there is higher center wheel-hub height adjustment. For highway road profile, the ride comfort improvement corresponded to their passive case are up to 45.57%, 45.93%, 44.82%, and 47.29% for the SAVGS in [linkage configuration 1; SL case 1], [linkage configuration 2; SL case 1], [linkage configuration 1; SL case 2], and [linkage configuration 2; SL case 2], respectively. However, the single-link rotation among two cases result less differences in ride comfort improvement for the non-linear models. The aforementioned quality improvement in non-linear model under bump road is 6.30% and 7.01% for linkage configuration 1 and configuration 2. Interestingly, the road holding quality also has been improved along with the linear equivalent and non-linear models.

Future work recommendations, implement the linearization theories and the designed controller into real prototype to further study their effects on dynamic response of suspension system.

REFERENCES

[1]   M. Yu, S. A. Evangelou, and D. Dini, "Model identification and control for a quarter car test rig of series active variable geometry suspension," *IFAC-PapersOnLine*, vol. 50, no. 1, pp. 3376–3381, 2017.

[2]   M. Yu, C. Arana, S. A. Evangelou, and D. Dini, "Quarter-car experimental study for series active variable geometry suspension," *IEEE Trans. Control Syst. Technol.*, vol. 27, no. 2, pp. 743–759, 2017.

[3]   M. Omar, M. M. El-Kassaby, and W. Abdelghaffar, "A universal suspension test rig for electrohydraulic active and passive automotive suspension system," *Alexandria Eng. J.*, vol. 56, no. 4, pp. 359–370, 2017.

[4]   S. Ikenaga, F. L. Lewis, J. Campos, and L. Davis, "Active suspension control of ground vehicle based on a full-vehicle model," in *Proceedings of the 2000 American Control Conference. ACC (IEEE Cat. No. 00CH36334)*, 2000, vol. 6, pp. 4019–4024.

[5]   S. R. Kristiadi and U. Wasiwitono, "Effect of feedback measurement on LQG control for Low Bandwidth Active Suspension system," in *2015 International Conference on Advanced Mechatronics, Intelligent Manufacture, and Industrial Automation (ICAMIMIA)*, 2015, pp. 42–45.

[6]   C. Arana, S. A. Evangelou, and D. Dini, "Pitch angle reduction for cars under acceleration and braking by active variable geometry suspension," in *2012 IEEE 51st IEEE Conference on Decision and Control (CDC)*, 2012, pp. 4390–4395.

[7]   C. Cheng, S. A. Evangelou, C. Arana, and D. Dini, "Active variable geometry suspension robust control for improved vehicle ride comfort and road holding," in *2015 American Control Conference (ACC)*, 2015, pp. 3440–3446.

[8]   Y. M. Sam, M. R. H. A. Ghani, and N. Ahmad, "LQR controller for active car suspension," in *2000 TENCON Proceedings. Intelligent Systems and Technologies for the New Millennium (Cat. No. 00CH37119)*, 2000, vol. 1, pp. 441–444.

[9]   M. A. Nekoui and P. Hadavi, "Optimal control of an active suspension

system," in *Proceedings of 14th International Power Electronics and Motion Control Conference EPE-PEMC 2010*, 2010, pp. T5-60.

[10] A. Agharkakli, G. S. Sabet, and A. Barouz, "Simulation and analysis of passive and active suspension system using quarter car model for different road profile," *Int. J. Eng. Trends Technol.*, vol. 3, no. 5, pp. 636–644, 2012.

[11] C. Yue, T. Butsuen, and J. K. Hedrick, "Alternative control laws for automotive active suspensions," 1989.

[12] G. Koch, O. Fritsch, and B. Lohmann, "Potential of low bandwidth active suspension control with continuously variable damper," *Control Eng. Pract.*, vol. 18, no. 11, pp. 1251–1262, 2010.

[13] C. Arana, S. A. Evangelou, and D. Dini, "Series active variable geometry suspension application to comfort enhancement," *Control Eng. Pract.*, vol. 59, pp. 111–126, 2017.

[14] U. Wasiwitono, A. S. Pramono, and I. N. Sutantra, "Study on influences of linkage geometry on actively controlled double wishbone suspension," in *AIP Conference Proceedings*, 2018, vol. 1983, no. 1, p. 30009.

[15] M. S. Kumar and S. Vijayarangan, "Design of LQR controller for active suspension system," 2006.

[16] R. Darus and Y. M. Sam, "Modeling and control active suspension system for a full car model," in *2009 5th International Colloquium on Signal Processing & Its Applications*, 2009, pp. 13–18.

[17] M. Kaleemullah, W. F. Faris, and F. Hasbullah, "Design of robust H∞, fuzzy and LQR controller for active suspension of a quarter car model," in *2011 4th International Conference on Mechatronics (ICOM)*, 2011, pp. 1–6.

[18] C. Arana, S. A. Evangelou, and D. Dini, "Series active variable geometry suspension for road vehicles," *IEEE/ASME Trans. Mechatronics*, vol. 20, no. 1, pp. 361–372, 2014.

[19] C. Arana, S. A. Evangelou, and D. Dini, "Series active variable geometry suspension application to chassis attitude control," *IEEE/ASME Trans. Mechatronics*, vol. 21, no. 1, pp. 518–530, 2015.

[20] C. Arana, S. A. Evangelou, and D. Dini, "Car attitude control by series mechatronic suspension," *IFAC Proc. Vol.*, vol. 47, no. 3, pp. 10688–10693,

2014.

[21]   R. L. Williams and D. A. Lawrence, *Linear state-space control systems*. John
        Wiley & Sons, 2007.

[22]   "Control Tutorials for MATLAB and Simulink - Motor Speed: System
        Modeling."
        http://ctms.engin.umich.edu/CTMS/index.php?example=MotorSpeed&sect
        ion=SystemModeling (accessed Jun. 29, 2020).

[23]   "FAULHABER   CXR   2657   ...   CXR."
        https://www.faulhaber.com/en/products/series/2657cxr/ (accessed Jun. 29,
        2020).

[24]   N. S. Nise, *CONTROL SYSTEMS ENGINEERING, (With CD)*. John Wiley
        & Sons, 2007.

[25]   U. Wasiwitono and I. N. Sutantra, "Constrained $\mathcal{H}\infty$ control for low
        bandwidth active suspensions," in *AIP Conference Proceedings*, 2017, vol.
        1867, no. 1, p. 20032.

[26]   "Get   Started   with   Simscape   Multibody."
        https://www.mathworks.com/help/physmod/sm/getting-started-with-
        simmechanics.html (accessed Jun. 13, 2020).

[27]   "Simscape Multibody Contact Forces Library - File Exchange - MATLAB
        Central."   https://www.mathworks.com/matlabcentral/fileexchange/47417-
        simscape-multibody-contact-forces-library (accessed Jun. 14, 2020).

This page is blank

Appendix 1

Quarter-car component dimensions
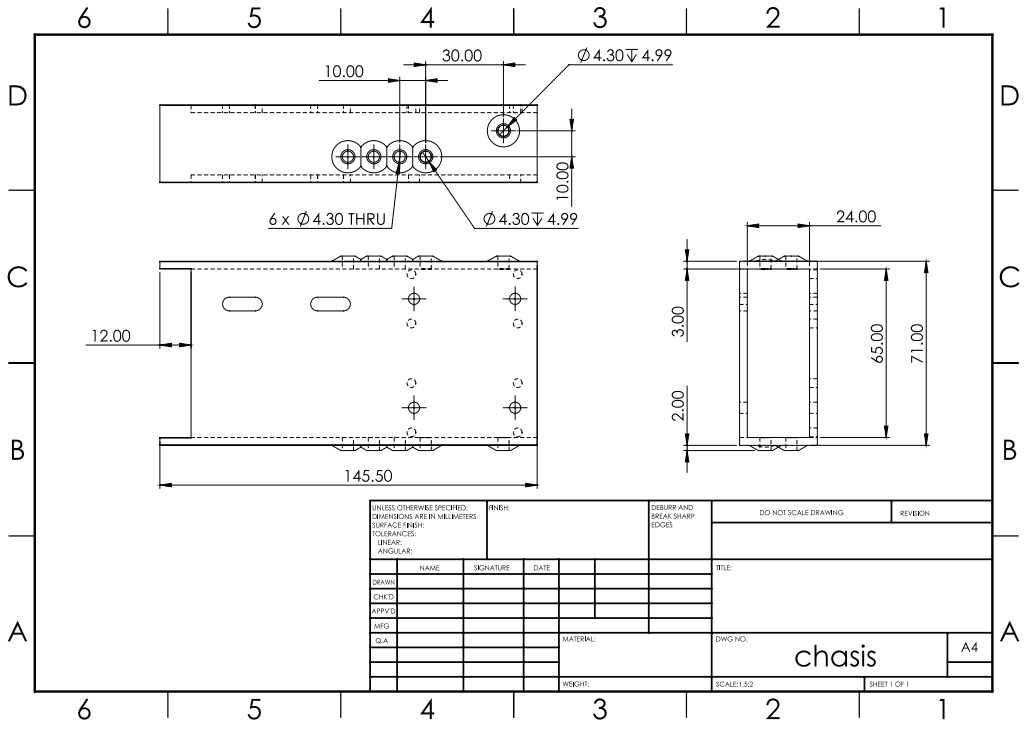
Fig. 1 Chassis dimension
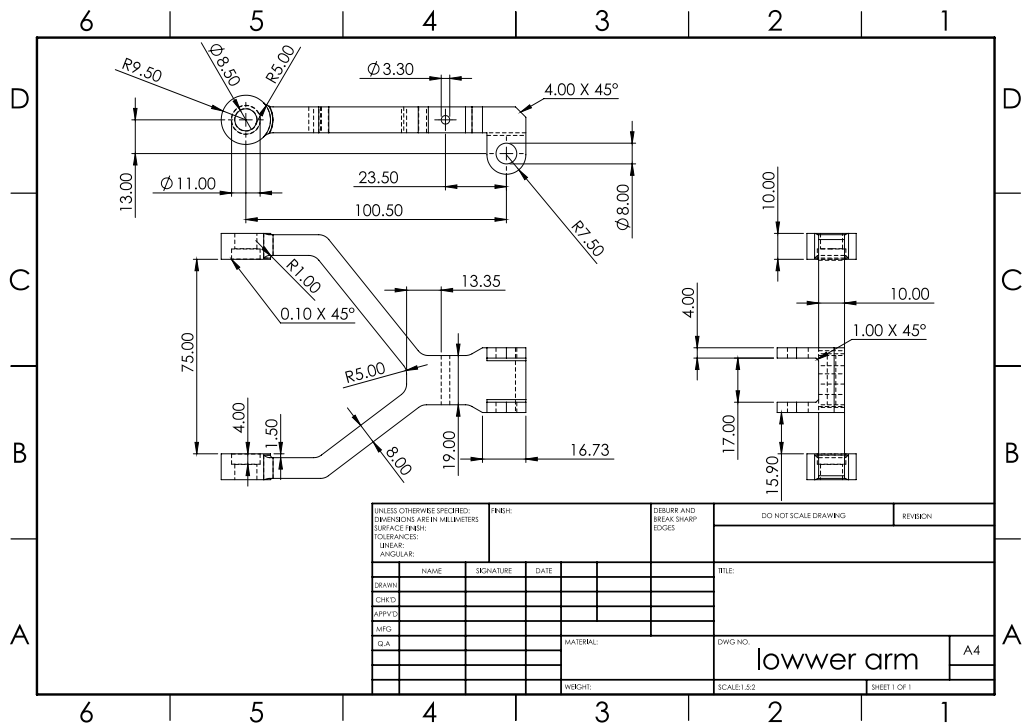
Fig. 2 Lower arm dimension for configuration 1
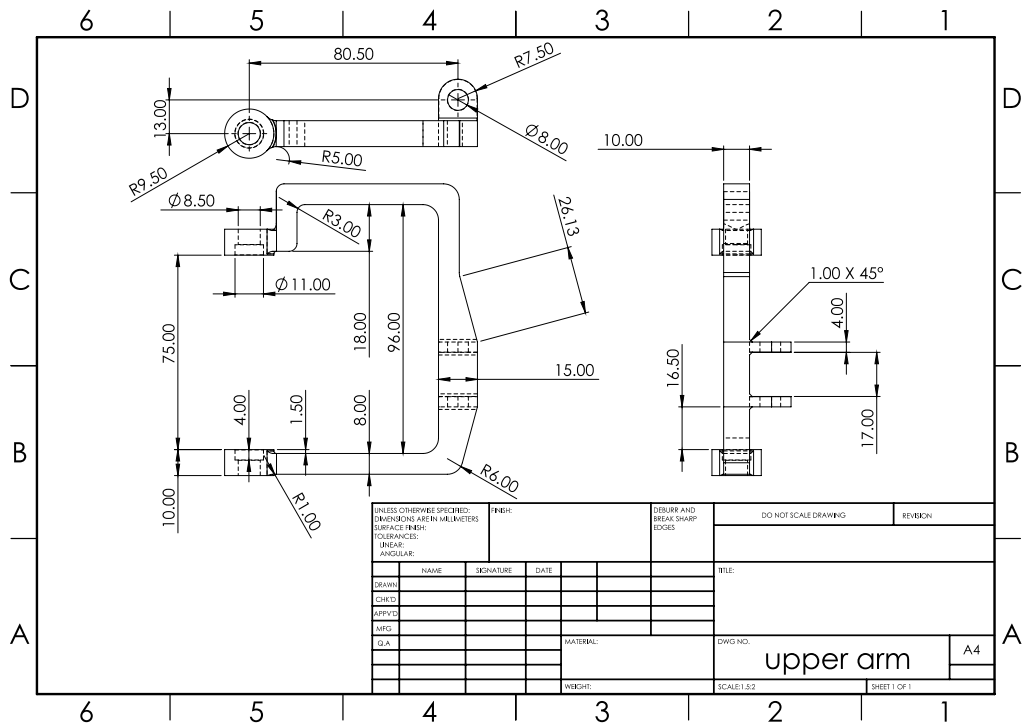
Fig. 3 Upper arm dimension for configuration 1
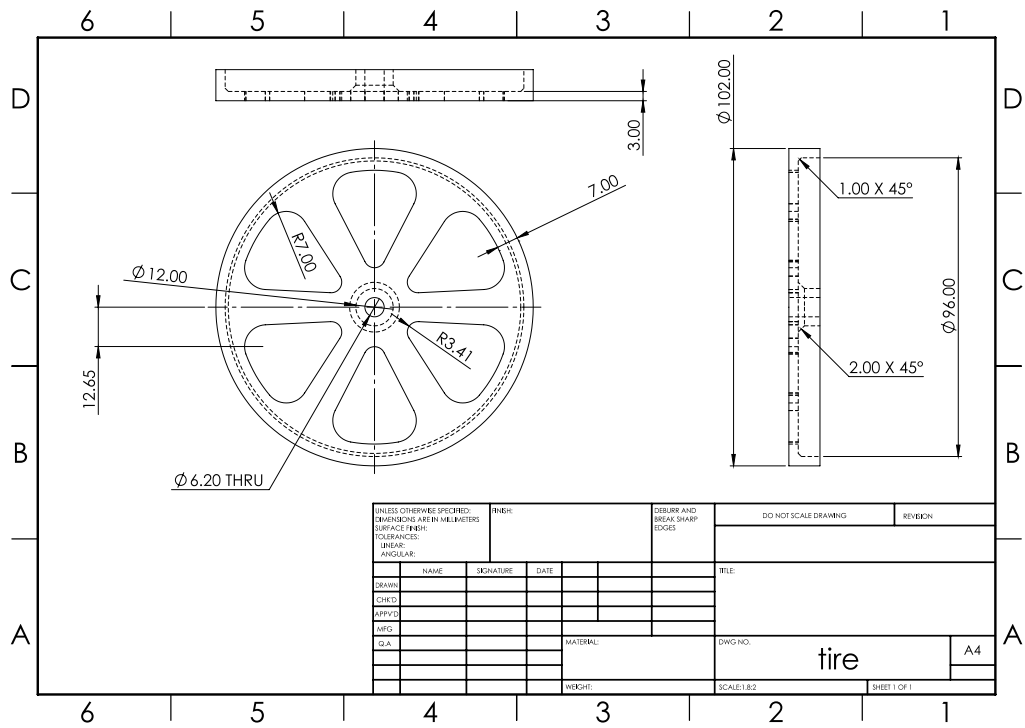
Fig. 4 Tire dimension
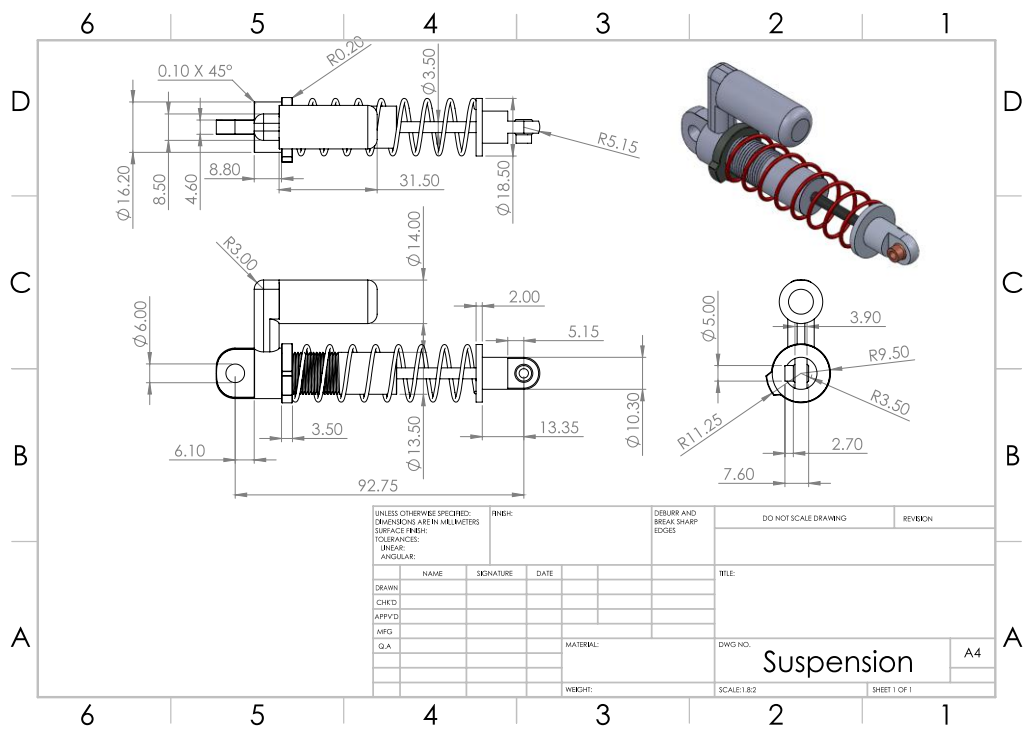
Fig. 5 Spring-damper unit dimension

Fig. 6 Knuckle wheel hub dimension for configuration 1

Fig. 7 Knuckle washer dimension
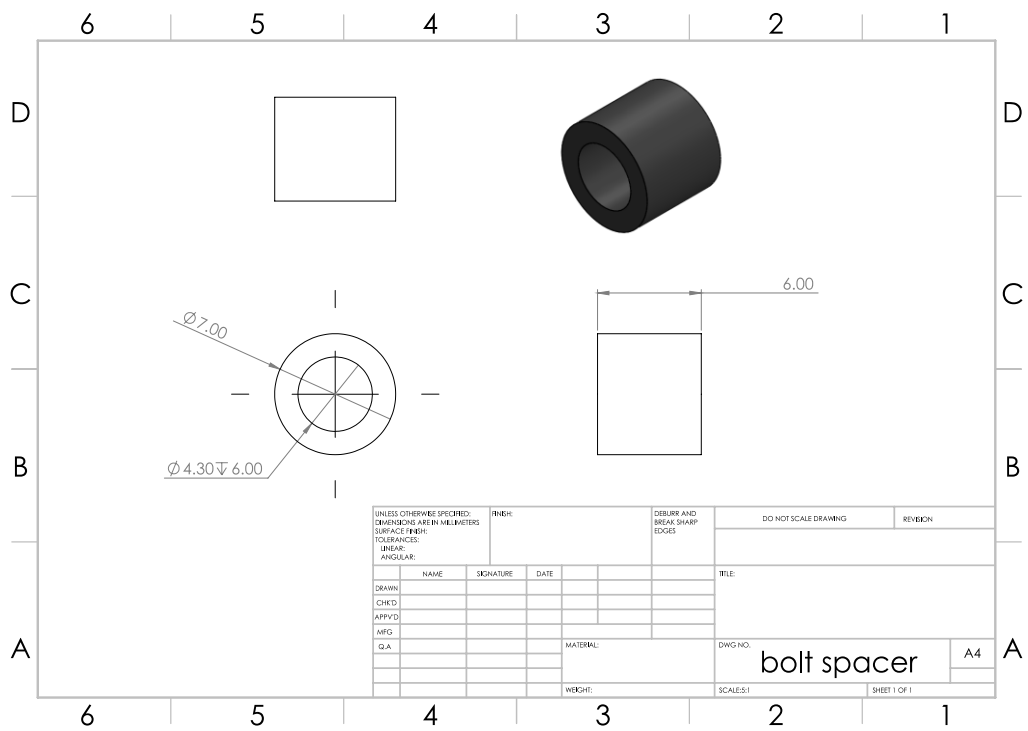
Fig. 8 Bolt spacer dimension
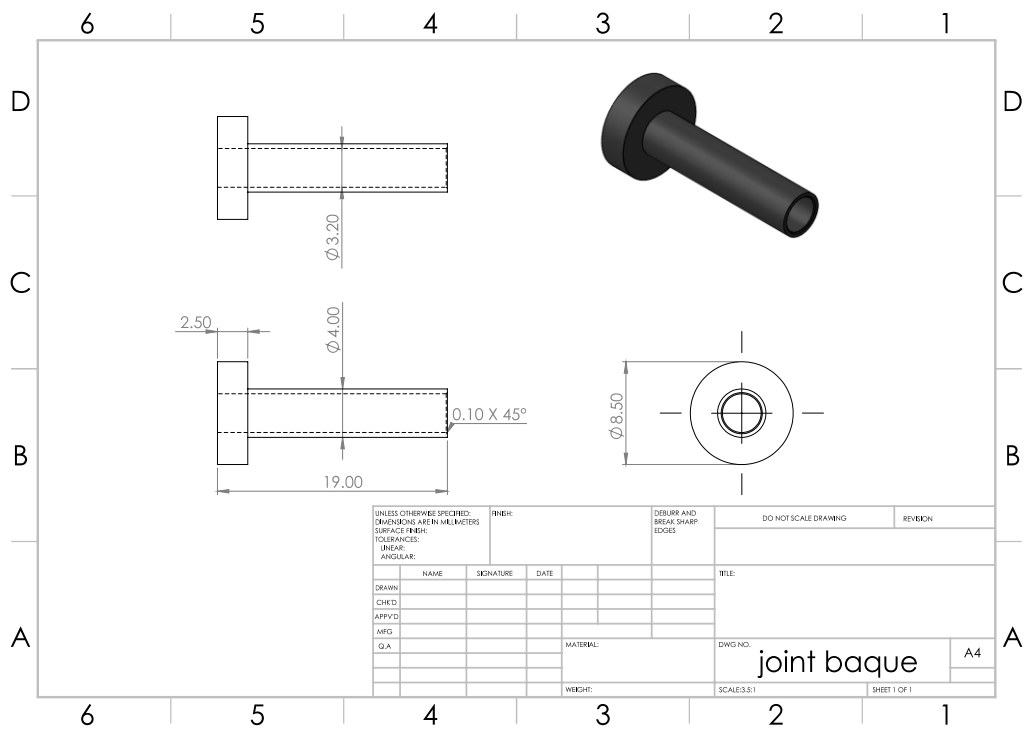
Fig. 9 Joint baque dimension
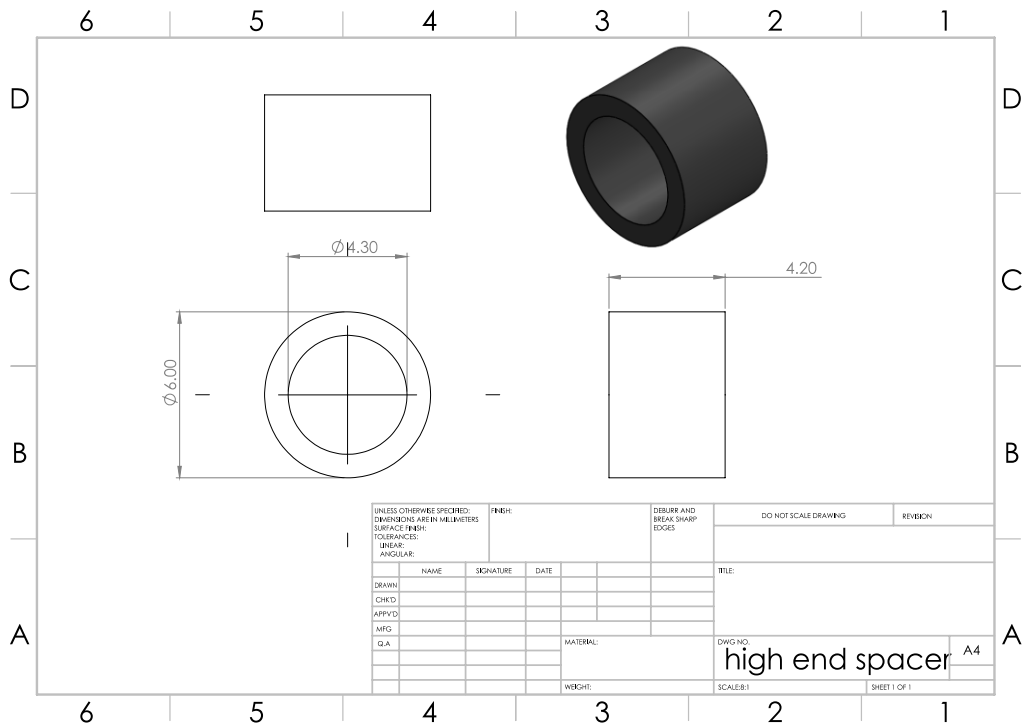
Fig. 10 High-end spacer dimension
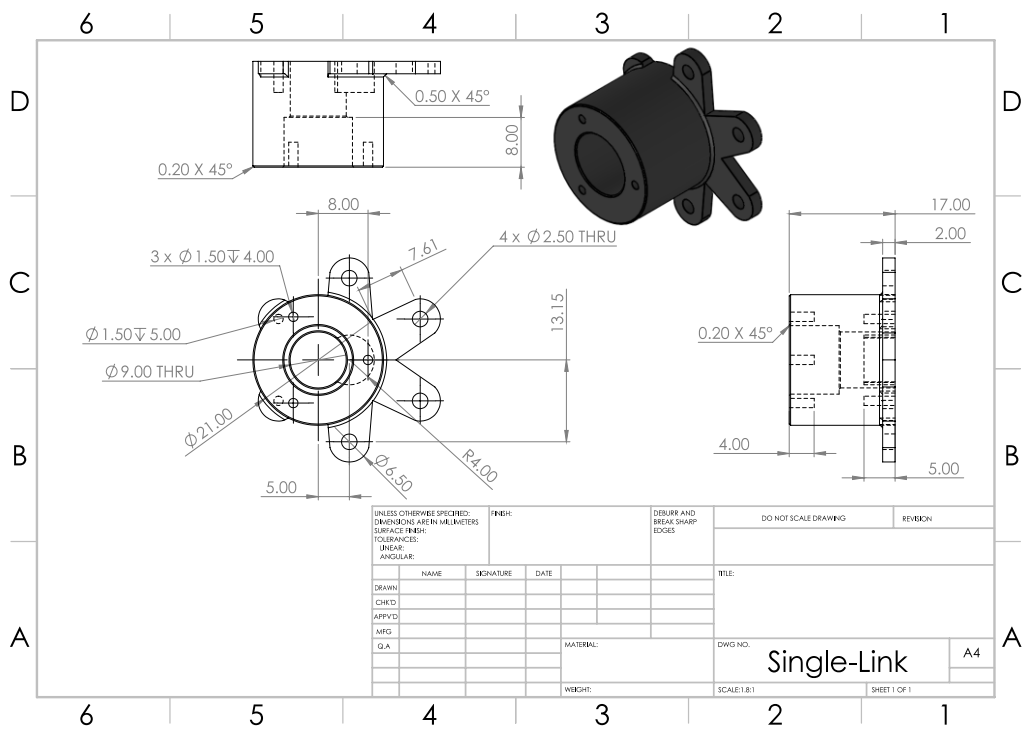
Fig. 11 Single-link dimension
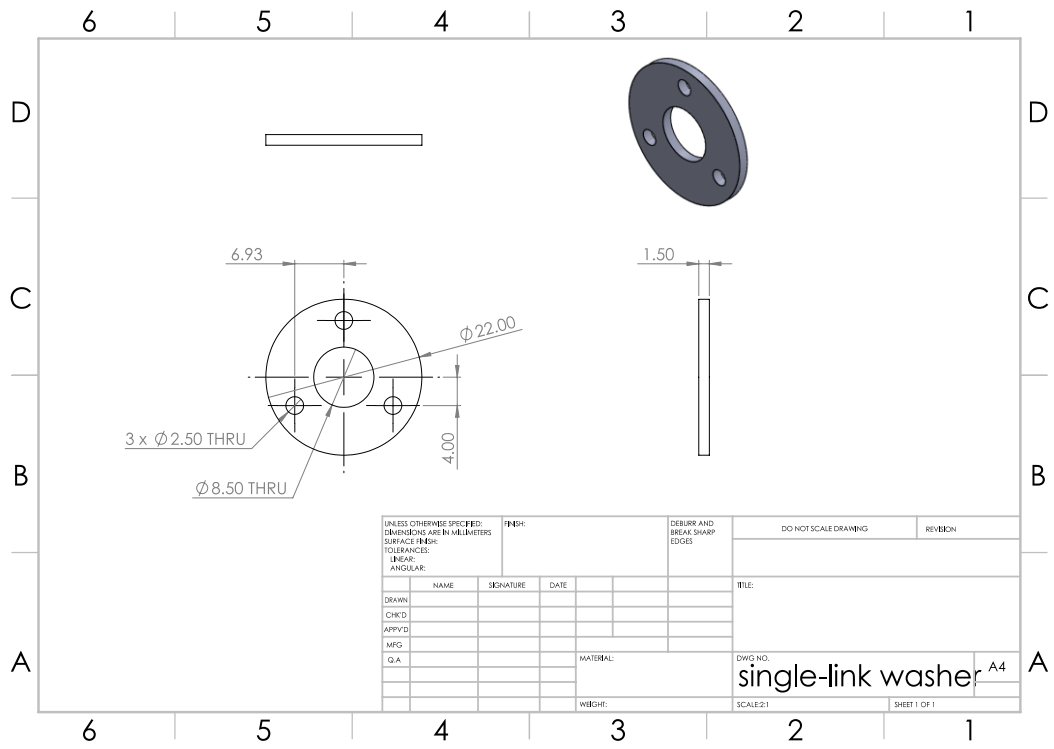
Fig. 12 Single-link washer dimension
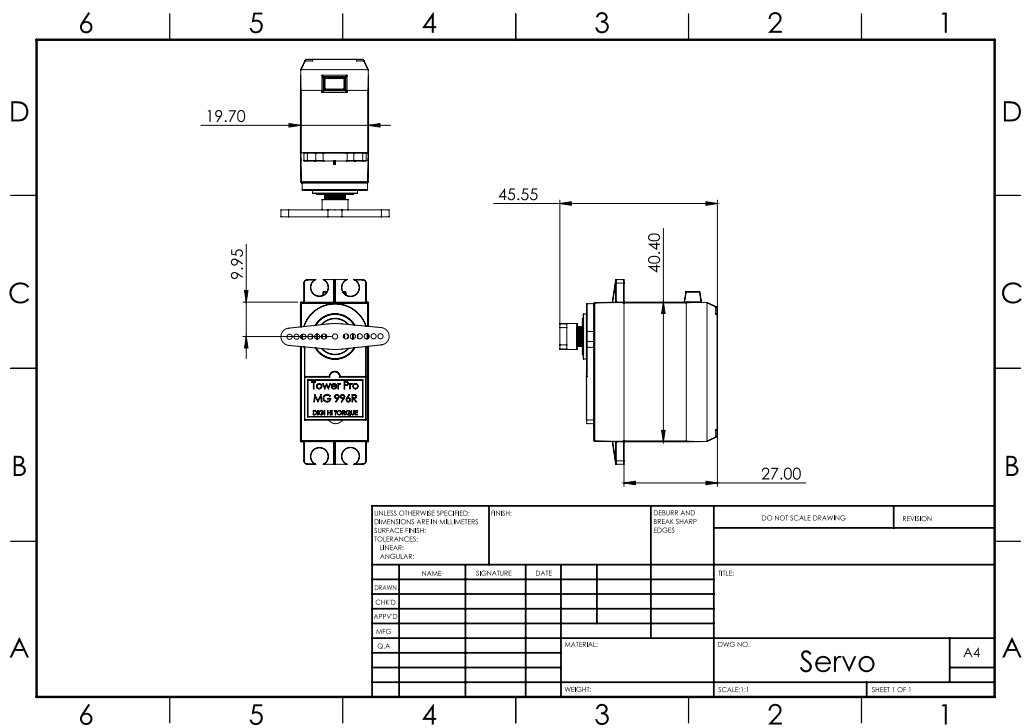
Fig. 13 Servo motor dimension
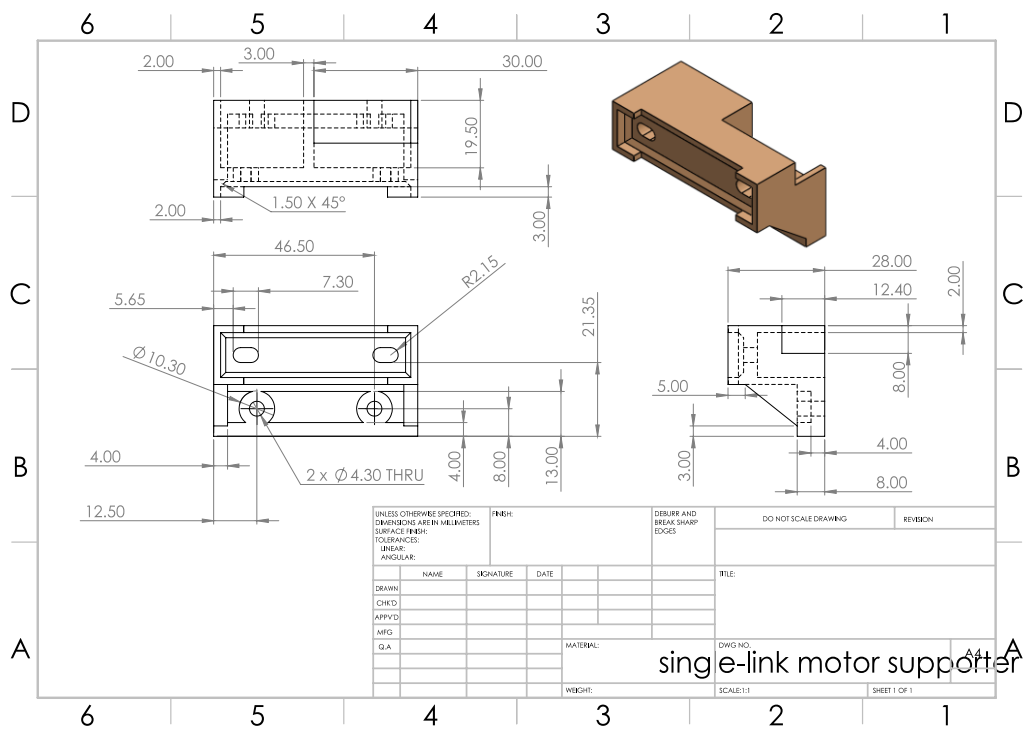
Fig. 14 Single-link motor supporter dimension
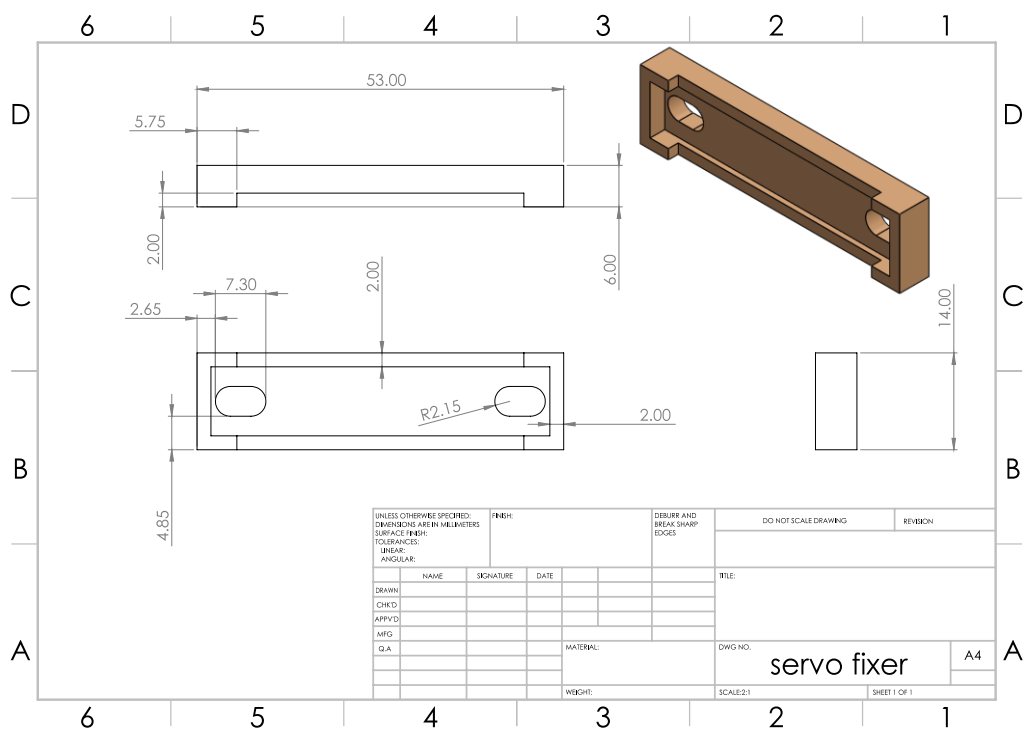
Fig. 15 Servo motor fixer dimension

108
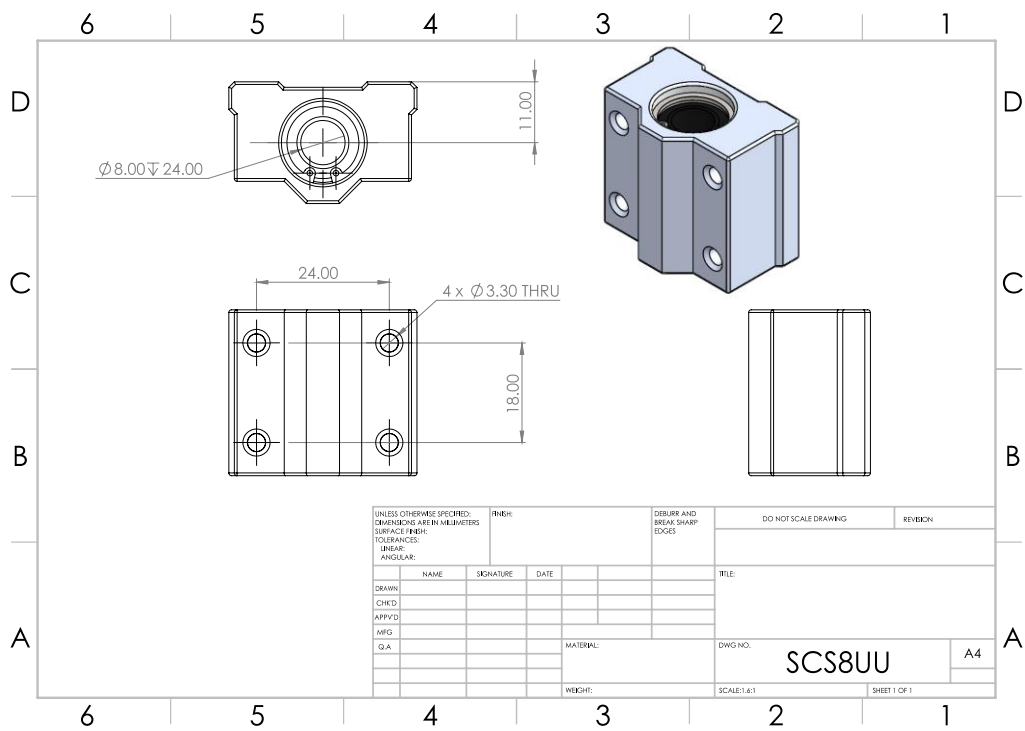
Fig. 16 Linear bearing SCS8UU dimension
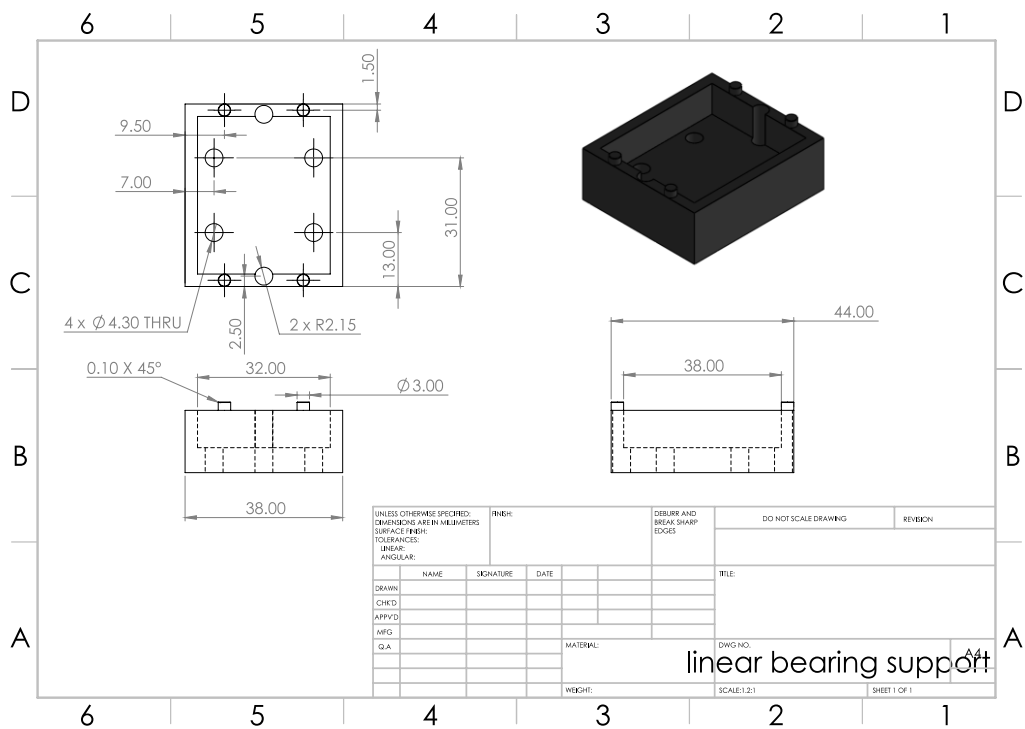
Fig. 17 Linear bearing supporter dimension
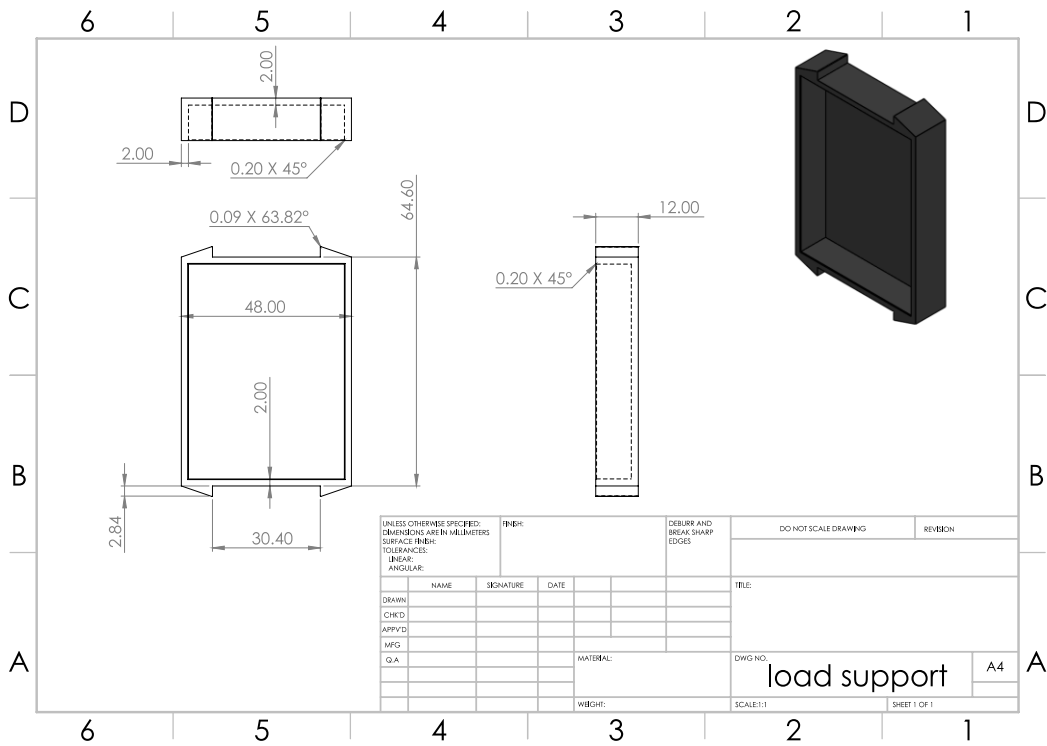
Fig. 18 Load supporter dimension

For the quarter-car configuration 2, all parts of main components are the same as those of configuration 1, excepting several parts such as: lower arm, upper arm and knuckle wheel hub. Those parts are shown below:
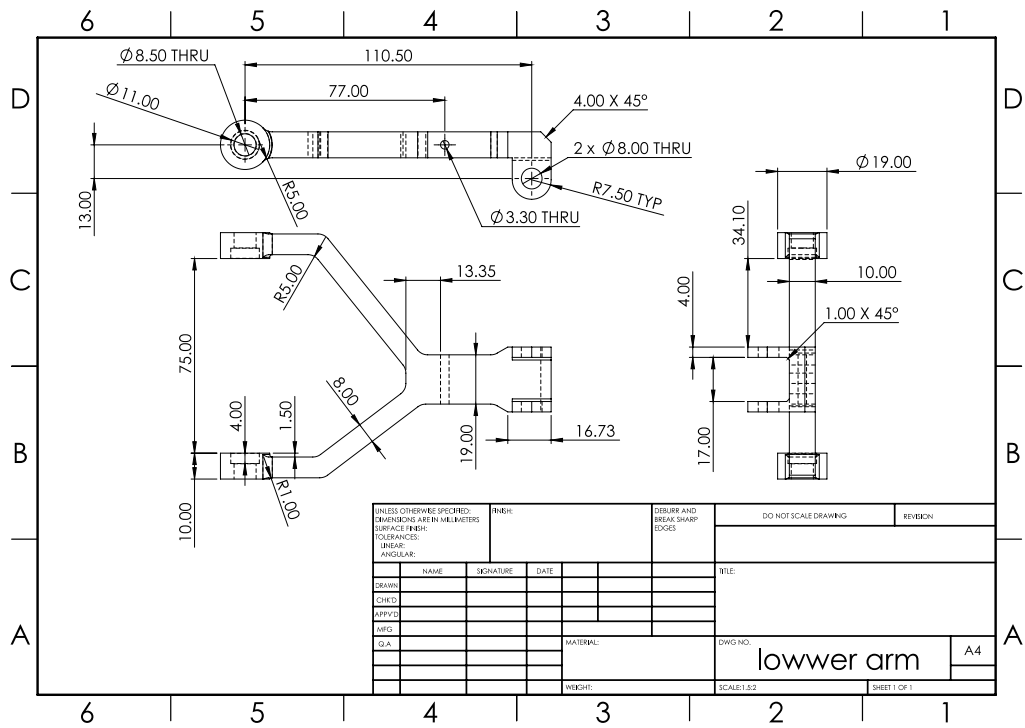
Fig. 19 Lower arm dimension for configuration 2
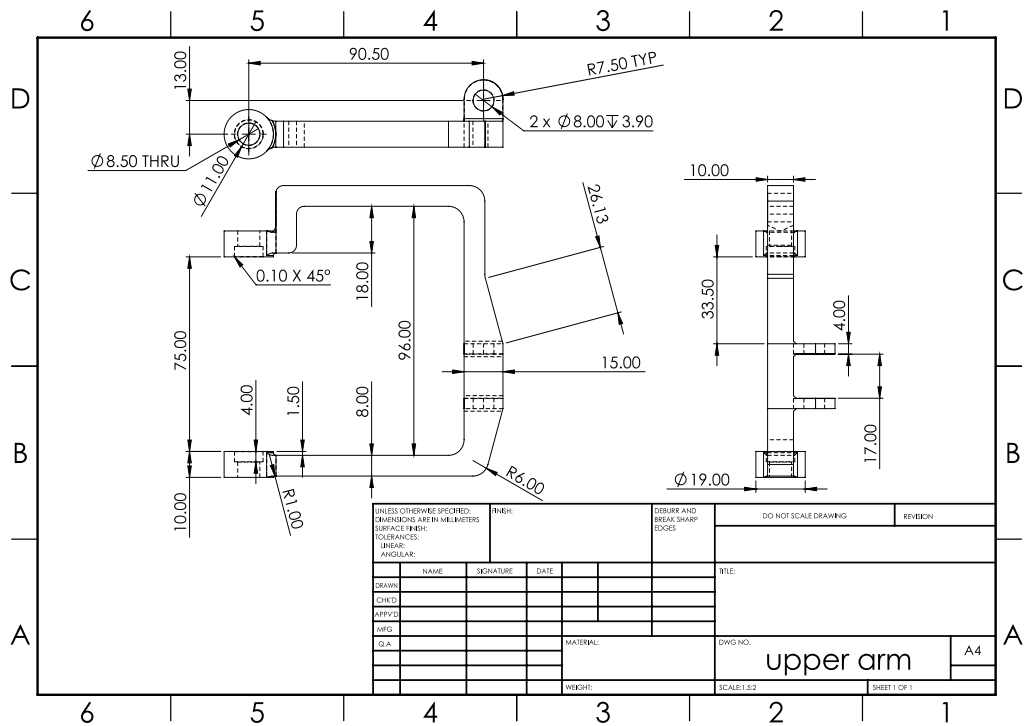
Fig. 20 Upper arm dimension for configuration 2

111
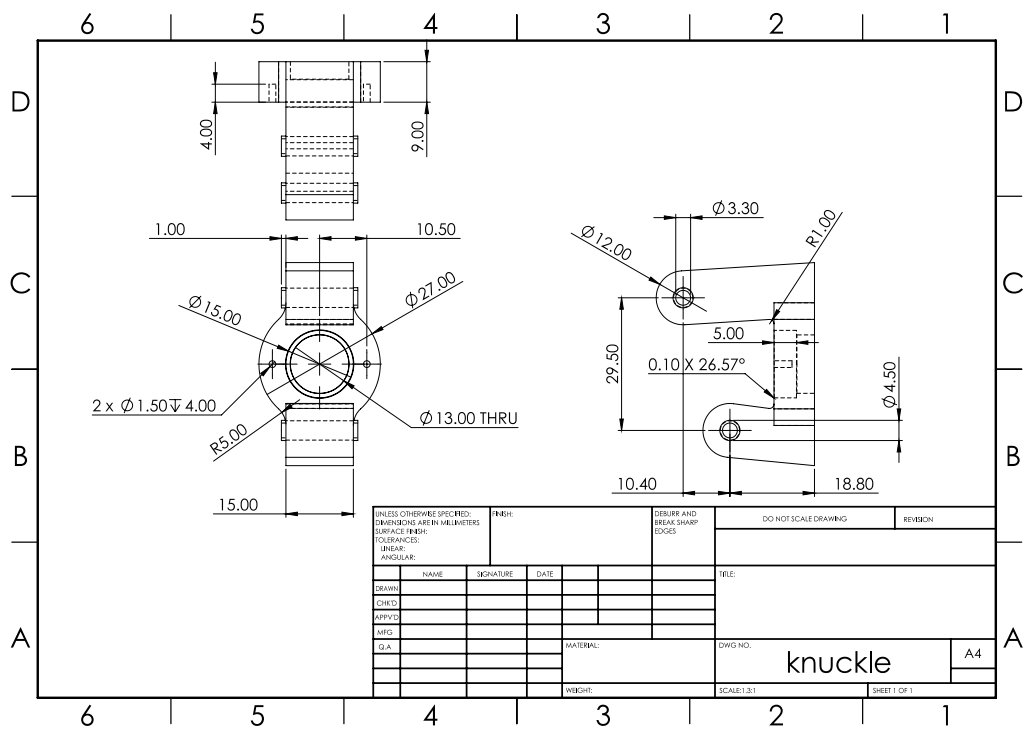
Fig. 21 Knuckle wheel hub for configuration 2

Appendix 2

Frame supporting and road exciting component dimensions
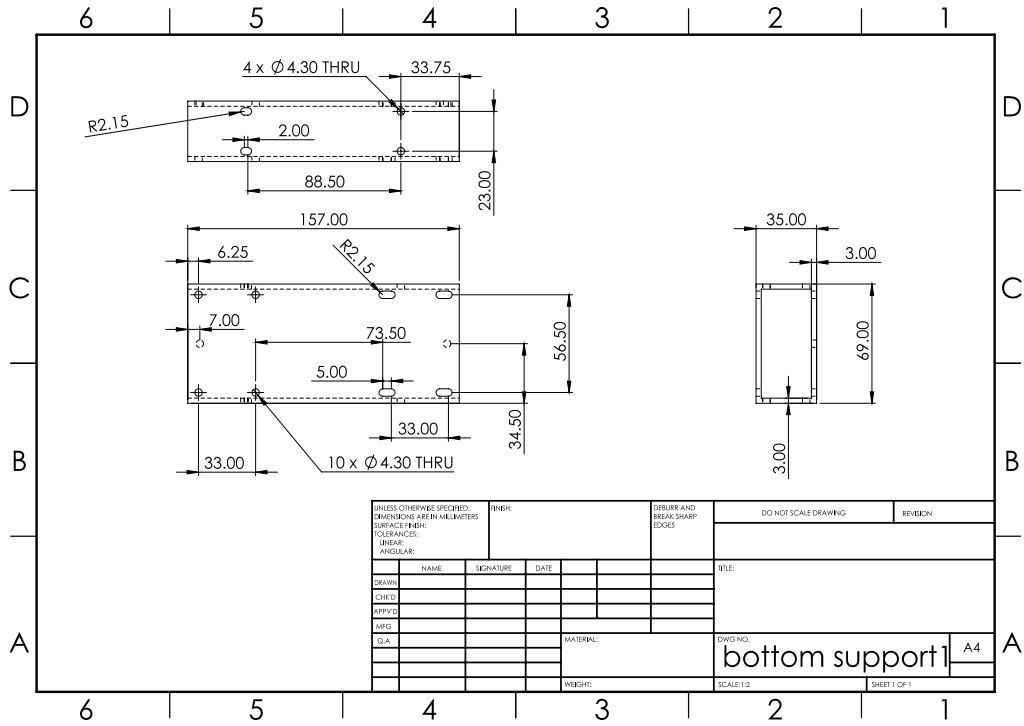
Fig. 22 Bottom support 1 dimension
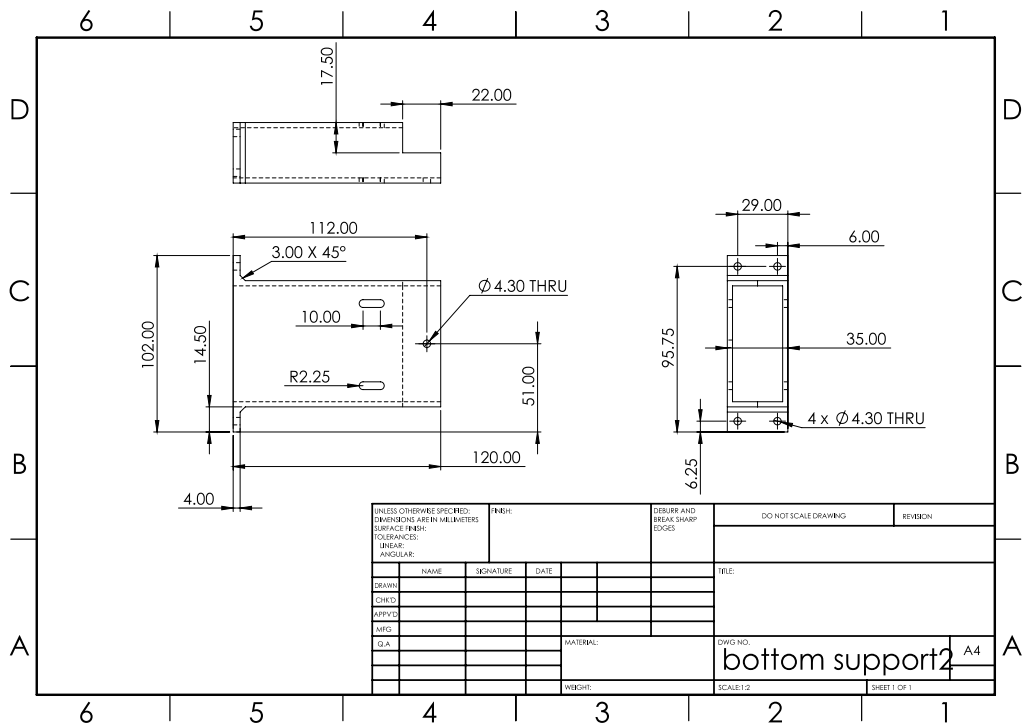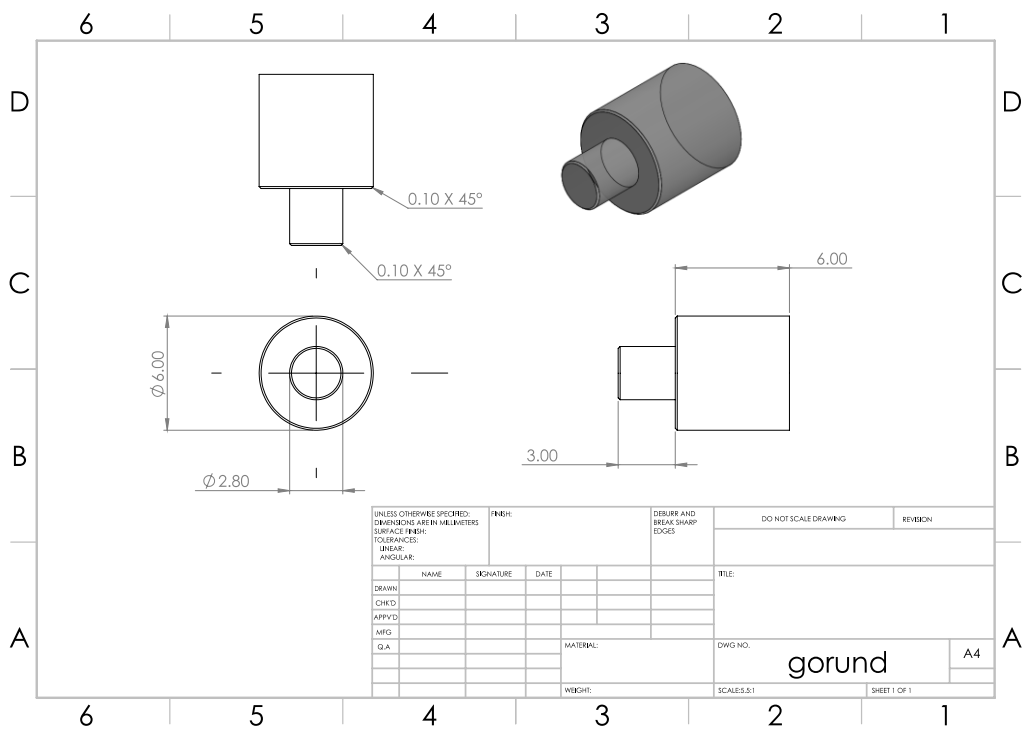
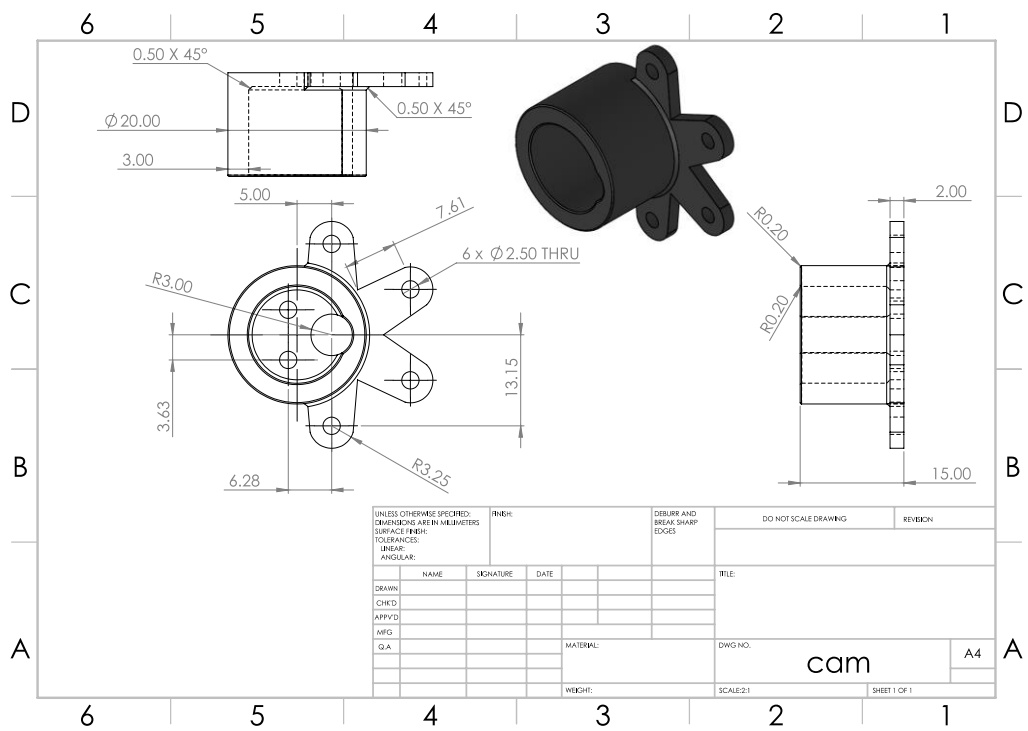Fig. 23 Bottom support 2 dimension

Fig. 24 Ground part dimension
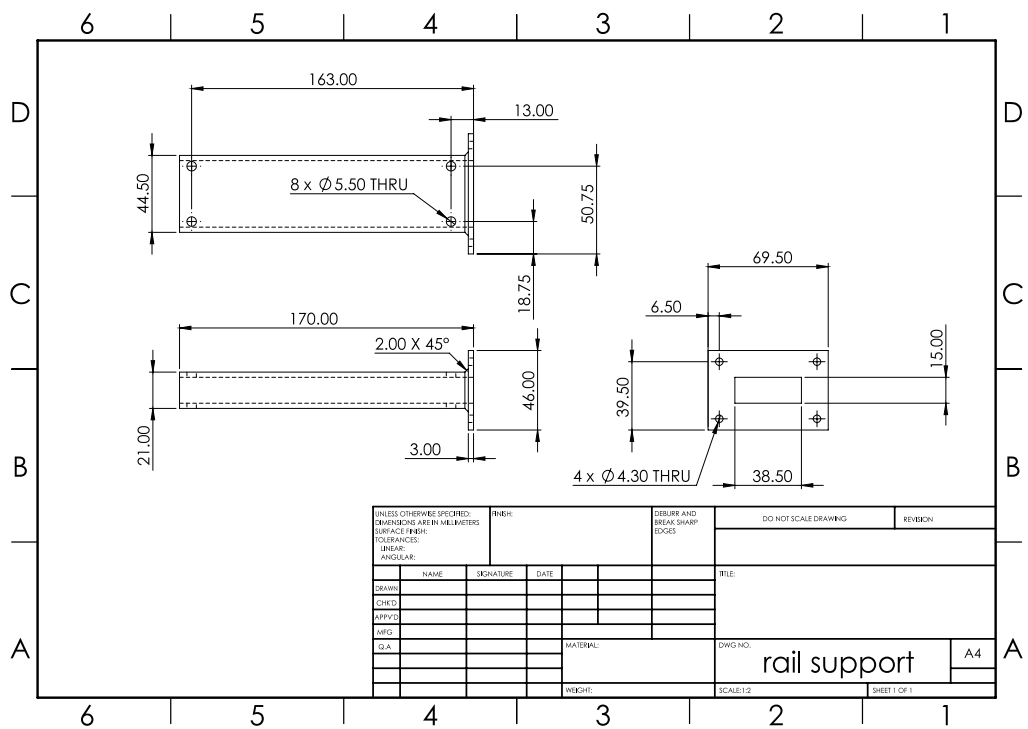
114

Fig. 25 Cam dimension

Fig. 26 Rail supporter dimension
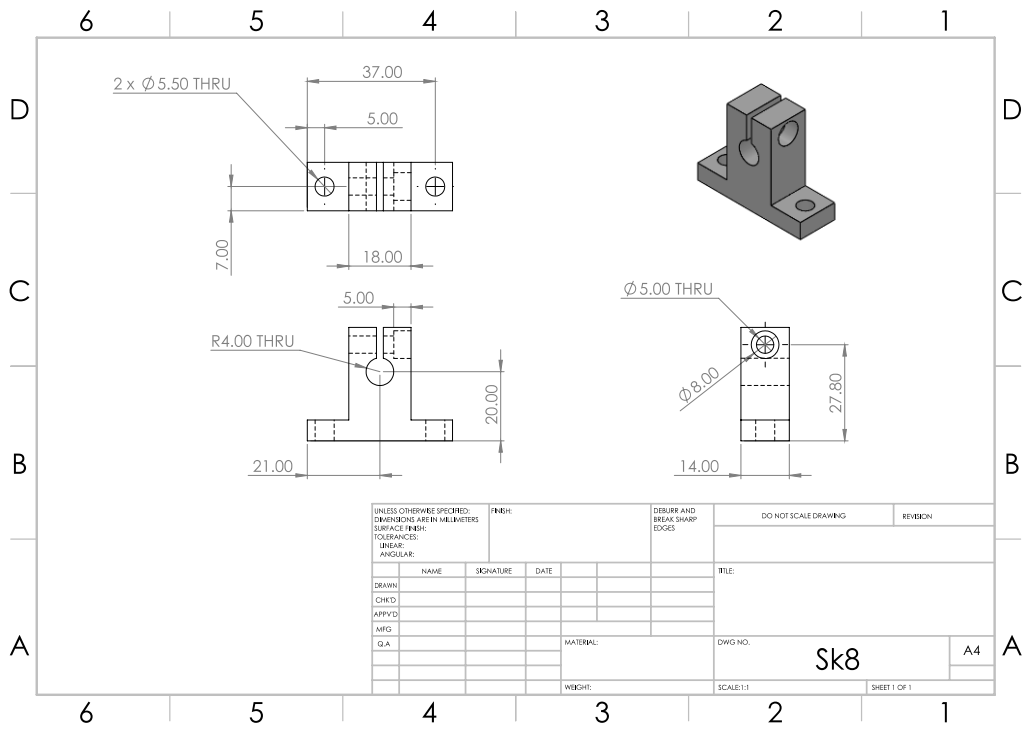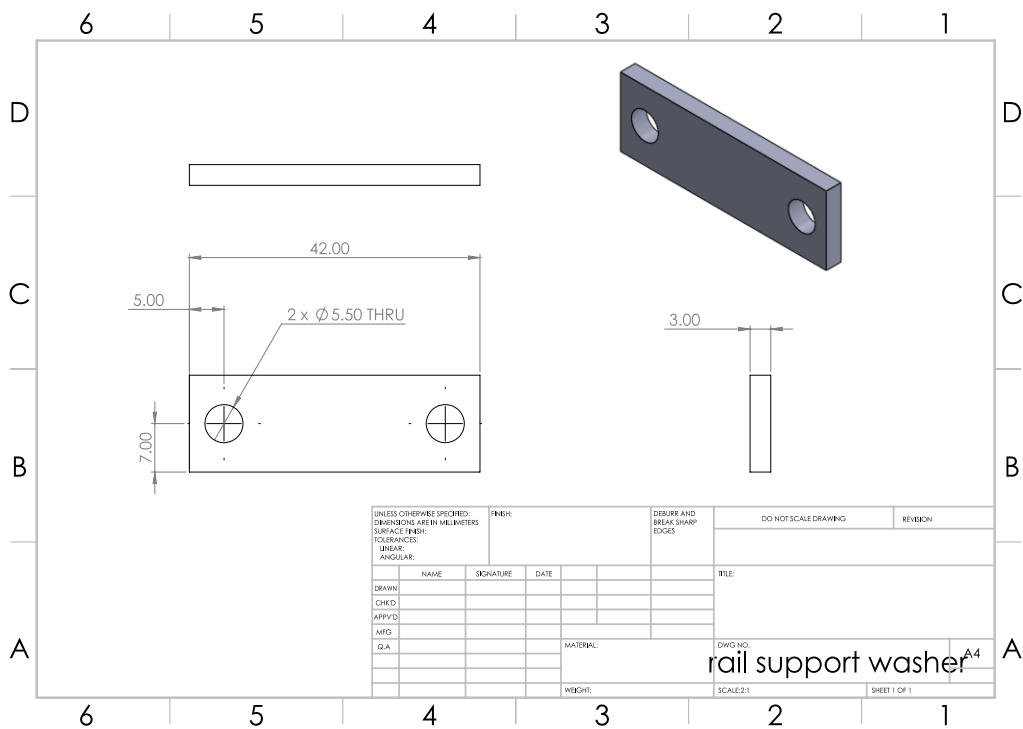
Fig. 27 Sk8 rod housing dimension

Fig. 28 Rail washer dimension

163.00

⌀8.00

UNLESS OTHERWISE SPECIFIED:
DIMENSIONS ARE IN MILLIMETERS
SURFACE FINISH:
TOLERANCES:
  LINEAR:
  ANGULAR:

FINISH:

DEBURR AND
BREAK SHARP
EDGES

DO NOT SCALE DRAWING | REVISION

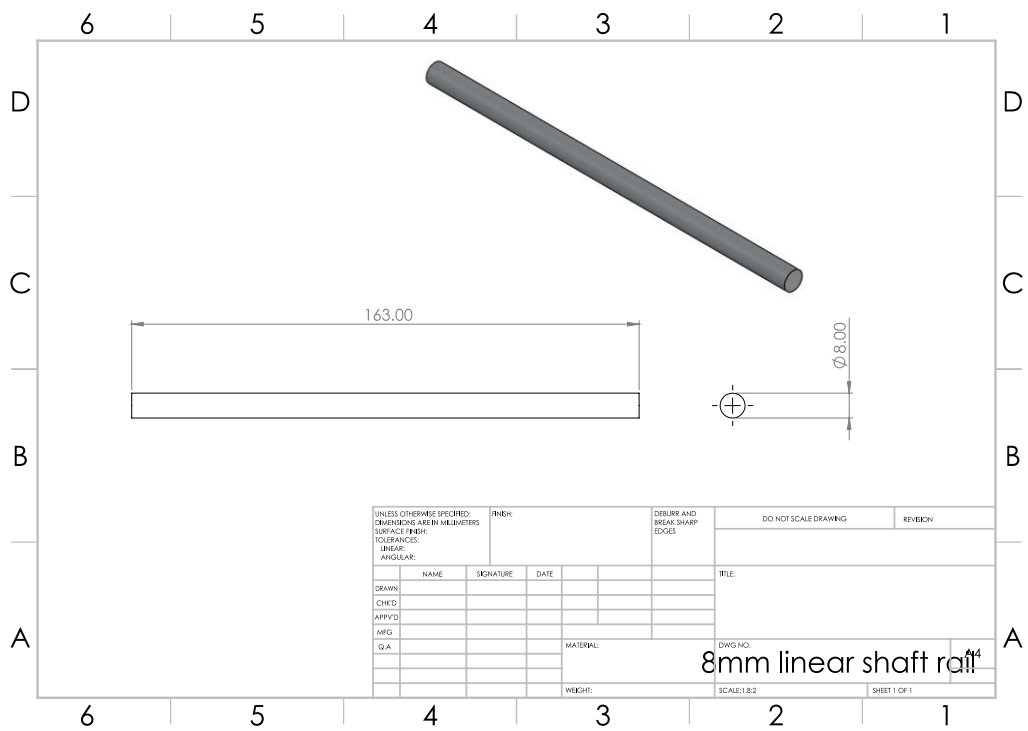|	NAME	SIGNATURE	DATE		TITLE:
DRAWN					
CHK'D					
APPV'D					
MFG					
Q.A			MATERIAL:		DWG NO.

8mm linear shaft rail

A4

WEIGHT: | SCALE:1.8:2 | SHEET 1 OF 1

Fig. 29 Rod guidance linear bearing dimension